

**TRANSPARENT AND CONDUCTIVE CARBON NANOTUBE MULTILAYER
THIN FILMS SUITABLE AS AN INDIUM TIN OXIDE REPLACEMENT**

A Dissertation

by

YONG TAE PARK

Submitted to the Office of Graduate Studies of
Texas A&M University
in partial fulfillment of the requirements for the degree of

DOCTOR OF PHILOSOPHY

May 2011

Major Subject: Mechanical Engineering

**TRANSPARENT AND CONDUCTIVE CARBON NANOTUBE MULTILAYER
THIN FILMS SUITABLE AS AN INDIUM TIN OXIDE REPLACEMENT**

A Dissertation

by

YONG TAE PARK

Submitted to the Office of Graduate Studies of
Texas A&M University
in partial fulfillment of the requirements for the degree of

DOCTOR OF PHILOSOPHY

Approved by:

Chair of Committee,
Committee Members,

Jaime C. Grunlan
Raymundo Arroyave
Michael J. McShane
Miladin Radovic

Head of Department,

Dennis L. O'Neal

May 2011

Major Subject: Mechanical Engineering

ABSTRACT

Transparent and Conductive Carbon Nanotube Multilayer Thin Films Suitable as an
Indium Tin Oxide Replacement. (May 2011)

Yong Tae Park, B.S., Korea Advanced Institute of Science and Technology;

M.S., Pohang University of Science and Technology

Chair of Advisory Committee: Dr. Jaime C. Grunlan

Transparent electrodes made from metal oxides suffer from poor flexibility and durability. Highly transparent and electrically conductive thin films based on carbon nanotubes (CNTs) were assembled as a potential indium tin oxide (ITO) replacement using layer-by-layer (LbL) assembly. The ultimate objective of this dissertation work is to produce CNT-based assemblies with sheet resistance below 100 Ω/sq and visible light transmission greater than 85%. The alternate deposition of positively charged poly(diallyldimethylammonium chloride) [PDDA] and CNTs stabilized with negatively charged deoxycholate (DOC) exhibit linear film growth and thin film properties can be precisely tuned. Ellipsometry, quartz crystal microbalance, and UV-vis were used to measure the growth of these films as a function of PDDA-CNT bilayers deposited, while TEM, SEM, and AFM were used to visualize the nanostructure of these films.

Following a literature review describing potential ITO substitutes and LbL technology, the influence of CNT type on optoelectronic performance of LbL assemblies is described. Three different types of nanotubes were investigated: (1) multiwalled

carbon nanotubes (MWNTs), (2) few-walled carbon nanotubes (FWNT), and (3) purified single-walled carbon nanotubes (SWNTs). SWNTs produced the most transparent ($>85\%$ visible light transmittance) and electrically conductive (148 S/cm , $1.62\text{ k}\Omega/\text{sq}$) 20-bilayer films with a 41.6 nm thickness, while MWNT-based films are much thicker and more opaque. A 20-bilayer PDDA/(MWNT+DOC) film is approximately 103 nm thick, with a conductivity of 36 S/cm and a transmittance of 30% .

In an effort to improve both transparency and electrical conductivity, heat and acid treatments were studied. Heating films to $300\text{ }^{\circ}\text{C}$ reduced sheet resistance to $701\text{ }\Omega/\text{sq}$ (618 S/cm conductivity, 38.4 nm thickness), with no change in transparency, owing to the removal of insulating component in the film. Despite improving conductivity, heating is not compatible with most plastic substrates, so acid doping was investigated as an alternate means to enhance properties. Exposing SWNT-based assemblies to HNO_3 vapor reduced sheet resistance of a 10 BL film to $227\text{ }\Omega/\text{sq}$. Replacing SWNTs with double walled carbon nanotubes (DWNTs) provided further reduction in sheet resistance due to the greater metallic of DWNT. A 5 BL DWNT film exhibited the lowest $104\text{ }\Omega/\text{sq}$ sheet resistance (4200 S/cm conductivity, 22.9 nm thickness) with 84% transmittance after nitric acid treatment. DWNT-based assemblies maintained their low sheet resistance after repeated bending and also showed electrochemical stability relative to ITO. This work demonstrates the excellent optoelectronic performance, mechanical flexibility, and electrochemical stability of CNT-based assemblies, which are potentially useful as flexible transparent electrodes for a variety of flexible electronics.

*To
My beloved wife, Shin Young,
My family,
and
My Lord Jesus*

ACKNOWLEDGEMENTS

I would like to thank my academic advisor, Dr. Jaime C. Grunlan, for his continual encouragement, support and guidance during my time at Texas A&M University, and my committee members, Dr. Raymundo Arroyave, Dr. Michael J. McShane, and Dr. Miladin Radovic, and Dr. Nicole Zacharia and Dr. Jean-Francois Feller, for their support throughout my Ph.D. research. Thanks also go to my colleagues, research associates, and Mechanical Engineering Department faculty and staff, especially former and current Polymer NanoComposites Laboratory members: Yeon Seok, Woo-Sik, Krishna, Yu-Chin, Morgan, You-Hao, Galina, Greg, and Amanda. I appreciate the assistance of Aaron Ham, my super undergraduate student, and Ms. Ann Ellis at the Microscopy & Imaging Center at Texas A&M University.

Finally, I would like to thank to my whole family for their continued support and love throughout my degree.

TABLE OF CONTENTS

	Page
ABSTRACT	iii
DEDICATION	v
ACKNOWLEDGEMENTS	vi
TABLE OF CONTENTS	vii
LIST OF TABLES	x
LIST OF FIGURES	xi
 CHAPTER	
I INTRODUCTION.....	1
1.1 Background	1
1.2 Objectives and Dissertation Outline.....	3
II LITERATURE REVIEW	7
2.1 Transparent and Conductive Thin Films.....	7
2.1.1 Metal Thin Films	7
2.1.2 Doped Transition Metal Oxide Thin Films	11
2.1.3 Fully Organic Conductive Thin Films	14
2.2 Layer-by-Layer Assembly.....	17
2.2.1 From Langmuir-Blodgett to Layer-by-Layer Assembly	17
2.2.2 Introduction to Layer-by-Layer Assembly.....	18
2.2.3 Particle-Based Layer-by-Layer Assemblies.....	24
III INFLUENCE OF CARBON NANOTUBE TYPE ON TRANSPARENCY AND ELECTRICAL CONDUCTIVITY OF THIN FILM ASSEMBLIES	26
3.1 Introduction	26
3.2 Experimental	27
3.2.1 Materials.....	27
3.2.2 Layer-by-Layer Assembly.....	28
3.2.3 Characterization of Film Growth	29
3.2.4 Microscopic Imaging.....	30

CHAPTER	Page
3.2.5 Electrical Property Characterization	30
3.3 Results and Discussion.....	31
3.3.1 Growth of Carbon Nanotube Assemblies.....	31
3.3.2 Structural Characterization.....	36
3.3.3 Optoelectronic Behavior.....	41
3.4 Conclusions	47
IV HEATING CARBON NANOTUBE ASSEMBLIES FOR REDUCED SHEET RESISTANCE	49
4.1 Introduction	49
4.2 Experimental	50
4.2.1 Materials.....	50
4.2.2 Layer-by-Layer Assembly and Heat Treatment.....	50
4.2.3 Thin Film Characterization and Microscopic Imaging	50
4.3 Results and Discussion.....	51
4.3.1 Influence of Deoxycholate on Carbon Nanotube Assemblies	51
4.3.2 Growth of SWNT Assemblies.....	53
4.3.3 Electrical Properties after Heat Treatment	58
4.4 Conclusions	62
V ACID TREATMENT OF CARBON NANOTUBE ASSEMBLIES FOR REDUCED SHEET RESISTANCE	63
5.1 Introduction	63
5.2 Experimental.....	64
5.2.1 Materials.....	64
5.2.2 Layer-by-Layer Assembly and Acid Treatment.....	65
5.2.3 Thin Film Characterization	66
5.3 Results and Discussion.....	66
5.3.1 Growth and Microstructure of Carbon Nanotube Assemblies before and after Acid Treatment	66
5.3.2 Optoelectronic Performance of Carbon Nanotube Assemblies.....	70
5.3.3 Influence of Acid Treatment on Sheet Resistance	72
5.3.4 Mechanical and Electrochemical Stability of Carbon Nanotube Assemblies	87
5.4 Conclusions	90
VI CONCLUSION AND FUTURE WORK.....	92
6.1 Influence of Carbon Nanotube Type on Optoelectronic Performance	92
6.2 Heat Treatment for Reducing Sheet Resistance	93

CHAPTER	Page
6.3 Acid Treatment for Reducing Sheet Resistance	93
6.4 Future Research Plan	94
6.4.1 Graphene-Based Layer-by-Layer Transparent Electrodes	94
6.4.2 Electronic Devices with Layer-by-Layer Assemblies	97
REFERENCES AND NOTES.....	99
APPENDIX A	115
VITA	142

LIST OF TABLES

TABLE	Page
1.1 Summary of Various Types of Transparent Electrodes and Their Potential Applications (reproduced from [65])	8
3.1 Growth, Density, and Composition of PDDA/(CNT+DOC) Assemblies	32
3.2 Characteristic Temperature of Each CNT and CNT Composition in PDDA/(CNT+DOC) Assemblies	35
5.1 Carbon and Oxygen Contents in DWNT and EA-SWNT Films before and after Acid Treatment	78

LIST OF FIGURES

FIGURE	Page
1.1 Schematic of the LbL process for making conductive thin films that involves dipping a substrate in cationic PDDA and anionically-stabilized CNT mixtures, followed by rinsing with water and drying with filtered air. These steps generate one bilayer (BL) and are repeated to grow a film with a given number of bilayers.	3
1.2 Overview of the carbon nanotube-based electrode research described in this dissertation.	4
2.1 (a) Survey of growth stages, structures, and thickness scales for Au thin films deposited on glass by conventional evaporation and ion-assisted evaporation (reproduced from [66]). (b) Thickness-dependent electrical resistivity of Au films on two different substrates, in as-deposited state and after annealing at 350 °C (arrow: the resistivity of bulk Au, reproduced from [68]).	9
2.2 (a) Transmittance and reflectance of Ag films with different thicknesses on glass substrates (reproduced from [69]). (b) Transmittance of Au films with the sub-wavelength holes, which lead to extraordinary transmittance in a band centered at 615 nm (reproduced from [71]).	10
2.3 (a) Transmittance and reflectance of TiO ₂ /Ag/TiO ₂ coatings (reproduced from [73]). (b) Sheet resistance and maximum transmittance as a function of Ag thickness in ZnO(20 nm)/Ag/ZnO(20 nm) coatings (reproduced from [74]).	11
2.4 Optical transmission and resistivity as a function of (a) ITO film thickness and (b) sputtering power (at 100 nm film thickness) (reproduced from [79]).	12
2.5 Effect of the number of deflection cycles on (a) the film resistivity and (b) the average visible light transmittance for samples of varying thickness (reproduced from [3]).	13
2.6 (a) Sheet resistance and transparency of PEDOT–PSS relative to ITO. (b) Antistatic coating for cathode ray tubes to prevent dust attraction. (c) Schematic structure of an inorganic electroluminescent device with the traditional ITO layer replaced by a PEDOT–PSS layer (reproduced from [31])....	14

FIGURE	Page
2.7 Illustration of several methods for carbon nanotube film fabrication: (a) vacuum filtration, (b) air-spraying, (c) transfer printing, and (d) rod coating (reproduced from [91], [92], [37], and [42], respectively).	16
2.8 (a) AFM image of a nanotube film with $R_S = 200 \text{ } \Omega/\text{sq}$ on a glass slide and film thickness of 25 nm. (b) Optoelectronic behavior (transmittance at 550 nm vs. sheet resistance) of nanotube films with different thickness on PET substrates. The bold line shows the performance of commercially available ITO films on PET substrates. The inset shows transmittance of a nanotube film with $R_S = 120 \text{ } \Omega/\text{sq}$. (reproduced from [36]).	16
2.9 Schematic of the electrostatic layer-by-layer self-assembly process (reproduced from [48]).	19
2.10 (a) Cross-sectional confocal microscopy image of a graded PDDA/CdTe film made of 10 BLs of four different size CdTe QDs (green, yellow, orange, and red; total 40 BLs). (b) TEM cross-section of a graded film made from 5 BLs of green, yellow, and red QDs (reproduced from [116]). (c) Illustration of the LbL procedure used to prepare CdTe QD-microsphere bioconjugates (reproduced from [117]).	21
2.11 LbL coatings on the surfaces of (a) a patterned PDMS stamp, (b) fibers, and (c) polycarbonate porous membrane templates (reproduced from [118], [112], and [121], respectively). (d) The nanotubes prepared in the membranes with 400 nm diameter pores via the LbL process of (c).	21
2.12 (a) Thickness as a function of the number of layers deposited for a PSS/PDDA multilayer on a silicon wafer (reproduced from [122]). (b) Thickness as a function of bilayers deposited for films made with clay and polyethylenimine. (reproduced from [52]). (c) Proposed film growth mechanism for BPEI/MMT and BPEI/LAP with different deposition times. (reproduced from [125]). (d) X-ray reflectivity spectra of three LbL films dried with different methods. Film 1 was dried by spinning after each dipping step. Film 2 was prepared like 1 , but was immersed in water and dried in air after the film build-up was completed. Film 3 was dried in air after each dipping step (reproduced from [128]).	23
2.13 (a) LbL assembly with TiO_2 and SiO_2 nanoparticles used (reproduced from [135]). (b) AFM images of all-silica nanoparticle multilayers at pH 2 after 1, 2, and 3 deposition cycles (reproduced from [136]).	24

FIGURE	Page
2.14 SEM morphology of (a) [(PVA/PSS) ₃ (PVA/SWNT-PSS) ₁₅], (b) [(PVA/PSS) ₃ (PVA/TWNT-PSS) ₂₅], and (c) [(PVA/PSS) ₃ (PVA/MWNT-PSS) ₁₇] (reproduced from [61]). (d) MWNT thin film assembled with positively and negatively charged MWNTs (reproduced from [63]). (e) Electrical conductivity of [PVA/(SWNT+PSS)] _n as a function of the number of bilayers (reproduced from [60]).	25
3.1 (a) Film thickness of three types of [PDDA/(CNT+DOC)] ₂₀ thin films as a function of the number of bilayers deposited, as determined by ellipsometry. (b) Film thickness of a [PDDA/(SWNT+DOC)] ₂₀ thin film as a function of the number of bilayers deposited. The inset is the film thickness from 10 to 15 BLs, where a half bilayer corresponds to PDDA deposition.	31
3.2 (a) Mass growth of three types of [PDDA/(CNT+DOC)] ₂₀ thin films as a function of the number of bilayers deposited, as measured by QCM. (b) Mass growth of a [PDDA/(SWNT+DOC)] ₂₀ thin film as a function of the number of bilayers deposited. The inset is the mass change from 10 to 15 BLs, where a half bilayer corresponds to PDDA deposition.	33
3.3 Thermogravimetry of each component of CNT-based LbL films and three types of LbL films ((a) PDDA, (b) DOC, (c) MWNT, (d) [PDDA/(MWNT+DOC)], (e) FWNT, (f) [PDDA/(FWNT+DOC)], (g) SWNT, and (h) [PDDA/(SWNT+DOC)]) under dried air and nitrogen gas, respectively. The difference between the air and nitrogen curves is also plotted to reveal the characteristic peak for a given material.	34
3.4 (a) Optical images of glass vials containing a 0.25 wt% PDDA aqueous solution and 0.05 wt% MWNT, FWNT, SWNT aqueous solutions stabilized by 2.0 wt% DOC. [PDDA/(CNT+DOC)] ₂₀ coatings on both sides of (b) quartz and (c) PS substrates with (i) MWNT, (ii) FWNT, and (iii) SWNT.	36
3.5 TEM cross-sections of a [PDDA/(MWNT+DOC)] ₂₀ thin film at (a) low and (b) high magnifications. Cross-sections of a [PDDA/(SWNT+DOC)] ₂₀ thin film are also shown at the same (c) low and (d) high magnifications.	37
3.6 TEM surface images of (a) [PDDA/(MWNT+DOC)] ₂ , (b) [PDDA/(FWNT+DOC)] ₂ , and (c) [PDDA/(SWNT+DOC)] ₂ assemblies on Formvar grids.	39
3.7 SEM surface images of (a) [PDDA/(MWNT+DOC)] ₂₀ , (b) [PDDA/(FWNT+DOC)] ₂₀ , and (c) [PDDA/(SWNT+DOC)] ₂₀ assemblies on PS film.	40

FIGURE	Page
3.8 (a) Absorbance of PDDA/(CNT+DOC) assemblies on quartz slides from 200 to 850 nm. The inset is absorbance spectra of a PDDA/(SWNT+DOC) measured in 2 BL step up to 20 BLs. (b) Absorbance of the same thin films at 550 nm, as a function of the number of BLs deposited, is also shown.	42
3.9 (a) Sheet resistance of [PDDA/(CNT+DOC)] _n thin films as a function of the number of bilayers deposited on PS film. (b) Electrical conductivity of the same systems as a function of the number of bilayers deposited, using the data in (a) multiplied by ellipsometric film thickness (Figure 3.1).	43
3.10 Comparison of the optoelectronic performance of [PDDA/(CNT+DOC)] _n thin films with other transparent and conductive SWNT thin films.	46
4.1 (a) Photograph of 0.05 wt% SWNT only solution and (0.05 wt% SWNT+1 wt% DOC) solution after 1 hour from sonication. (b) Photograph of (0.05 wt% SWNT+1 wt% DOC) and (0.05 wt% DWNT+1 wt% DOC) solutions after 2 months from sonication.	51
4.2 Comparison of the ellipsometric 20BL thickness, UV-vis absorbance at 550 nm, and electrical conductivity of four different films. These [PDDA/(SWNT+DOC)] ₂₀ films were fabricated with four different concentrations of DOC.	53
4.3 (a) Photograph of [PDDA/(SWNT+DOC)] _n ($n = 4-20$) assemblies on both sides of PS film. (b) Optical image of a [PDDA/(SWNT+DOC)] ₂₀ coating on both sides of the 7.5×7.5 cm PS film. (c) TEM cross-section of a [PDDA/(SWNT + DOC)] ₂₀ thin film.	54
4.4 (a) Absorbance and (b) transmittance spectra of [PDDA/(SWNT+DOC)] _n thin films, measured in 2 BL step up to 20 BLs. The dotted line is of [PDDA/(SWNT+ DOC)] ₂₀ after 300 °C heating for 5 min.	54
4.5 SEM surface images of [PDDA/(SWNT+DOC)] ₂₀ (on a silicon wafer) (a) before heat treatment and (b) after heating at 300 °C for 10 min.	55
4.6 (a) Growth of PDDA/(SWNT+DOC) thin films as a function of the number of bilayers deposited. Film thickness was obtained by ellipsometry, mass by QCM, and absorbance (at 550 nm) by UV-vis (inset), respectively. (b) Thickness and mass change from 10 to 15 BLs, where a half bilayer corresponds to PDDA deposition.	56

FIGURE	Page
4.7 (a) Optoelectronic performance and (b) electrical conductivity of [PDDA/(SWNT+DOC)] _n thin films as a function of the number of bilayers deposited to 20 BL are also shown.	57
4.8 Thermogravimetry of the components of the PDDA/(SWNT+DOC) system and a fully assembled film under a nitrogen atmosphere.	59
4.9 (a) Sheet resistance and (b) electrical conductivity of [PDDA/(SWNT+DOC)] ₂₀ thin films after 300, 350, and 400 °C heating, for 1 to 20 min.	60
4.10 Normalized thickness and sheet resistance after heat treatment. White and grey colors mean before and after heating, respectively.	61
5.1 (a) Schematic of acid treatment apparatus and (b) picture of actual apparatus without cover.	65
5.2 Thickness of PDDA/(DWNT+DOC) thin films as a function of the number of bilayers deposited. The solid lines are linear curve fits. Transmittance was calculated from absorbance data. White points with black outlines are values after 20 min of exposure to nitric acid vapor.	67
5.3 (a) Photograph of a 100 Ω/sq single side ITO-coated PET and a 5 BL DWNT assembly (103 Ω/sq) on both sides of PET. (b) Transmittance spectra of a ITO-coated PET and [PDDA/(DWNT+DOC)] _n (n = 1–5) on PET. Absorbance of the LbL thin films, coated on both sides of PET was divided by two to produce the data shown in (b). The dotted lines are transmittance of [PDDA/(DWNT+DOC)] ₅ after sulfuric, nitric, and hydrochloric acid treatment.	68
5.4 SEM surface images of [PDDA/(DWNT+DOC)] ₆ on PET (a) before and (b) after 20 min exposure to nitric acid vapor. TEM cross-sections of [PDDA/(DWNT+DOC)] ₁₀ (a) before and (b) after 20 min treatment with nitric acid.	70
5.5 (a) Optoelectronic performance and (b) electrical conductivity as a function of thickness for the [PDDA/(EA-SWNT+DOC)] _n and [PDDA/(DWNT+DOC)] _n systems.	71
5.6 (a) Sheet resistance and (b) electrical conductivity of [PDDA/(HiPCO-SWNT+DOC)] ₂₀ thin films after 300, 350, and 400 °C heat treatment for 5 min and nitric acid treatment. The values after heat treatment are from Figure 4.9 in Chapter IV.	74

FIGURE

Page

5.7	Normalized thickness and sheet resistance of [PDDA/(HiPCO-SWNT+DOC)] ₂₀ thin films after post-treatments, such as only nitric acid treatment (a), heat treatment (b–m), heat and acid treatments (c, g, k, m), and annealing after heat and acid treatments (c", k"). Rectangles and circles mean thickness and sheet resistance, respectively. White, grey, black, and gradient colors are samples before heat treatment, after heat treatment, after acid treatment, and after annealing, respectively.	75
5.8	Sheet resistance of [PDDA/(DWNT+DOC)] ₅ after acid treatment for 2 to 20 min with nitric acid, hydrochloric acid, and sulfuric acid, respectively. (a) is the sheet resistance of an as-assembled 5 BL DWNT thin film.	76
5.9	EDX spectrum of [PDDA/(DWNT+DOC)] ₅ before acid treatment. Platinum was from ~ 10 nm thin coating for SEM images. The inset contains spectra of the 5BL DWNT films after 20 min nitric acid and sulfuric acid treatments, respectively.	77
5.10	SEM surface images of [PDDA/(DWNT+DOC)] ₅ on PET (a) before and after (b) 20 min HNO ₃ , (c) 20 min HCl, and (d) 20 min H ₂ SO ₄ treatments, respectively.	79
5.11	Sheet resistance of [PDDA/(EA-SWNT+DOC)] ₅ , [PDDA/(DWNT+DOC)] ₅ , and [PDDA/(DWNT+DOC)] ₁₀ as a function of nitric acid treatment time.	80
5.12	(a) FT-IR spectra of [PDDA/(DWNT+DOC)] ₂₅ before and after nitric acid treatment, from 2 to 20 min. These spectra are magnified and overlaid with arbitrary offset for clarity. (b) EDX spectra of the [PDDA/(DWNT+DOC)] ₅ before and after nitric acid treatment, from 2 to 20 min exposure time.	82
5.13	SEM surface images of [PDDA/(DWNT+DOC)] ₅ on PET (a) before and (b) after 2 min, (c) 5 min, and (d) 20 min HNO ₃ exposure, respectively.	83
5.14	EDX spectra of [PDDA/(EA-SWNT+DOC)] ₁₀ before and after 20 min nitric acid treatment. These spectra are magnified to emphasize oxygen content.	84
5.15	SEM surface images of [PDDA/(EA-SWNT+DOC)] ₁₀ on PET (a) before and (b) after 20 min exposure to nitric acid vapor.	85
5.16	Optoelectronic performance of several CNT LbL systems before and after acid treatment. Points with the black outline are values of as-assembled LbL films and those with no outline are acid-treated LbL films.	86

FIGURE	Page
5.17 Sheet resistance as a function of bending cycles (to 1 cm radius of curvature) for 5 BL DWNT and 100 Ω/sq ITO-coated PET films. R_{S0} indicates the value prior to any bending.	87
5.18 Cyclic voltammograms of a [PDDA/(DWNT+DOC)] ₅ thin film on PET and a commercial 100 Ω/sq ITO-coated PET. Measurements were made in 0.1 M Na ₂ SO ₄ , at room temperature, with a scan rate of 100 mV/s.	88
5.19 (a) Cyclic voltammograms of [PDDA/(DWNT+DOC)] _n assemblies deposited on PET. (b) Integrated charge density of each film, as a function of film thickness, was calculated from cyclic voltammograms and electrode area.	89
6.1 (a) Graphene oxide structure. (b) Deposition of graphene oxide sheet by dip coating and an SEM image of deposited graphene oxide pieces (reproduced from [172]). (c) Photo reduction lithography approach for fabrication of patterns on (PDDA/Graphene Oxide/PDDA/TiO) ₂₀ LbL thin films (reproduced from [180]). (d) Schematic illustration of a reduced graphene oxide field-effect transistor for biosensing applications (reproduced from [183]).	95
6.2 (a) An image of a series of SWNT-based assemblies deposited on vapor sensing electrodes (reproduced from [186]). (b) Metal oxide-based transparent transistors. An ITO lower layer as a gate, an aluminum–titanium oxide (ATO) upper layer as the gate dielectric, and a ZnO channel layer on a glass substrate (reproduced from [185]).	98
A.1 Schematic of the LbL process. The three recipes studied here are each represented by their own schematic: (a) PVP-S/WO ₄ ²⁻ , (b) (PVP-S+ITO)/WO ₄ ²⁻ , and (c) PVP-S/WO ₄ ²⁻ /(PDDA+ITO)/WO ₄ ²⁻ quad-layer (QL).	117
A.2 Film thickness as a function of the number of PVP-S/WO ₄ ²⁻ BLs deposited, as determined by ellipsometry. The thickness increase from 15 to 20 BLs is shown in the inset. Half bilayers correspond to PVP-S deposition.	122
A.3 Mass growth as a function of the number of PVP-S/WO ₄ ²⁻ BLs deposited, as measured with QCM. The inset is the mass change from 30 to 35 BLs. Half bilayers correspond to PVP-S deposition.	123
A.4 Spectral absorbance (i) and transmittance (ii) of a 50 BL PVP-S/WO ₄ ²⁻ film produced on a fused quartz slide. The inset is the absorbance of a 145 nm PVP-S film that was spun coat on a quartz slide.	124

FIGURE	Page
A.5 Absorbance spectra of a quartz slide (i) and n BLs of PVP-S/ WO_4^{2-} , with $n = 5$ (ii) to 50 (iii), and every 5 BL step in between. The inset is absorbance at 250 nm as a function of the number of BLs deposited.	125
A.6 Film thickness and mass growth as a function of the number of (a) (PVP-S+ITO)/ WO_4^{2-} BLs and (b) PVP-S/ WO_4^{2-} /(PDDA+ITO)/ WO_4^{2-} QLs, as determined by ellipsometry and QCM. Half bilayers correspond to PVP-S deposition.	126
A.7 TEM cross-sections of (a) a 60 BL PVP-S/ WO_4^{2-} film, (b) a 60 BL (PVP-S+ITO)/ WO_4^{2-} film, and (c) a 30 QL PVP-S/ WO_4^{2-} /PDDA+ITO/ WO_4^{2-} film.	127
A.8 AFM height images of (a) 50 BL PVP-S/ WO_4^{2-} , (b) 50 BL (PVP-S+ITO)/ WO_4^{2-} , and (c) 25 QL PVP-S/ WO_4^{2-} /(PDDA+ITO)/ WO_4^{2-} film surfaces on silicon wafers.	128
A.9 TEM surface images of (a) 5 BL PVP-S/ WO_4^{2-} , (b) 5 BL (PVP-S+ITO)/ WO_4^{2-} , and (c) 3 QL PVP-S/ WO_4^{2-} /(PDDA+ITO)/ WO_4^{2-} films on formvar grids.	128
A.10 Cyclic voltammetry of a 60 BL PVP-S/ WO_4^{2-} film on an ITO-coated glass slide at 25, 50, 100, and 200 mV/s scan rates in an aqueous 0.1M LiCl electrolyte (pH = 2.5) with an AgCl/Ag reference electrode. Linear dependence of peak current density of a 60 BL PVP-S/ WO_4^{2-} film as a function of the square root of the scan rate is shown in the inset.	130
A.11 Cyclic voltammetry of (a) a 60 BL (PVP-S+ITO)/ WO_4^{2-} film at 25, 50, 100, and 200 mV/s scan rates and (b) a 30 QL PVP-S/ WO_4^{2-} /(PDDA+ITO)/ WO_4^{2-} film at 50, 100, and 200 mV/s scan rates on ITO-coated glass slides with a AgCl/Ag reference electrode, in an aqueous 0.1M LiCl electrolyte (pH = 2.5). The insets highlight the linear dependence of peak current density of each film on the square root of the scan rate.	131
A.12 (a) Absorption spectra of a 60 BL PVP-S/ WO_4^{2-} film at +2.0, 0, and -1.0 V applied potentials. (b) Absorbance at 750 nm as a function of time during repeated potential steps. The inset is the transmittance plot of this same film during the same time interval.	132
A.13 (a) Absorption spectra for a 60 BL (PVP-S+ITO)/ WO_4^{2-} film at applied potentials from +2.0 to -1.0 V in 0.5 V steps. (b) Absorbance changes at 750 nm during repeated potential steps.	134

FIGURE

Page

- A.14 (a) Absorption spectra for a 30 QL PVP-S/ WO_4^{2-} /(PDDA+ITO)/ WO_4^{2-} film at applied potentials from +2.0 to −3.0 V in 0.5 V steps. (b) Absorbance changes at 750 nm during repeated potential steps. 135

CHAPTER I

INTRODUCTION

1.1 Background

Transparent electrode alternatives to metal oxides are desired because of increasing demand for flexible and robust optoelectronic devices that include solar cells, touch screens, and flexible displays. Metal oxides such as cadmium oxide, indium oxide, and indium tin oxide (ITO) have been widely used for more than a half century as transparent electrodes.¹ ITO thin films are the most prominent electrodes due to low electrical resistance and high visible light transmittance,²⁻⁴ but these ceramic films have limited flexibility that leads to cracking, and adhesion problems that are made worse by the thermal mismatch with polymer substrates during deposition.³⁻⁸ Intrinsically conductive polymers (ICPs), such as poly(3,4-ethylenedioxythiophene) [PEDOT], have been studied as transparent electrode alternatives, but they suffer from low transparency and photo-oxidative degradation.^{9,10} Carbon nanotube (CNT) thin films offer a promising alternative to these brittle conductive oxides and low transparency ICPs.

Intense study has followed the discovery of carbon nanotubes (CNTs)¹¹⁻¹³ because of their impressive electrical,¹⁴ thermal,¹⁵ mechanical,¹⁶ structural,¹⁷ and chemical properties.¹⁸ Recently, CNT-based thin films have been investigated as components in electronic devices, including high mobility transistors,^{19,20} sensors,^{21,22} solar and fuel cells,^{23,24} integrated circuits,^{25,26} and transparent conductive thin films.^{27,28} For electronic

This dissertation follows the style of *The Journal of Physical Chemistry C*.

devices, such as touch screens and flexible displays, it is desirable for electrodes to exhibit high transparency and electrical conductivity ($\geq 85\%$ transmittance and $\leq 1 \text{ k}\Omega/\text{sq}$ sheet resistance).²⁷ CNT thin films are an interesting alternative to existing transparent conductive layers, such as brittle and chemically unstable indium tin oxide,^{6,29} low conductivity antimony tin oxide/polymer,³⁰ and low transparency poly(3,4-ethylenedioxythiophene)-poly(styrenesulfonate) [PEDOT-PSS].³¹ Several methods for preparation of CNT thin films have been introduced in recent years, such as vacuum filtration,³²⁻³⁴ transfer printing onto various substrates,³⁵⁻³⁷ spin coating,³⁸ dip-coating,³⁹ direct CVD growth,⁴⁰ air-spraying/brushing,^{27,34,41} rod coating,⁴² electrophoretic deposition,⁴³ and more typical CNT/polymer composites.⁴⁴ Despite their promise, these techniques have some disadvantages with regard to film quality, electrical performance, and processing complexity.⁴⁵

Many of the processing and performance issues associated with nanotube films can be circumvented using a technique known as layer-by-layer (LbL) assembly, which has been extensively used in recent years to produce multifunctional thin films in a controlled manner.⁴⁶⁻⁴⁹ LbL assembly typically produces thin films through electrostatic interactions, by alternately exposing a substrate to positively and negatively-charged materials in aqueous solutions, as shown in **Figure 1.1**. Film thickness is determined by the number of deposition cycles, in which each positive and negative pair deposited is referred to as a bilayer (BL). Additionally, LbL deposition is compatible with most substrates, such as plastic films (*e.g.*, polyethylene terephthalate (PET), polystyrene (PS), and polypropylene), glass slides, silicon wafers, and fibers. A variety of functional thin films have been produced using the LbL technique, including antimicrobial,^{50,51} gas

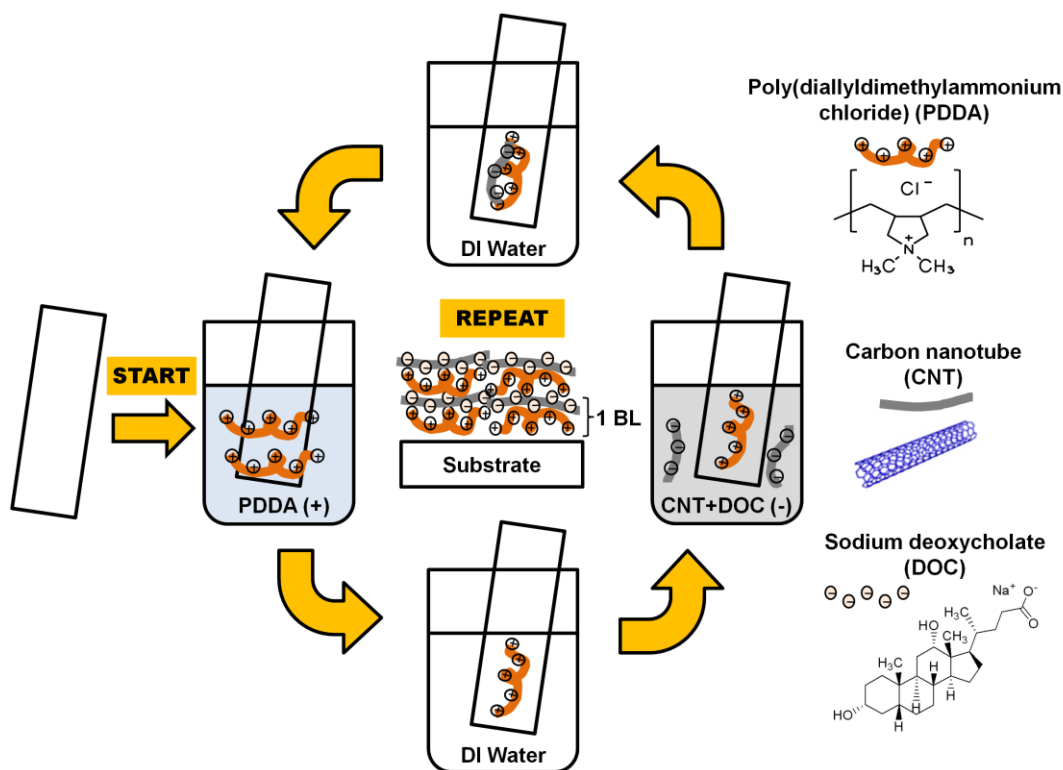


Figure 1.1. Schematic of the LbL process for making conductive thin films that involves dipping a substrate in cationic PDDA and anionically-stabilized CNT mixtures, followed by rinsing with water and drying with filtered air. These steps generate one bilayer (BL) and are repeated to grow a film with a given number of bilayers.

barrier,^{52,53} sensing,⁵⁴ flame retardant,⁵⁵ electrochromics,⁵⁶ drug delivery,⁵⁷ and electrically conductive.⁵⁸⁻⁶⁴ Conductive assemblies made with carbon nanotubes can exhibit ITO-like transparency and sheet resistance,⁶⁰ making them an important topic of study.

1.2 Objectives and Dissertation Outline

The present work focuses on improving the transparency and conductivity of nanotube thin films by alternately depositing CNTs, stabilized with a negatively charged

surfactant, with a transparent polycation using layer-by-layer assembly. The ultimate goal is to develop high conductivity and transparent thin films capable of replacing ITO. The influence of heat treatment, acid treatment, and film composition on transparency and sheet resistance of these assemblies is examined. The ability to tailor thin film resistance can be potentially useful for anti-static films^{33,44} and EMI shielding,^{37,42} in addition to transparent, flexible electrodes. An overview of this research is shown schematically in

Figure 1.2. The key objectives are:

1. To fabricate transparent and conductive nanotube-based thin films with ITO replacement performance, using the LbL technique.
2. To evaluate and understand the microstructure and optoelectronic properties of CNT-based LbL assemblies as a function of the number of bilayers, CNT type, and the type of post treatment (heat treatment, acid treatment, etc.).

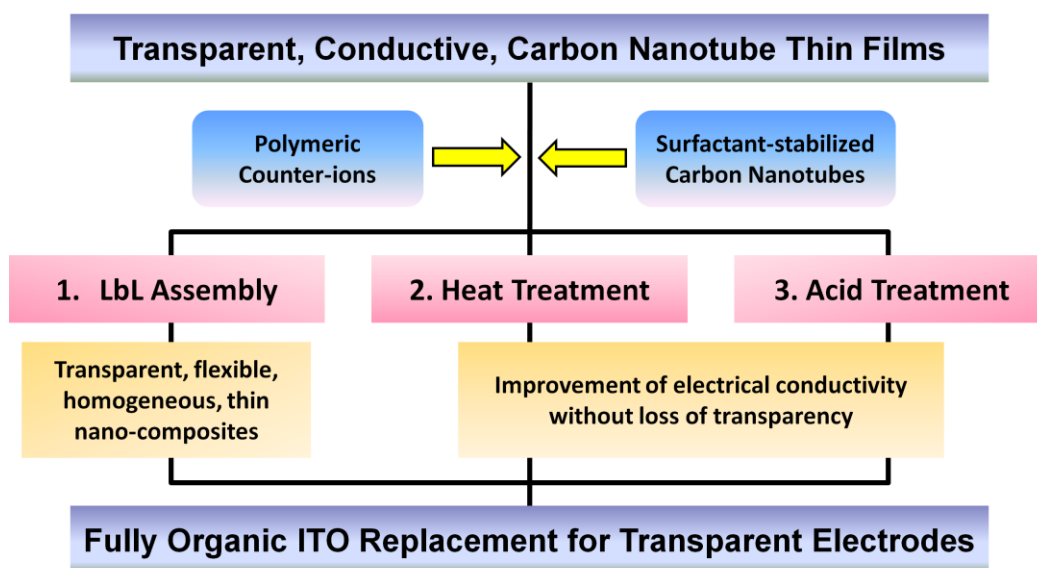


Figure 1.2. Overview of the carbon nanotube-based electrode research described in this dissertation.

3. To confirm the super flexibility and electrochemical stability of CNT-based LbL assemblies are relative to ITO thin films.

Chapter II is a literature review of transparent conductive thin films and LbL assembly. A thorough background of the current technology with regard to transparent and conductive thin films is provided. The LbL assembly basics, along with a survey of the functionality achieved with these thin films, is the second part of this chapter.

Chapter III describes the influence of CNT type on transparency and electrical conductivity of LbL thin films. Three different types of nanotubes are compared: (1) multi-walled carbon nanotubes (MWNTs), (2) few-walled carbon nanotubes (FWNTs), and (3) single-walled carbon nanotubes (SWNTs). In this chapter, a solution of poly(diallyldimethylammonium chloride) [PDDA] and aqueous suspensions of nanotubes stabilized by deoxycholate (DOC) were used to fabricate LbL assemblies. Optoelectronic performance is characterized, along with film growth, component concentration, microstructure, and surface morphology.

Chapter IV examines the heating effect on optoelectronic performance of CNT-based LbL thin films. Thermogravimetric analysis (TGA) was performed on each component of these assemblies, and the fully assembled CNT thin film, in order to choose a suitable temperature range for heat treatment. The influence of different temperatures and times on sheet resistance and transparency is described. Changes in sheet resistance and optical transmittance were measured before and after heating, along with film thickness and microstructure.

Chapter V evaluates acid treatment of these CNT-based thin films. This treatment was applied to decrease sheet resistance to ITO level. The optoelectronic behavior was characterized before and after acid treatment, using various acid types and time. Additionally, this chapter demonstrates the bending performance of CNT- and ITO-coated plastic films. Cyclic voltammetry was also used to compare the electrochemical stability of these two electrode materials.

Chapter VI provides the conclusions for this work and future research directions. This work establishes CNT-based LbL thin films as a legitimate candidate for ITO replacement. CNT thin films were as conductive and transparent as ITO coatings. Moreover, these films exhibit better bending performance and electrochemical stability. Future work will focus on improving these films by other experiments and examining their use as electric applications including antistatic films, EMI shielding, and flexible antennas.

In Appendix A, a study of electrochromic thin film assemblies that switch from transparent to dark blue in their oxidized and reduced states, respectively, is described. These films were generated by alternately depositing tungstate anions with cationic poly(4-vinylpyridine-co-styrene) [PVP-S]. In an effort to decrease switching time, ITO nanoparticles were incorporated into these tungstate-based assemblies. ITO allows these films to maintain electrical conductivity in both states, which is the source of this faster and more stable switching.

CHAPTER II

LITERATURE REVIEW

2.1 Transparent and Conductive Thin Films

Transparent electrodes continue to be studied because of increasing demand for optoelectronics, such as photodiodes for solar cells and electronic displays (*e.g.*, touch screens and light-emitting diodes). For these electronic devices, transporting electrons to and from the electrode layer is required. In many cases, this electrode must transmit visible light because it is applied directly onto the surface of a transparent substrate. Therefore, it is desirable for electrodes to exhibit high transparency and electrical conductivity, especially for display applications. Various materials have achieved a combination of conductivity and transparency to satisfy the needs of these optoelectronic applications. **Table 1.1** summarizes the advantages and disadvantages of the various types of transparent electrodes discussed in the following sections.⁶⁵

2.1.1 Metal Thin Films

One group of transparent electrodes is thin films of metals such as silver (Ag), gold (Au) or copper (Cu). Since first being prepared by vapor deposition on an amorphous substrate in 1969, these metal thin films have been investigated with film thicknesses from 10 to 150 nm.⁶⁶ Unfortunately, these films are soft, porous, catalytically active, chemically reactive, and sometimes poorly adherent to substrates. Metal thin film electrical resistivity is quite low ($< 3.0 \times 10^{-6} \Omega \cdot \text{cm}$) and thickness dependent, and optical

Table 1.1: Summary of Various Types of Transparent Electrodes and Their Potential Applications (reproduced from [65])

	advantages	disadvantages	applications
carbon nanotube	highly flexible neutral color low haze low reflection can be doped solution processable cheap in bulk chemically stable	relatively high sheet resistance for solar cell and large-scale display applications	touch screen EPD flexible OLED LCD IR device EC, EL display
graphene	flexible, neutral color potentially low cost, continuous improvement of conductivity can be doped potentially solution processable low surface roughness	relatively high sheet resistance for solar cell and large-scale display applications	touch screen flexible OLED
metal nanowire or thin film (i.e., Ag or Au)	low sheet resistance large light scattering mechanically flexible surfactant-free processing solution processable	relatively high haze value high surface roughness poor chemical stability	mainly solar cells
PEDOT	flexible mature solution processable	relative high sheet resistance chemically sensitive color	surface modification for nanowire or nanotube network electrode
ITO, IZO	mature low sheet resistance high transparency solution processed ITO particle or ITO nanowires are under study	costly poor mechanical properties high reflection	optoelectronic devices on rigid substrates

properties are also thickness dependent, but not sufficient for transparent applications.⁶⁷ The metal deposition on the substrate starts from metallic nuclei, so electrical conduction is only possible for films that exceed the level where large-scale coalescence begins (**Figure 2.1(a)**).⁶⁶ Further deposition is needed to create a continuous metal film with stable resistivity. **Figure 2.1(b)** shows resistivity data for evaporated Au films before and after annealing at 350 °C for 15 to 30 min.⁶⁸ The resistivity of the as-deposited film drops sharply with increasing thickness and reaches a minimum value of $\sim 3.0 \times 10^{-6} \Omega \cdot \text{cm}$ beyond a 150 nm thickness. After heat treatment, resistivity generally decreases, especially at small thickness, and approaches the bulk value. This resistivity is much smaller than the lowest resistivity of doped metal oxide- or fully organic-based conductive thin films described in the next sections.

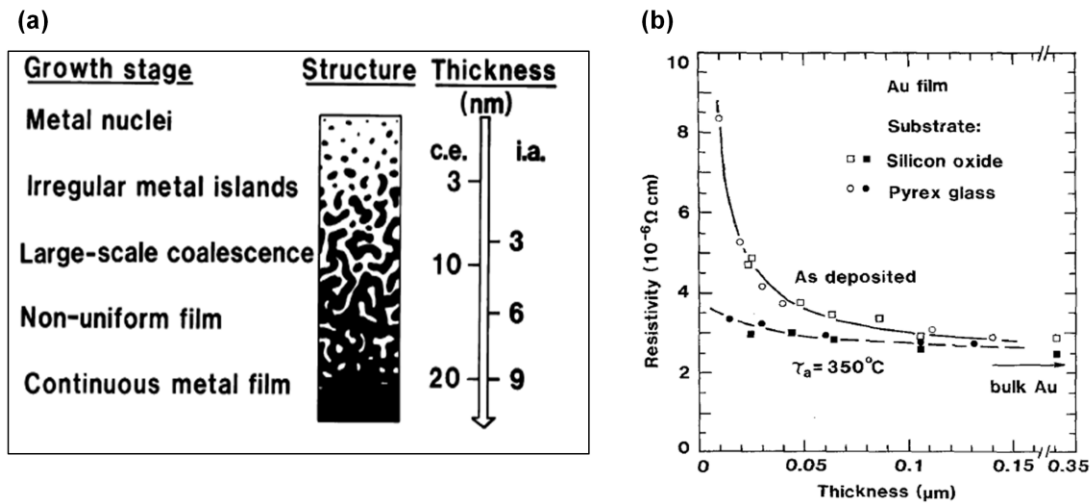


Figure 2.1. (a) Survey of growth stages, structures, and thickness scales for Au thin films deposited on glass by conventional evaporation and ion-assisted evaporation (reproduced from [66]). (b) Thickness-dependent electrical resistivity of Au films on two different substrates, in as-deposited state and after annealing at 350 °C (arrow: the resistivity of bulk Au, reproduced from [68]).

Figure 2.2(a) shows the typical transmittance and reflectance of evaporated Ag thin films for the wavelength range from 350 to 1,600 nm.⁶⁹ The 6 nm thick film is in the irregular metal islands regime, but the reflectance shows metallic behavior at $t > 9$ nm. For these films, the transmittance is $< 55\%$ at 500 nm, which is too low to use them as transparent electrodes for optoelectronic applications. Several techniques have achieved lower resistivity at small thickness.⁷⁰ Transmittance, however, has been reported to be difficult to increase to sufficient values for optoelectronics. Although several methods have been introduced on Au and Ag films in order to tailor the transmittance, they are not satisfactory for most optoelectronic applications. Recently, a remarkable increase in light transmittance was introduced through metallic sub-wavelength hole arrays. The influence of 250 nm diameter nanoholes on transmittance through Au films is shown in **Figure 2.2(b)**.⁷¹ Water-soluble Au nanoparticles have also been utilized to produce patterned,

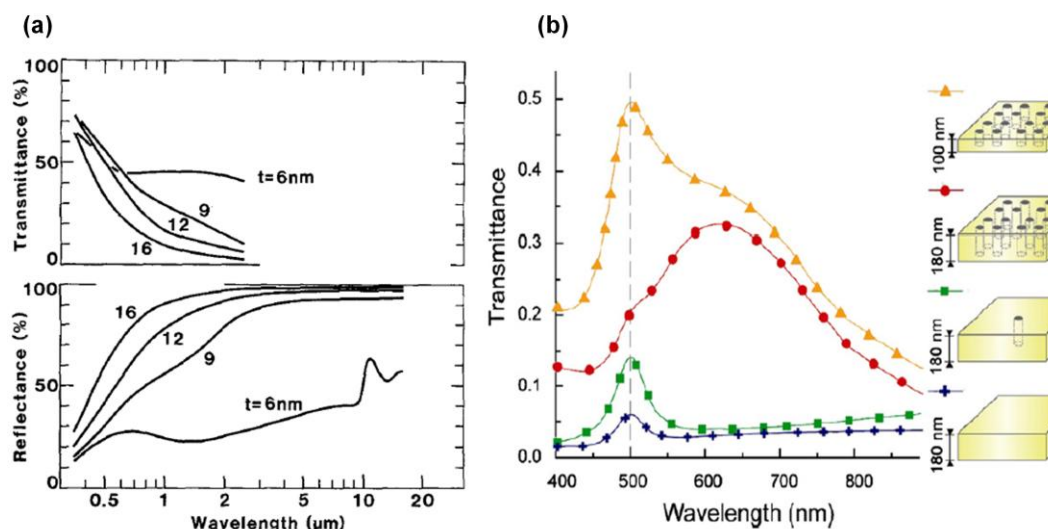


Figure 2.2. (a) Transmittance and reflectance of Ag films with different thicknesses on glass substrates (reproduced from [69]). (b) Transmittance of Au films with the sub-wavelength holes, which lead to extraordinary transmittance in a band centered at 615 nm (reproduced from [71]).

nanostructured conductive films.⁷² These films achieved very high transparency, but also had very high resistivity 10^8 – 10^9 $\Omega\cdot\text{cm}$. Multilayer coatings have achieved high transmittance, using one or several dielectric layers with high refractive index species (*e.g.*, TiO_2 or ZnO),^{73,74} but these layers may have an undesired doping effect. **Figure 2.3** illustrates the increase in transmittance of $\text{TiO}_2/\text{Ag}/\text{TiO}_2$ films and improvement of optoelectronic property in $\text{ZnO}/\text{Ag}/\text{ZnO}$ films.

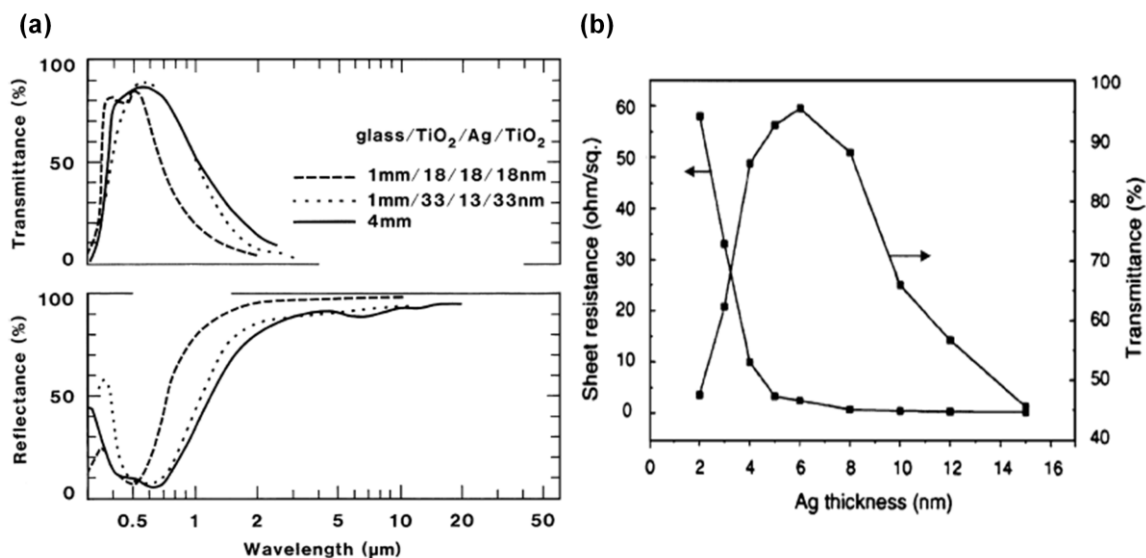


Figure 2.3. (a) Transmittance and reflectance of $\text{TiO}_2/\text{Ag}/\text{TiO}_2$ coatings (reproduced from [73]). (b) Sheet resistance and maximum transmittance as a function of Ag thickness in $\text{ZnO}(20\text{ nm})/\text{Ag}/\text{ZnO}(20\text{ nm})$ coatings (reproduced from [74]).

2.1.2 Doped Transition Metal Oxide Thin Films

Doped, wide-bandgap transition metal oxide semiconductors are another class of transparent electrode materials. Inspired by the behavior of cadmium oxide in 1951, this group of materials (primarily In_2O_3 , SnO_2 or ZnO) have been widely investigated due to

their high electrical conductivity and optical transmittance.¹ These studies ultimately lead to the development of doped $\text{In}_2\text{O}_3\text{:Sn}$ (also known as indium tin oxide or ITO), which has excellent electrical and optical properties.⁷⁵ These films are hard, dense, strongly adherent to glass, and chemically inert, relative to metal thin films. Most common oxide semiconductor materials, such as ZnO:Al ,⁷⁶ $\text{SnO}_2\text{:Sb}$,⁷⁷ ZnO_x ,⁷⁸ and ITO,⁷⁹⁻⁸¹ have very low resistivity ($< 5 \times 10^{-4} \Omega\cdot\text{cm}$). Most current optoelectronic devices use these doped metal oxide materials. ITO remains the most widely used and studied oxide, along with $\text{SnO}_2\text{:F}$ and ZnO:Al , for transparent electrodes. Flat panel displays use ITO as a front electrode,^{82,83} and ITO layers can be directly coated on flexible, transparent plastic substrates.⁸⁴ **Figure 2.4** shows that ITO on PET can achieve a resistivity of $5 \times 10^{-4} \Omega\cdot\text{cm}$ and an average visible light transmittance of 80%, when applied by RF magnetron sputtering.⁷⁹

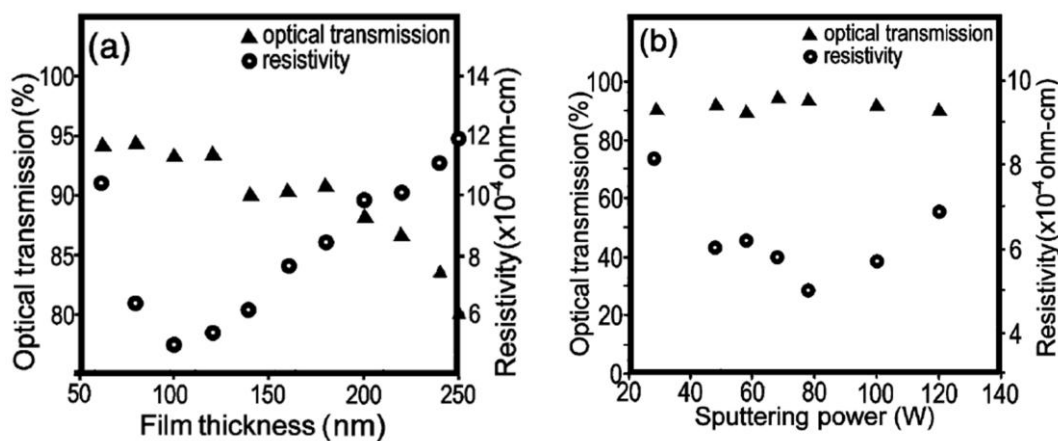


Figure 2.4. Optical transmission and resistivity as a function of (a) ITO film thickness and (b) sputtering power (at 100 nm film thickness) (reproduced from [79]).

Despite having low sheet resistance and high transparency, ITO thin films are not ideal for flexible displays due to their brittleness.³⁻⁵ Additionally, the difference in thermal expansion coefficient and elastic properties of ITO films and polymer substrates results in large mechanical stresses.⁴ Flexing an ITO coated PET film causes stress cracks that reduce its electrical conductivity. Several studies have examined the effect of deflection on the electrical resistivity of ITO on a PET or polycarbonate (PC) substrate, focusing on the relationship between cracking and electrical properties.^{6,7,85} These studies show that cracks are initiated at a strain of 1.28%, when films are stretched, and at a curvature of 10 cm, when films are bent. **Figure 2.5(a)** shows a plot of the film thickness as a function of resistivity, revealing that as the thickness of the film increases, so does sensitivity to bending. **Figure 2.5(b)** shows that average visible light transmittance also diminishes with bending, for a 200 nm-thick ITO film, due to widespread cracks.

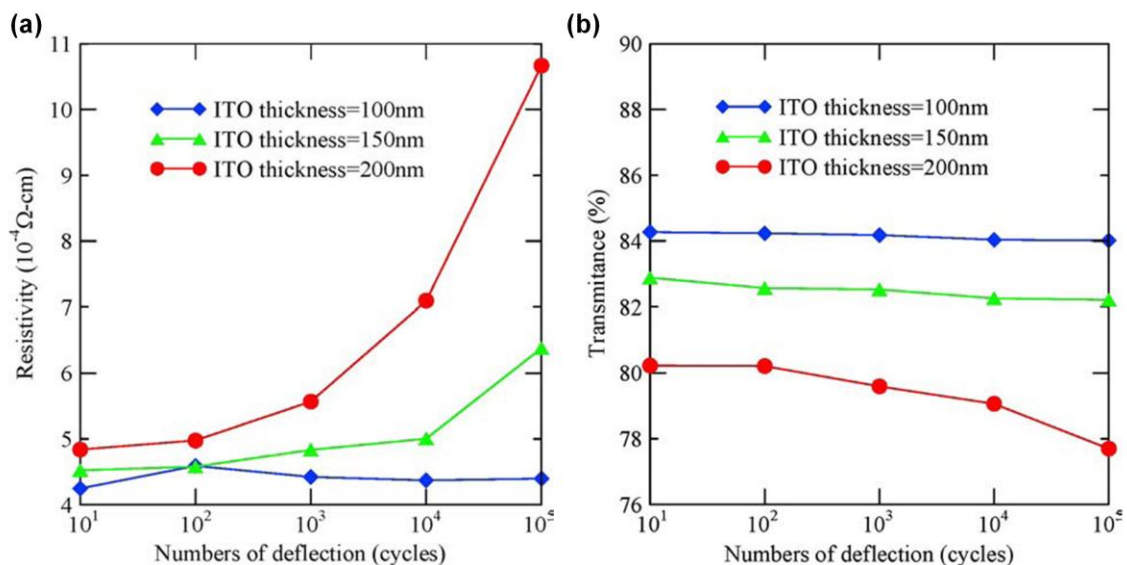


Figure 2.5. Effect of the number of deflection cycles on (a) the film resistivity and (b) the average visible light transmittance for samples of varying thickness (reproduced from [3]).

2.1.3 Fully Organic Conductive Thin Films

2.1.3.1 Polymeric Organic Conductive Films

Since their discovery in 1977,⁸⁶ intrinsically conductive polymers (ICPs) have been heavily studied because of their unique properties.^{31,87} Many ICPs have been applied to electronic devices. Poly(3,4-ethylenedioxythiophene) [PEDOT] is the most widely used ICP due to its relatively high electrical conductivity and photo-oxidative stability, especially when applied from its water-based complex with poly(styrene sulfonate) [PSS].³¹ **Figure 2.6(a)** shows the optoelectronic performance of a PEDOT–PSS coating, indicating good (but not great) sheet resistance ($\rho \approx 1.6 \times 10^{-3} \Omega \cdot \text{cm}$) relative to ITO. ICPs have been evaluated as antistatic coatings (**Figure 2.6(b)**), transparent conductors (**Figure 2.6(c)**),³¹ electrochromic materials,⁸⁸ light emitting diodes,⁸⁹ and transistors.⁹⁰ Photo-oxidative degradation is a key drawback for all ICPs, including PEDOT,^{9,10} due to their conjugated backbones (*i.e.*, alternating double and single bonds). Although ICPs have many advantages, their visible light transmittance and noticeable color is not suitable for most optoelectronic applications.

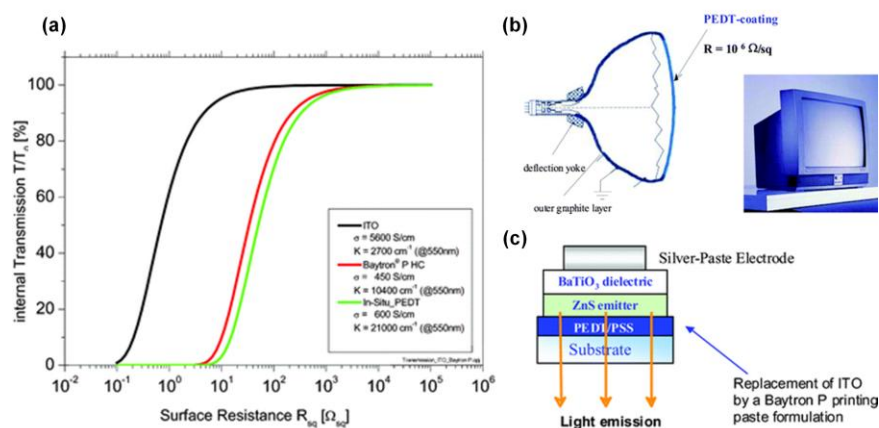


Figure 2.6. (a) Sheet resistance and transparency of PEDOT–PSS relative to ITO. (b) Antistatic coating for cathode ray tubes to prevent dust attraction. (c) Schematic structure of an inorganic electroluminescent device with the traditional ITO layer replaced by a PEDOT–PSS layer (reproduced from [31]).

2.1.3.2 Carbon Nanotube-based Thin Films

Carbon nanotube-based thin films are a more recent alternative to existing transparent conductive layers. Single-walled carbon nanotubes, consisting of one layer of the hexagonal graphite lattice rolled to form a seamless cylinder with a radius up to a few nanometers,¹³ are especially promising. **Figure 2.7** illustrates four methods [vacuum filtration (a),⁹¹ air-spraying (b),⁹² transfer printing (c),³⁷ and rod coating (d),⁴²] for preparing CNT thin films. Spin coating, dip-coating, direct CVD growth, and electrophoretic deposition have also been used to make these films.^{38-40,43} **Figure 2.8** shows an AFM image and optoelectronic behavior of carbon nanotube films prepared by transfer printing. These CNT thin films show good optoelectronic performance, with values in the middle of the range of commercial ITO-coated PET, which typically has 50–200 Ω/sq sheet resistance and $\sim 83\%$ T at 550 nm. Although transfer printing is one of the best methods for producing CNT thin films, there has been difficulty with scale-up, breakage of the film during transfer, and comparatively brittle final films.⁴⁵ These challenges have opened the door for the use of LbL assembly to produce these important CNT films.

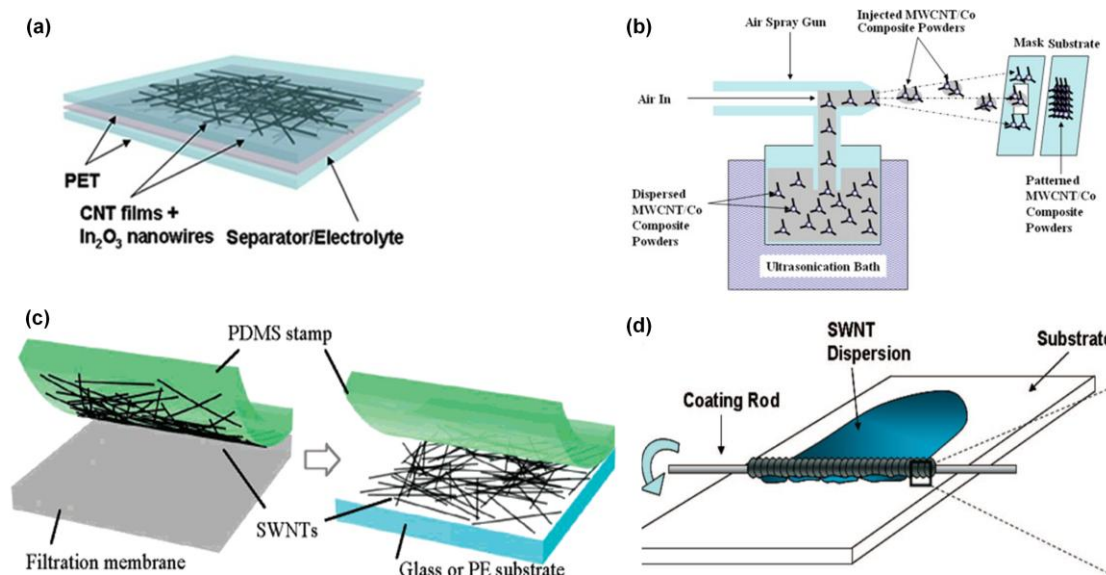


Figure 2.7. Illustration of several methods for carbon nanotube film fabrication: (a) vacuum filtration, (b) air-spraying, (c) transfer printing, and (d) rod coating (reproduced from [91], [92], [37], and [42], respectively).

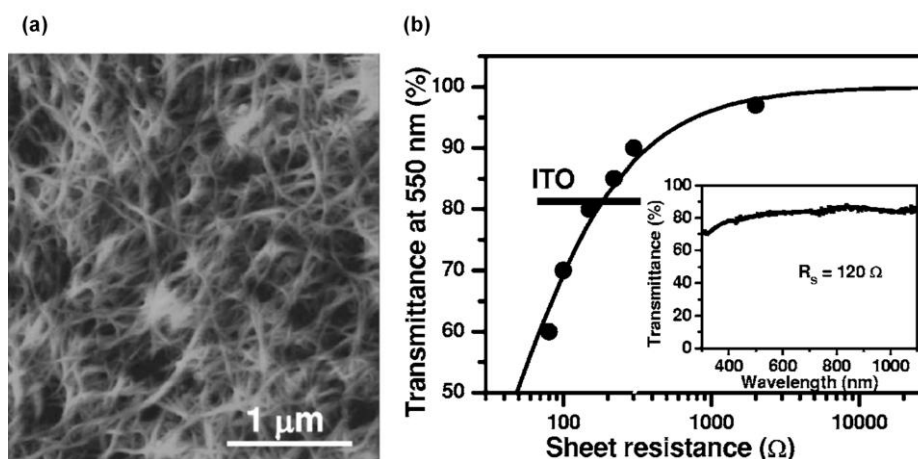


Figure 2.8. (a) AFM image of a nanotube film with $R_s = 200 \Omega/\text{sq}$ on a glass slide and film thickness of 25 nm. (b) Optoelectronic behavior (transmittance at 550 nm vs. sheet resistance) of nanotube films with different thickness on PET substrates. The bold line shows the performance of commercially available ITO films on PET substrates. The inset shows transmittance of a nanotube film with $R_s = 120 \Omega/\text{sq}$. (reproduced from [36]).

2.2 Layer-by-Layer Assembly

2.2.1 *From Langmuir-Blodgett to Layer-by-Layer Assembly*

Many material studies in the last three decades have investigated nano-scale composites with metallic, inorganic, organic, polymeric, and biological components. These nanocomposites make it possible to create synergy by combining two or more materials of desired properties, but it is also known that it is difficult to develop methods to tailor nano-scale assemblies. Moreover, polymer thin films have been increasingly explored for well-defined surfaces and interfaces in recent years. These polymer thin films are formed on substrates, due to balanced interactions between substrate, polymer (or its precursor), and other components. It is possible to consecutively deposit single molecular layers and to form multilayers on a substrate. In order to prepare uniform and homogeneous thin films, several nanofabrication methods have been developed, such as chemical vapor deposition, electron beam induced deposition, colloidal methods, and molecular beam epitaxy.⁹³ Many of these approaches have disadvantages; among these are high operating costs to use these techniques and limitation of the range of organic materials, particularly in the combination of organic and inorganic materials.⁴⁷

The Langmuir-Blodgett (LB) technique involves the deposition of self-assembled amphiphilic monolayers onto a substrate from a water surface. This methodology has been used to fabricate (with angstrom precision) controlled nanostructure films since the 1930's.⁹⁴ The LB technique, however, has limitations with respect to substrate size and applying non-amphiphilic material. There are also issues with film quality and stability.⁹⁵ These limitations are too severe to be useful for practical applications. In an effort to overcome the challenges associated with LB films, the LbL method was developed by

alternating substrate exposure to oppositely charged polyelectrolytes.^{49,95} Any charged nano-scale objects, such as molecular aggregates, clusters, or colloids, are also suitable for this deposition method. Furthermore, the LbL process is largely independent of the nature, size, and topology of the substrate. This is a classic bottom-up nanofabrication technique that has grown in popularity for the past 20 years, due to its simplicity and versatility.

2.2.2 *Introduction to Layer-by-Layer Assembly*

2.2.2.1 Mechanism and Process

Uncertainty remains about the driving force for LbL assembly, although it is widely accepted that the multilayer buildup depends on the electrostatic attraction between oppositely charged molecules and the entropy gain from small counterions entering the water.⁴⁹ This simple process, shown in **Figure 1.1**, results in polycation-polyanion deposition on a charged substrate. When the strong electrostatic attraction occurs between a charged substrate and oppositely charged molecules in solution, overcompensation of the original surface charge, due to the adsorption of molecules, induces charge reversal on the new surface. When the substrate is exposed to a second solution, oppositely charged molecules are again attracted to the surface. Repetition of adsorption cycles with polyanions and polycations (or other charged ingredients) leads to LbL growth of multifunctional films (**Figure 2.9**).⁴⁸ The driving force for LbL assembly is not limited to electrostatic attractions. Many kinds of physicochemical interactions have been used to assemble films. Metal-phosphate interactions,^{96,97} hydrogen bonding,^{98,99} weak electrostatic interactions with the aid of strong π - π interaction,^{100,101}

various biochemical interactions,^{102,103} charge transfer interactions,¹⁰⁴ and sol-gel reactions¹⁰⁵ have all been successfully used to generate these thin films.

Multilayer structures composed of polyions or other charged molecular or colloidal objects (or both) are grown as shown schematically in **Figures 1.1** and **2.9**. Film deposition on a substrate can be carried out manually or with an automated device, which may provide better control.¹⁰⁶ In most cases, dipping into one solution, rinsing, dipping into the other solution, and rinsing again makes one cycle, yielding one bilayer. Excessive molecules from solution adhering to the surface are removed by the rinsing. This cycle is repeated until the desired number of bilayers has been deposited.

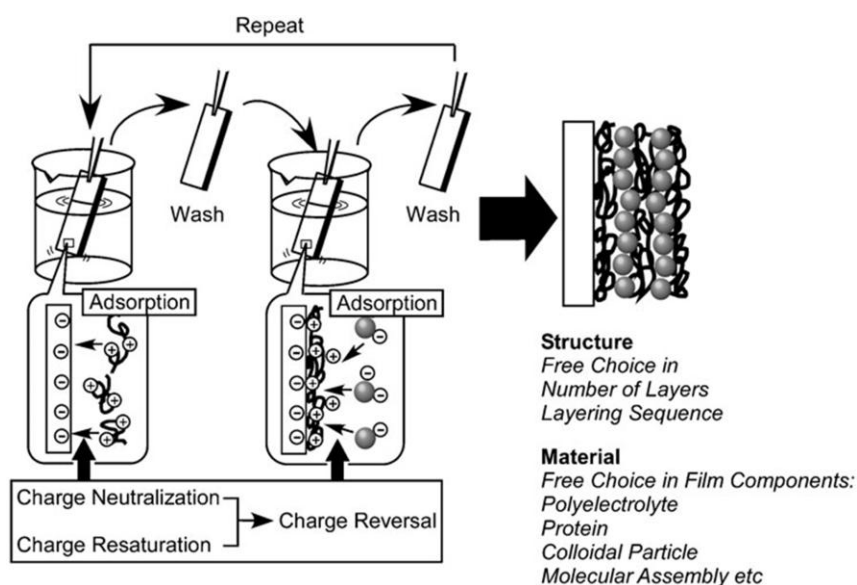


Figure 2.9. Schematic of the electrostatic layer-by-layer self-assembly process (reproduced from [48]).

2.2.2.2 Advantages of LbL Thin Films

One of the major advantages of LbL assemblies is the ability to incorporate several different materials into precise levels within sub-micron films. In principle, there is no limitation to the number of ingredients within LbL films. In addition to conventional polyelectrolytes, various functional materials have been assembled by electrostatic LbL assembly. These unconventional ingredients include biomaterials, especially DNA¹⁰⁷ and proteins,¹⁰⁸ and charged substances like colloidal nanoparticles,^{109,110} metal oxides,^{9,111} clay,^{52,112} nanosheets,^{113,114} and nanotubes.^{60,61,115} Photonic crystals have been built by altering the size of quantum dots (QDs) in successive layers,¹¹⁶ which highlights the power of this technique. **Figures 2.10(a) and (b)** show a graded LbL film on a glass slide made with PDDA and four different size thioglycolic acid-stabilized CdTe QDs with green, yellow, orange, and red luminescence.¹¹⁶ **Figure 2.10(c)** illustrates the LbL assembly procedure for biologically active semiconductor QD (CdTe)-labeled microsphere bioconjugates on 925 nm diameter PS beads.¹¹⁷ Additionally, there are no restrictions with respect to size, shape, and topology of substrate. Assemblies have been grown on fibers, foams, metals, glasses, semiconductors, and numerous polymer films (PET, PS, and polydimethylsiloxane (PDMS), etc.).^{9,52,60,61,108-115,118} The conformal nature of this coating process typically results in uniform coating of every three dimensional surface of a fiber,^{112,119} a core,^{117,120} or a pore¹²¹ (**Figure 2.11**).

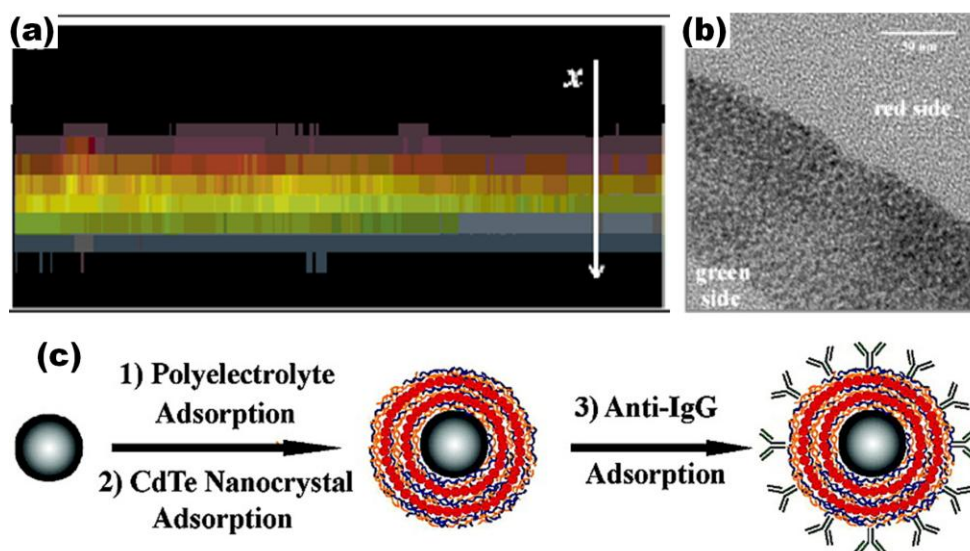


Figure 2.10. (a) Cross-sectional confocal microscopy image of a graded PDPA/CdTe film made of 10 BLs of four different size CdTe QDs (green, yellow, orange, and red; total 40 BLs). (b) TEM cross-section of a graded film made from 5 BLs of green, yellow, and red QDs (reproduced from [116]). (c) Illustration of the LbL procedure used to prepare CdTe QD-microsphere bioconjugates (reproduced from [117]).

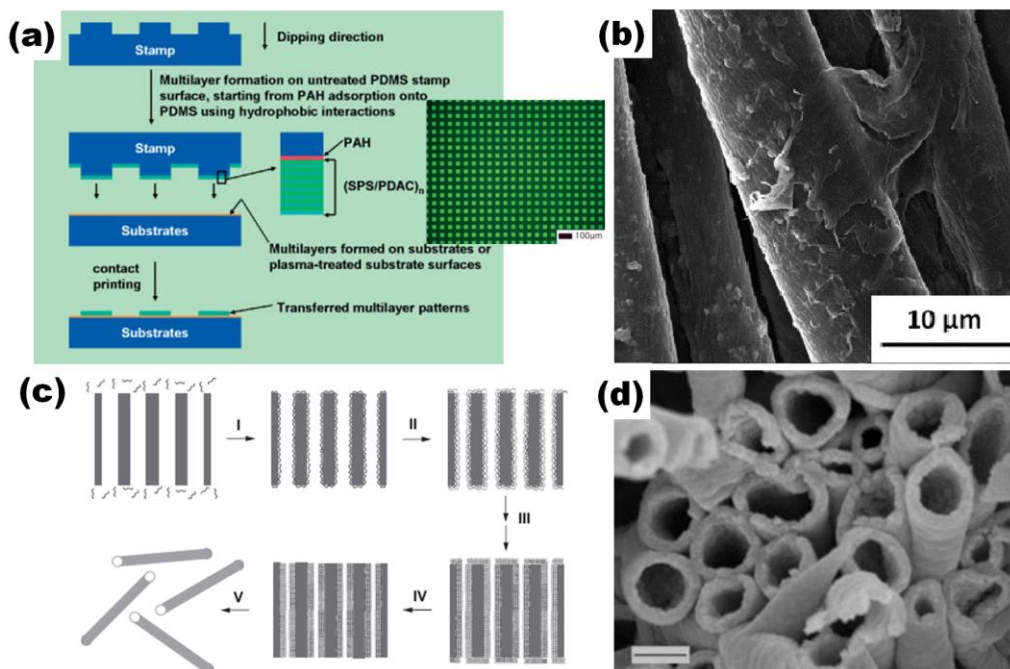


Figure 2.11. LbL coatings on the surfaces of (a) a patterned PDMS stamp, (b) fibers, and (c) polycarbonate porous membrane templates (reproduced from [118], [112], and [121], respectively). (d) The nanotubes prepared in the membranes with 400 nm diameter pores via the LbL process of (c).

2.2.2.3 Characteristics of Layer-by-Layer Films

In addition to the versatile spectrum of LbL assemblies, operating parameters add to the versatility of film characteristics for each assembly. Parameters affecting LbL film growth include surface charge of the substrate, concentration of the solution, pH of the solution, deposition time, rinsing, drying, stacking sequence, humidity, temperature, etc. The first layer is adsorbed by a charged substrate in conjunction with oppositely charged polyions. Therefore, the total amount of at least the first bilayer (up to 5 bilayers) depends on the substrate and its surface treatment (**Figure 2.12(a)**).¹²² The concentration of polyelectrolyte also affects LbL assembly. There is a lower concentration limit below which films will not grow.^{122,123} Adjusting pH can induce changes in the charge density of a polyelectrolyte, resulting in an increase or decrease in film thickness. Greater charge density of the polyelectrolyte will produce thinner films,^{52,112} while lower charge density will result in thicker films.¹²⁴

Figure 2.12(b) shows the thickness as a function of bilayers deposited for films made with clay and different pH of polyethylenimine (PEI).⁵² PEI is highly charged at low pH, suggesting uncoiled rod-like conformation of its chain, which results in thinner deposition. The influence of deposition time on film growth also has been studied using LbL assembly.^{122,125,126} Especially in particle-containing LbL assemblies, longer deposition time can produce thicker LbL thin films. **Figure 2.12(c)** shows a proposed mechanism for clay/polyelectrolyte assemblies with different deposition time. Smaller particle-based LbL assembly exhibits a greater change in thickness with deposition time.¹²⁵ Rinsing is typically used to remove excess material, which can be essential for nanoparticles with low charge.¹²⁷ The drying produces denser LbL assemblies, as well as

improved smoothness of the films, as shown in **Figure 2.12(d)**.^{46,128} Additionally, the influence of stacking sequence,¹²⁹ humidity,¹³⁰ and operating temperature^{131,132} on LbL assemblies have been widely investigated. All of these parameters result in a combined effect, so precise control of parameters should be chosen for the optimal films.

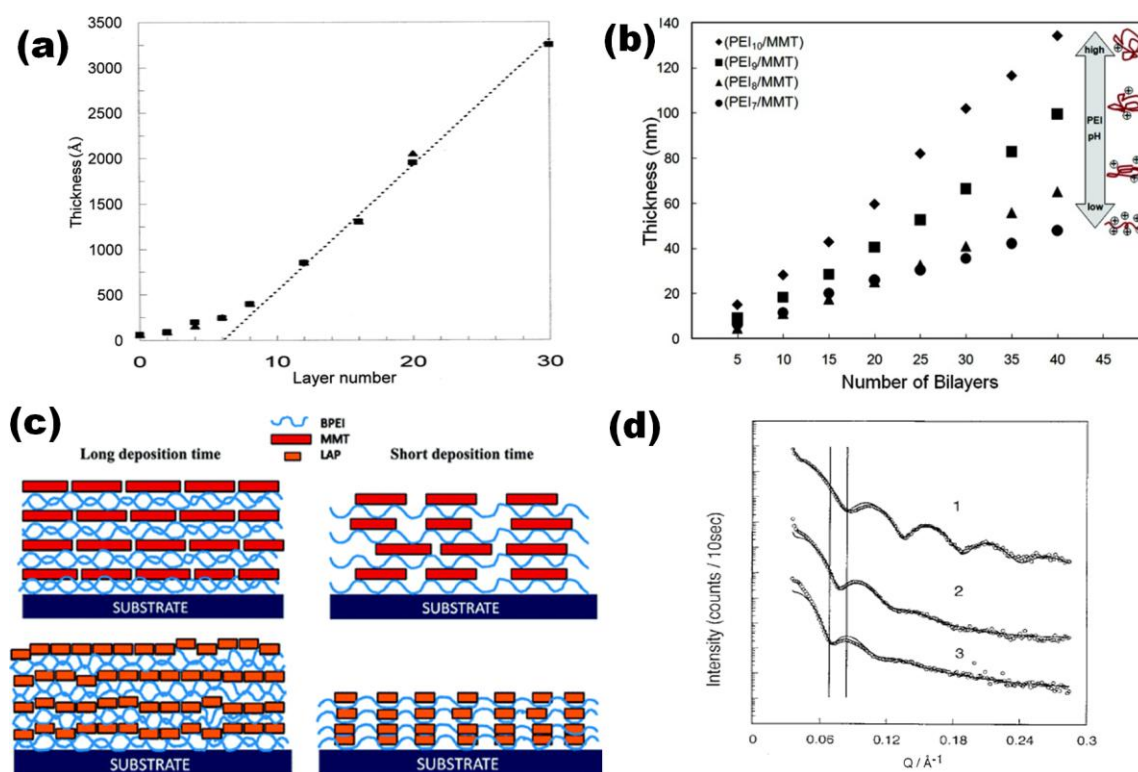


Figure 2.12. (a) Thickness as a function of the number of layers deposited for a PSS/PDDA multilayer on a silicon wafer (reproduced from [122]). (b) Thickness as a function of bilayers deposited for films made with clay and polyethylenimine. (reproduced from [52]). (c) Proposed film growth mechanism for BPEI/MMT and BPEI/LAP with different deposition times. (reproduced from [125]). (d) X-ray reflectivity spectra of three LbL films dried with different methods. Film 1 was dried by spinning after each dipping step. Film 2 was prepared like 1, but was immersed in water and dried in air after the film build-up was completed. Film 3 was dried in air after each dipping step (reproduced from [128]).

2.2.3 Particle-Based Layer-by-Layer Assemblies

As mentioned above, many types of charged molecules and nanoparticles have expanded the LbL spectrum. Many nanoparticles make use of stabilizers to impart the surface charge needed for effective LbL assembly.^{52,107-116} These particles often require additional strong interactions to reduce the minimum charge required, such as π - π stacking for organic dyes,¹⁰¹ aggregate deposition for inorganic colloids,^{111,133} and introduction of charged inorganic platelets like montmorillonite (MMT) clay, which behave as rigid polyelectrolytes, because of their natural surface charge.^{52,112} The most common materials used for LbL assembly are polymers. Polymeric LbL is much less dependent on the substrate, or the substrate charge density, than films made with smaller molecules.¹³⁴ Useful all nanoparticle-based LbL assemblies (**Figure 2.13**) have been successfully produced,^{135,136} but nanoparticle-polymer assemblies are more commonly used.¹⁰⁷⁻¹¹⁶

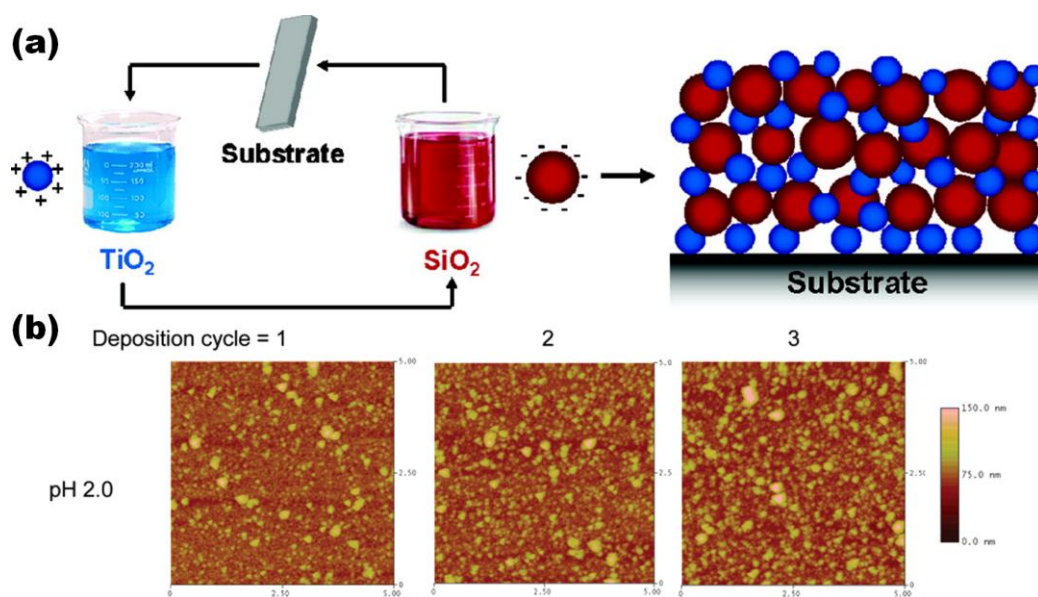


Figure 2.13. (a) LbL assembly with TiO_2 and SiO_2 nanoparticles used (reproduced from [135]). (b) AFM images of all-silica nanoparticle multilayers at pH 2 after 1, 2, and 3 deposition cycles (reproduced from [136]).

CNT-based LbL assemblies are a good example of a polymer-particle system widely studied to fabricate transparent electrodes. Several groups have prepared CNT-based thin films using the LbL method: oxidized individual SWNTs and PEI (denoted as $[\text{PEI}/\text{SWNT}_{\text{ox}}]_n$ where n is the number of BLs),⁵⁸ $[\text{PANI}/\text{SWNT}_{\text{ox}}]$,⁵⁸ $[(\text{PEI}/\text{PAA})(\text{PEI}/\text{SWNT}_{\text{ox}})]_n$,⁵⁹ $[\text{PVA}/(\text{SWNT}+\text{PSS})]_n$,⁶⁰ $[\text{PVA}/\text{PSS}]_3[\text{PVA}/(\text{CNT}+\text{PSS})]_n$,⁶¹ $[(\text{PDDA}/\text{PAA})/(\text{SWNT}/\text{PAA})]_n$ with surface-modified SWNTs by an amphiphilic copolymer,⁶² negatively and positively functionalized MWNT,⁶³ $[\text{PDDA}/(\text{SWNT}+\text{naphthalene})]_n$ and $[(\text{SWNT}+\text{pyrene})/\text{PSS}]_n$,⁶⁴ where PANI, PAA, and PVA are polyaniline, poly(acrylic acid), and poly(vinyl alcohol), respectively (**Figure 2.14**). Few studies have examined the influence of nanotube type on transparency and conductivity,⁶¹ or methods to improve these values in CNT LbL films.¹³⁷ The present dissertation explores methods to improve the transparency and electrical conductivity of these potential ITO replacement materials.

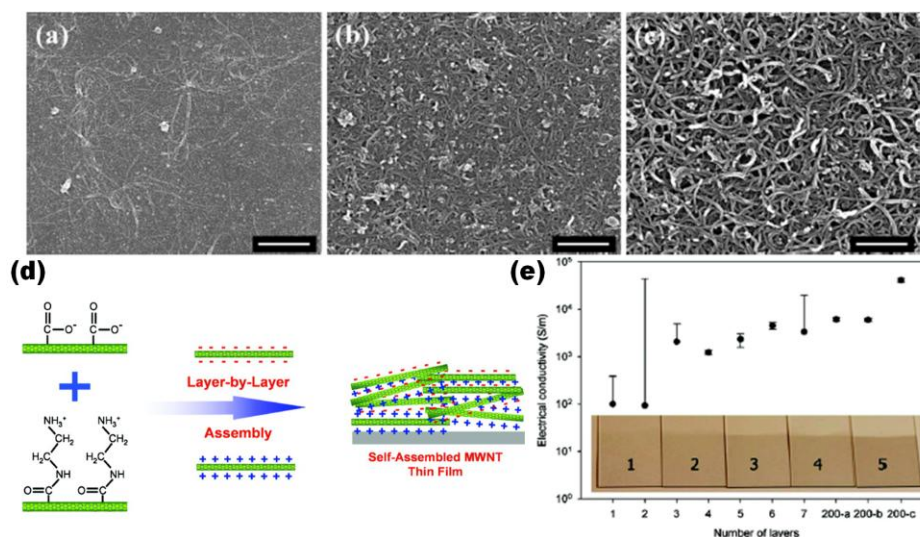


Figure 2.14. SEM morphology of (a) $[(\text{PVA}/\text{PSS})_3(\text{PVA}/\text{SWNT}-\text{PSS})_{15}]$, (b) $[(\text{PVA}/\text{PSS})_3(\text{PVA}/\text{TWNT}-\text{PSS})_{25}]$, and (c) $[(\text{PVA}/\text{PSS})_3(\text{PVA}/\text{MWNT}-\text{PSS})_{17}]$ (reproduced from [61]). (d) MWNT thin film assembled with positively and negatively charged MWNTs (reproduced from [63]). (e) Electrical conductivity of $[\text{PVA}/(\text{SWNT}+\text{PSS})]_n$ as a function of the number of bilayers (reproduced from [60]).

CHAPTER III

INFLUENCE OF CARBON NANOTUBE TYPE ON TRANSPARENCY AND ELECTRICAL CONDUCTIVITY OF THIN FILM ASSEMBLIES*

3.1 Introduction

Chapter III is focused on evaluating nanotube thin film transparency and electrical conductivity by alternately depositing various types of CNTs, stabilized with a negatively charged surfactant, with a polycation using LbL assembly. CNTs have impressive electrical properties, which have prompted significant effort to utilize them as electrodes, especially in flexible electronic devices. For these devices, it is desirable for electrodes to exhibit high visible light transparency and low sheet resistance. Although CNT thin films have been generated by several methods,³²⁻³⁴ they tend to exhibit problems related to fabrication and final properties. LbL assembly is a powerful coating technique, widely used to deposit multifunctional layers in a homogeneous and controlled manner.⁴⁶⁻⁴⁹ Several groups have prepared CNT-based thin films using the LbL method,⁵⁸⁻⁶⁴ but no study has reported the influence of nanotube type on optoelectronic performance of surfactant-stabilized CNT thin films.

In this chapter, layer-by-layer assembly was used to generate transparent, highly conductive thin films containing carbon nanotubes. Three different types of nanotubes were used: (1) MWNTs, (2) a mixture of single, di-, and triwalled nanotubes, also known as FWNTs, and (3) purified SWNTs. Thin films, less than 100 nm thick, were created by

* Reprinted with permission from “High electrical conductivity and transparency in deoxycholate-stabilized carbon nanotube thin films” by Yong Tae Park *etc.*, *J. Phys. Chem. C* **2010**, *114*, 6325-6333. ©2010 ACS.

alternately exposing a substrate to positively and negatively charged solutions. Poly(diallyldimethylammonium chloride) [PDDA] was used as the cationic layer, in conjunction with deoxycholate (DOC), as a negatively-charged nanotube stabilizer, to deposit these various types of CNTs. DOC is known to be an effective dispersing agent for CNTs in water.^{138,139} As a result, CNT damage from severe chemical or mechanical dispersion, such as oxidation or ultrasonic treatments, can be avoided.¹³⁸ Although other methods for making CNT transparent conductive thin films have been previously reported,^{27,28,32,33,35-45} only LbL assembly allows for film thickness and composition to be precisely tailored at the nanometer level under ambient conditions. The deposition sequence outlined in **Figure 1.1** was used to assemble films denoted as [PDDA/(CNT+DOC)]_n, where *n* is the number of bilayers deposited. Films with sheet resistance below 2 kΩ/sq (electrical conductivity (σ) > 150 S/cm with thickness ~ 40 nm) and transparency greater than 85% were deposited, with larger diameter nanotubes generating thicker and less transparent films. This combination of simple processing, high conductivity, and high transparency should make these films very attractive for a variety of flexible electronics applications.

3.2 Experimental

3.2.1 Materials

MWNTs (12–15 nm outer and 4 nm inner diameters and 1+ μm length, C ≥ 95 wt%) were provided by Bayer MaterialScience (Leverkusen, Germany). A mixture of single, di-, and triwalled carbon nanotubes (XM grade), referred to as FWNTs in this work, and purified SWNTs (1 nm diameter and 0.1–1 μm length, C ≥ 85 wt%) were

purchased from Unidym Inc. (Menlo Park, CA). PDDA, with a molecular weight of 100,000-200,000 g/mol, and sodium deoxycholate (DOC, $C_{24}H_{39}NaO_4$, $\geq 98\%$) were purchased from Aldrich (St. Louis, MO). Sulfuric acid (H_2SO_4 , 98%), hydrogen peroxide (H_2O_2 , 30%), methanol (99.8%), acetone (99.5%), and hydrochloric acid (HCl, 37%) were also purchased from Aldrich and used as received.

3.2.2 Layer-by-Layer Assembly

A cationic 0.25 wt% PDDA aqueous solution was prepared by dissolving in 18.2 M Ω deionized water. The anionic solution was prepared by dissolving 0.05 wt% CNTs in deionized water containing 2 wt% DOC, followed by mild sonication for 20 min to remove large CNT bundles and impurities. All solutions were used without altering pH. Fused quartz slides (Structure Probe Inc., West Chester, PA) were prepared by immersing them into a piranha solution (7:3 mixture of H_2SO_4 and H_2O_2) and sonicating for 30 min, followed by thoroughly rinsing with deionized water and drying with filtered air.¹⁴⁰ Single-side polished (1 0 0) silicon wafers (University Wafer, South Boston, MA) were cut to size, rinsed with ethanol-acetone (1:1), followed by deionized water, and finally dried with filtered air.¹⁴¹ PET (trade name ST505 by DuPont Teijin, Tekra Corp., New Berlin, WI) and PS (trade name ST311125 by Goodfellow Cambridge Ltd., Cambridge, UK) substrates were cut to size, followed by rinsing with methanol, then deionized water, and drying with filtered air. The quartz crystals were cleaned with an oxygen plasma etcher prior to use. The cleaned polymer substrates were then corona treated with a BD-20C Corona Treater (Electro-Technic Products Inc., Chicago, IL). Corona treatment is used to oxidize the surface of the polymers, which helps the polycationic species to better

adhere.¹⁴² Clean substrates were first immersed into the PDDA solution for 5 min, followed by rinsing with deionized water and drying with filtered air. Immersion into the DOC-stabilized CNT suspension for 5 min came next, followed by rinsing and drying. These four steps comprise one cycle, yielding one BL. For each subsequent cycle, the immersion time for both aqueous mixtures was reduced to one minute and repeated to deposit the desired number of BLs. Following deposition, all films were stored in a dry box for a minimum of 12 h prior to testing.

3.2.3 Characterization of Film Growth

Thickness measurements were performed on silicon wafers. A PHE-101 Discrete Wavelength Ellipsometer (Microphonics, Allentown, PA) was used at a fixed wavelength of 632.8 nm and an angle of 65°. An F20 Reflectometer (Filmetrics Inc., San Diego, CA) was also used to confirm the thickness with the same refractive index as that used in ellipsometry. The weight of each deposited layer was measured with a Maxtek (East Syracuse, NY) Research Quartz Crystal Microbalance (QCM) and 5 MHz gold-electrode quartz crystals. Absorbance and transmittance of deposited films on fused quartz slides were measured between 250 and 850 nm with a USB2000 UV-Vis spectrometer (Ocean Optics, Dunedin, FL). All absorbance values in the text are for one-side coating (*i.e.*, absorbance from 2 sides was halved). TGA was performed with a Q50 Analyzer (TA Instruments, New Castle, DE). Each sample was run under air or nitrogen gas from room temperature to 800 °C, at a heating rate of 20 °C/min. TGA was used to determine nanotube concentration using a previously established procedure.⁶⁰

3.2.4 Microscopic Imaging

Thin film cross sections were imaged with a JEOL 1200 EX TEM (JEOL USA Inc., Peabody, MA) with an operating voltage of 100 kV. TEM specimens were embedded in an epoxy resin comprised of Araldite 502 modified bisphenol A and Quetol 651 ethylene glycol diglycidyl ether, along with dodecenyl succinic anhydride hardener (2:1:1 mole ratio) and benzyldimethylamine accelerator (0.2 ml per 10 g of total epoxy resin), which were all purchased from Electron Microscopy Sciences (Hatfield, PA). The specimens were sectioned down to ~ 90 nm with a Reichert-Jung Ultracut E 7017014 and placed on 300 mesh nickel grids to dry prior to imaging. Surface images were obtained with a Quanta 600 FE-SEM (FEI Co., Hillsboro, OR) at an operating voltage of 10 kV.

3.2.5 Electrical Property Characterization

Sheet resistance was measured using a Signatone Pro4 Four-Point Probe (Gilroy, CA) with 0.4 mm probe tip diameter and 1.0 mm tip spacing, E3644A DC Power Supply (Agilent Technologies Inc., Santa Clara, CA), and a Digital Multimeter (Keithley Instruments, Cleveland, OH). Voltage and current values were collected in LabVIEW using a SCB-68 I/O connector (National Instruments Inc., Austin, TX). Correction factors were also tabulated because the dimensions of the substrate influence sheet resistance:

$$R_s = (V/I)CF_1CF_2 \quad (1)$$

where R_s is the sheet resistance, V is the voltage, I is the current, CF_1 is the correction factor based on the ratio between substrate diameter and probe tip spacing, and CF_2 is the correction factor based on the ratio between thickness and probe tip spacing.¹⁴³

3.3 Results and Discussion

3.3.1 Growth of Carbon Nanotube Assemblies

Film thickness was measured using ellipsometry after every two PDPA/(CNT+DOC) bilayers were deposited on a Si wafer. All three CNT systems exhibit linear growth, as shown in **Figure 3.1(a)**. These growth trends confirm successful combination of PDPA and CNT within the film and constant composition up to 20 BLs. In addition, **Table 3.1** shows that SWNT-based films grow much thinner than FWNT and MWNT, suggesting that the film thickness depends on the radial size of the CNT. Much thicker growth than 4.9 nm per bilayer may be expected from the MWNT-based films, but each measurement is an average thickness over an area containing many nanotubes that have empty areas between them. Furthermore, subsequent layers likely settle into some of these thinner areas left from a prior deposition step.

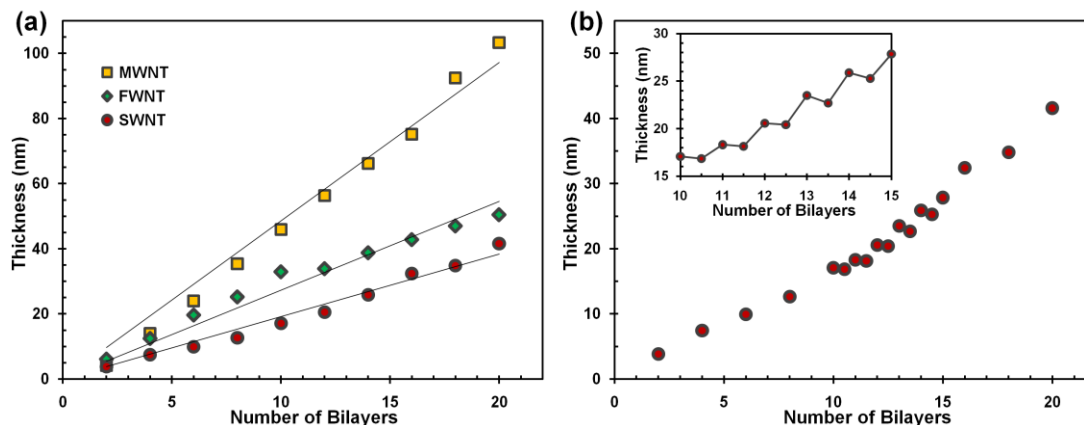


Figure 3.1. (a) Film thickness of three types of $[PDPA/(CNT+DOC)]_{20}$ thin films as a function of the number of bilayers deposited, as determined by ellipsometry. (b) Film thickness of a $[PDPA/(SWNT+DOC)]_{20}$ thin film as a function of the number of bilayers deposited. The inset is the film thickness from 10 to 15 BLs, where a half bilayer corresponds to PDPA deposition.

TABLE 3.1: Growth, Density, and Composition of PDDA/(CNT+DOC) Assemblies

LbL System	thickness per BL (nm)	density (g/cm ³)	PDDA (wt%)	CNT+DOC (wt%)
PDDA/(MWNT+DOC)	4.86	1.63	9.3	90.7
PDDA/(FWNT+DOC)	2.73	1.37	9.7	90.3
PDDA/(SWNT+DOC)	1.85	2.12	9.5	90.5

Figure 3.2(a) shows the mass growth of these three CNT systems, as measured by QCM. Similar to the ellipsometric film thickness, film mass increases linearly with bilayers deposited, suggesting constant composition during growth. The amounts of PDDA and SWNT+DOC adsorbed onto the quartz crystal in each deposition cycle were estimated to be 0.037 and 0.35 $\mu\text{g}/\text{cm}^2$, respectively, as shown in **Figure 3.2(b)** and **Table 3.1**. With the average thickness of each PDDA/(CNT+DOC) system from ellipsometry, QCM mass data allows the density of each film, as well as composition, to be calculated (see **Table 3.1**). The [PDDA/(SWNT+DOC)]₂₀ film appears to have the highest density, while having a similar CNT concentration as the other two systems, suggesting that the PDDA/(SWNT+DOC) system has a more tightly packed nanostructure. The [PDDA/(FWNT+DOC)]₂₀ films likely produced the lowest density due to reduced bundling relative to the SWNT system, which resulted in greater spacing between neighboring nanotubes (This assertion is supported by the surface images of 2-bilayer films shown in **Figure 3.6**). Additionally, for all three systems, the concentrations of CNT layers were over 90 wt% of the entire 20 BL thin films. This value is somewhat misleading, however, because nanotube deposition is accompanied by a large fraction of DOC stabilizer.

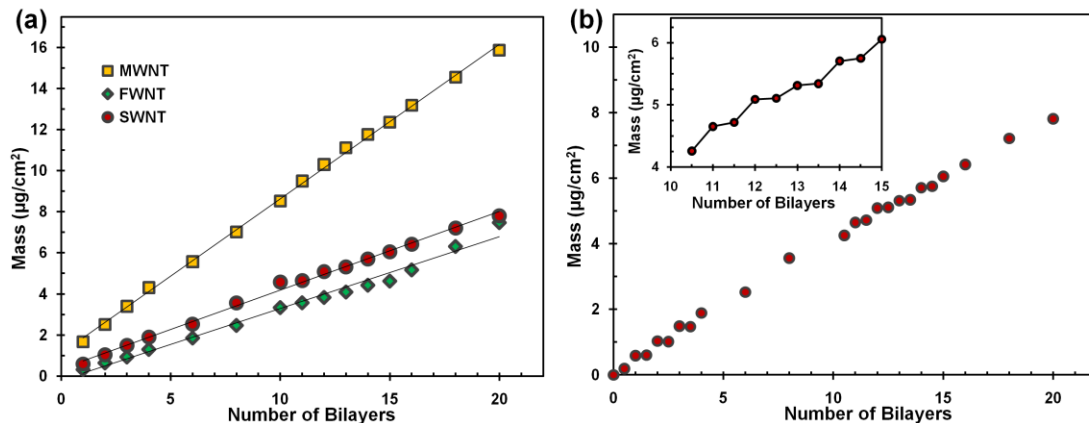


Figure 3.2. (a) Mass growth of three types of $[\text{PDDA}/(\text{CNT}+\text{DOC})]_{20}$ thin films as a function of the number of bilayers deposited, as measured by QCM. (b) Mass growth of a $[\text{PDDA}/(\text{SWNT}+\text{DOC})]_{20}$ thin film as a function of the number of bilayers deposited. The inset is the mass change from 10 to 15 BLs, where a half bilayer corresponds to PDDA deposition.

Uncertainty remains about how to accurately measure CNT concentration in these nanocomposite thin films, but TGA provides a reasonable option. The first step in this process is to obtain characteristic peaks for each component of these assemblies (MWNT, FWNT, SWNT, PDDA, and DOC), obtained by subtracting the graph obtained under nitrogen (unreactive) from the graph obtained under air (reactive).⁶⁰ **Figure 3.3** shows these graphs and corresponding characteristic peaks. These peaks are the result of differences in the degradation rate between the two gas environments. As shown in **Table 3.2**, MWNT, FWNT, and SWNT have characteristic peaks at 795, 725, and 620 °C ($T_{\text{C_CNT}}$), respectively, and these values do not overlap with the characteristic peaks of PDDA and DOC. Commercial CNTs are generally composed of ‘crystalline’ and amorphous carbons and some metallic catalyst. Metallic catalyst has the same high temperature behavior under air and nitrogen gas. Amorphous carbon has a lower degradation temperature than the crystalline carbon (*i.e.*, the carbon nanotube itself), suggesting that the nanotube concentration can be estimated from the height of its own

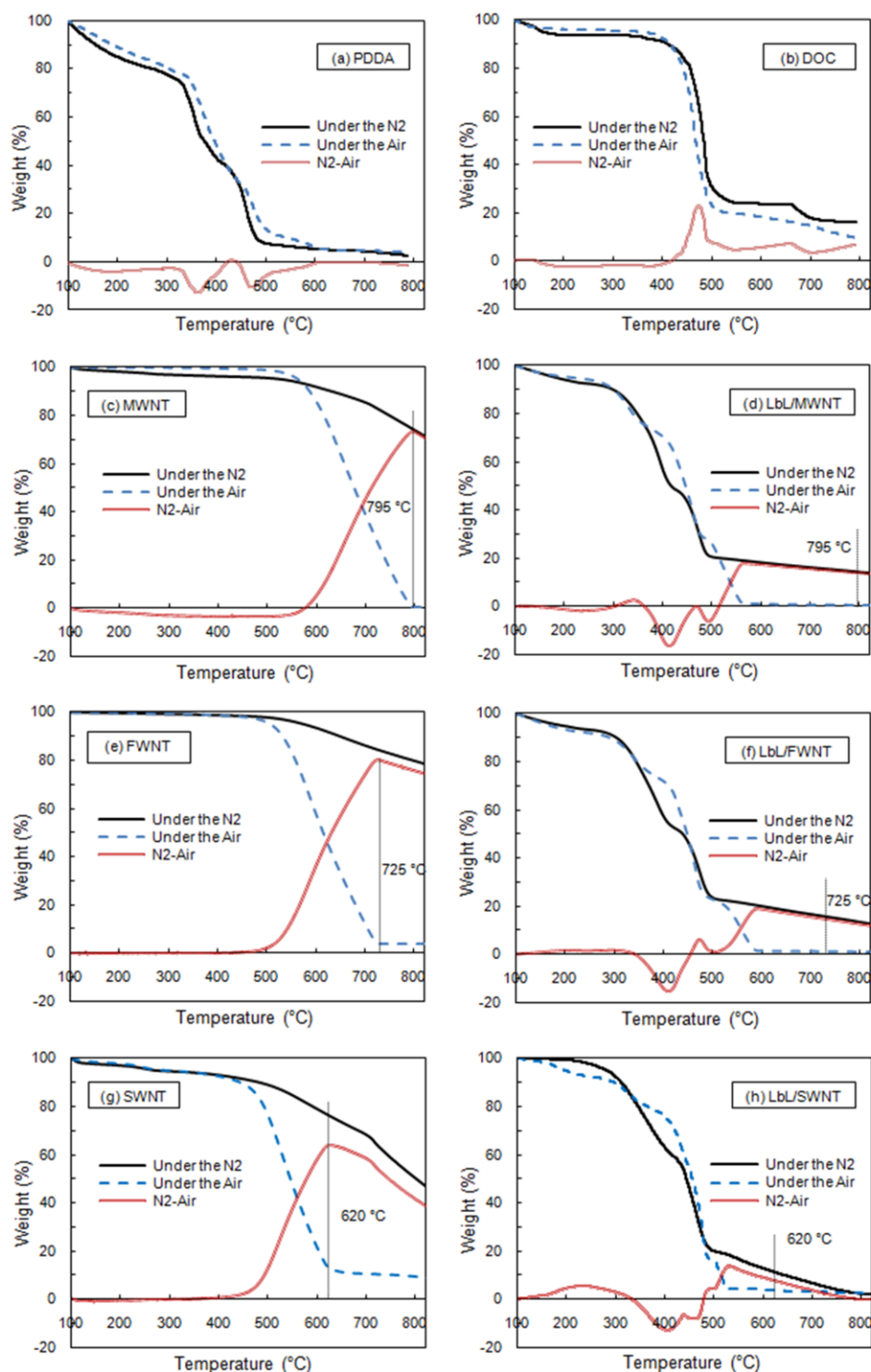


Figure 3.3. Thermogravimetry of each component of CNT-based LbL films and three types of LbL films ((a) PDDA, (b) DOC, (c) MWNT, (d) [PDDA/(MWNT+DOC)], (e) FWNT, (f) [PDDA/(FWNT+DOC)], (g) SWNT, and (h) [PDDA/(SWNT+DOC)]) under dried air and nitrogen gas, respectively. The difference between the air and nitrogen curves is also plotted to reveal the characteristic peak for a given material.

TABLE 3.2: Characteristic Temperature of Each CNT and CNT Composition in PDDA/(CNT+DOC) Assemblies

LbL System	T _{C_CNT} (°C)	W _{C_CNT} (%)	W _{C_LbL/CNT} (%)	CNT (%)
PDDA/(MWNT+DOC)	795	73.7	14.5	19.7
PDDA/(FWNT+DOC)	725	80.3	14.8	18.4
PDDA/(SWNT+DOC)	620	63.5	7.8	12.3

characteristic peak, which is only the result of nanotubes and catalyst. Therefore, the CNT concentration (expressed in wt%) in a given assembly is calculated by taking the characteristic peak wt% from TGA of the assembly, multiplying by 100, and finally dividing by the characteristic peak wt% from TGA of the neat nanotube. For example, the SWNT-based LbL assembly contains 12.3 wt% nanotube (plus some catalyst impurity), which was obtained by dividing 780 by 63.5. It is noteworthy that the [PDDA/(SWNT+DOC)]₂₀ film density is larger than PDDA or SWNT individually, but very close to their sum ($\rho_{\text{SWNT}} \approx 1.3 \text{ g/cm}^3$ and $\rho_{\text{PDDA}} \approx 1.1 \text{ g/cm}^3$). Thin films do not necessarily have densities that match their bulk values, so this apparent discrepancy may result from a highly ordered structure in the assembly. When thickness is measured after every deposited layer, thickness increases after deposition of SWNT, while it decreases slightly after each PDDA layer. Mass, however, increases after deposition of PDDA (**Figure 3.2(b)**), which suggests PDDA is penetrating into the underlying CNT layer. Each freshly deposited PDDA layer likely attracts CNTs in deeper layers to make denser, thinner films.

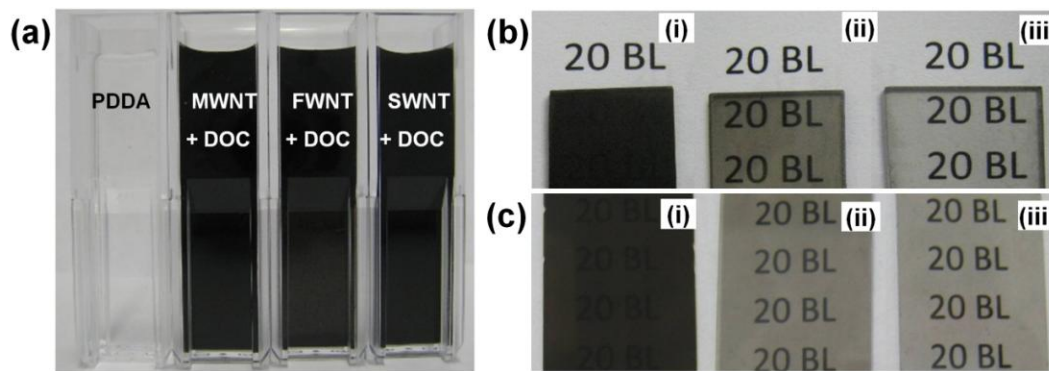


Figure 3.4. (a) Optical images of glass vials containing a 0.25 wt% PDDA aqueous solution and 0.05 wt% MWNT, FWNT, SWNT aqueous solutions stabilized by 2.0 wt% DOC. $[PDDA/(CNT+DOC)]_{20}$ coatings on both sides of (b) quartz and (c) PS substrates with (i) MWNT, (ii) FWNT, and (iii) SWNT.

Figure 3.4 shows vials of the aqueous deposition mixtures and three $[PDDA/(CNT+DOC)]_{20}$ thin films prepared on both sides of fused quartz slides and PS films. To the naked eye, all three solutions are too dark to see through after mild ultrasonication, but after depositing 20 bilayers on transparent substrates, only the MWNT coating is relatively opaque. In contrast, the SWNT coating is highly transparent and the FWNT is intermediate between MWNT and SWNT, as expected based upon tube diameter. The CNT coatings on PS are highly flexible thin films with no reduction of optical and electrical performance with repeated bending. The films shown in **Figure 3.4(c)** are $2\text{ cm} \times 5\text{ cm}$, but they could potentially be scaled up for large area, flexible electronics by replacing dipping with spraying.¹⁵

3.3.2 Structural Characterization

TEM micrographs of $[PDDA/(MWNT+DOC)]_{20}$ and $[PDDA/(SWNT+DOC)]_{20}$ cross-sections are shown in **Figure 3.5**. TEM is primarily used to visualize film structure, which in this case shows a highly inter-diffused nanostructure. In TEM cross-sections,

dark and light grey areas are CNT-rich and PDDA-rich regions, respectively, and the darkest black spots in the SWNT system are catalyst impurities from high-pressure CO conversion (HiPCO) process. Although not the goal of these images, they verify the 104 nm thickness of a $[\text{PDDA}/(\text{MWNT}+\text{DOC})]_{20}$ film measured by ellipsometry and the 12 nm diameter of an individual MWNT stated by the manufacturer. In the PDDA/(MWNT+

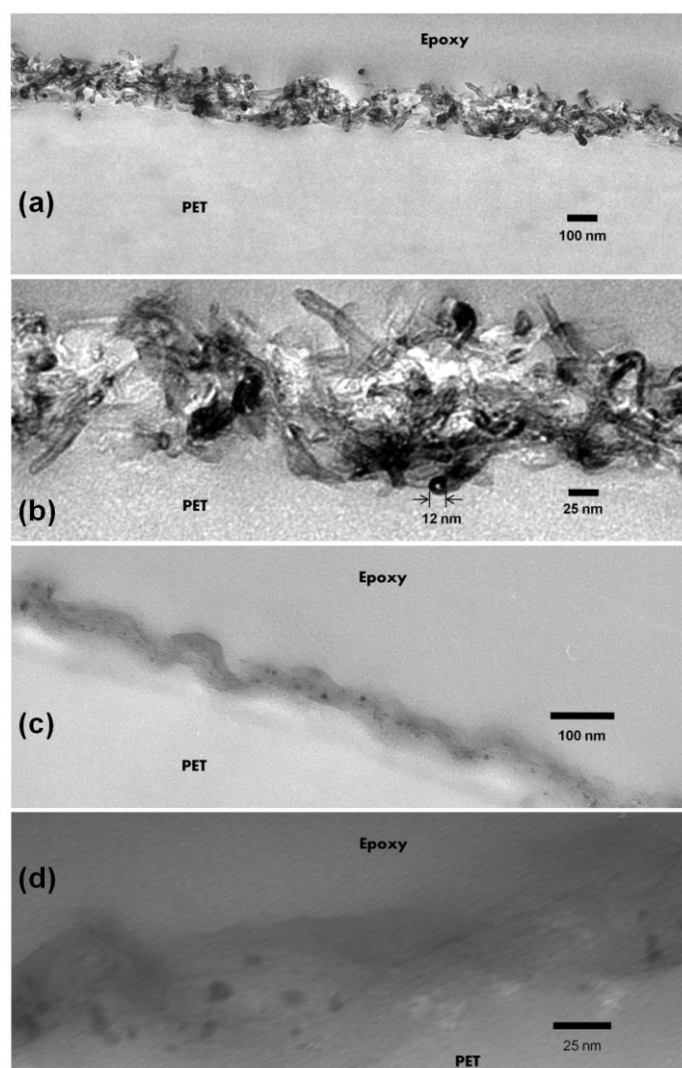


Figure 3.5. TEM cross-sections of a $[\text{PDDA}/(\text{MWNT}+\text{DOC})]_{20}$ thin film at (a) low and (b) high magnifications. Cross-sections of a $[\text{PDDA}/(\text{SWNT}+\text{DOC})]_{20}$ thin film are also shown at the same (c) low and (d) high magnifications.

DOC) system, several white regions are observed, indicating a looser, nano-porous structure due to inefficient packing of the thicker nanotubes. These open nano-structures account for the lower film densities that were measured using QCM in Section 3.3.1. This nanoporous structure of the MWNT thin film is further confirmed in the SEM and TEM surface images in **Figures 3.6** and **3.7**. Additionally, MWNTs are interwoven between each other in the matrix, resulting in a three-dimensional network. As a result, many electrical connections between layers give the film high conductivity even with only 2 BLs.

Figure 3.6 shows TEM surface images of 2 BL assemblies containing each of the three types of nanotubes. The surfaces of these CNT-based assemblies were also analyzed using SEM, as shown in **Figure 3.7**. In all cases, a homogeneous network of CNTs is observed. Addition of DOC for the exfoliation of individual CNTs aids the uniform distribution in the matrix that ultimately forms a three-dimensional network due to their polymer-like entanglements. CNT contacts within this network offer the pathway for electron transport through the film. The outer diameters of MWNTs used here are less than 13 nm, but the average thickness of each BL in a [PDDA/(MWNT+DOC)]₂₀ thin film is 4.9 nm. In the beginning of the LbL process, MWNTs are randomly deposited in the first layer. Next, gaps in the MWNT layer are filled with PDDA, but the polymer does not deposit thick enough to smooth out the surface. When the next MWNT layer is deposited, it is believed that the tubes populate the gaps left behind by the prior layer. In contrast, growth of a [PDDA/(SWNT+DOC)]₂₀ film proceeds at 1.85 nm per BL even though an individual SWNT has a diameter near 1 nm. This suggests SWNTs deposit more uniformly (*i.e.* fewer gaps in each layer) and may not be completely exfoliated.

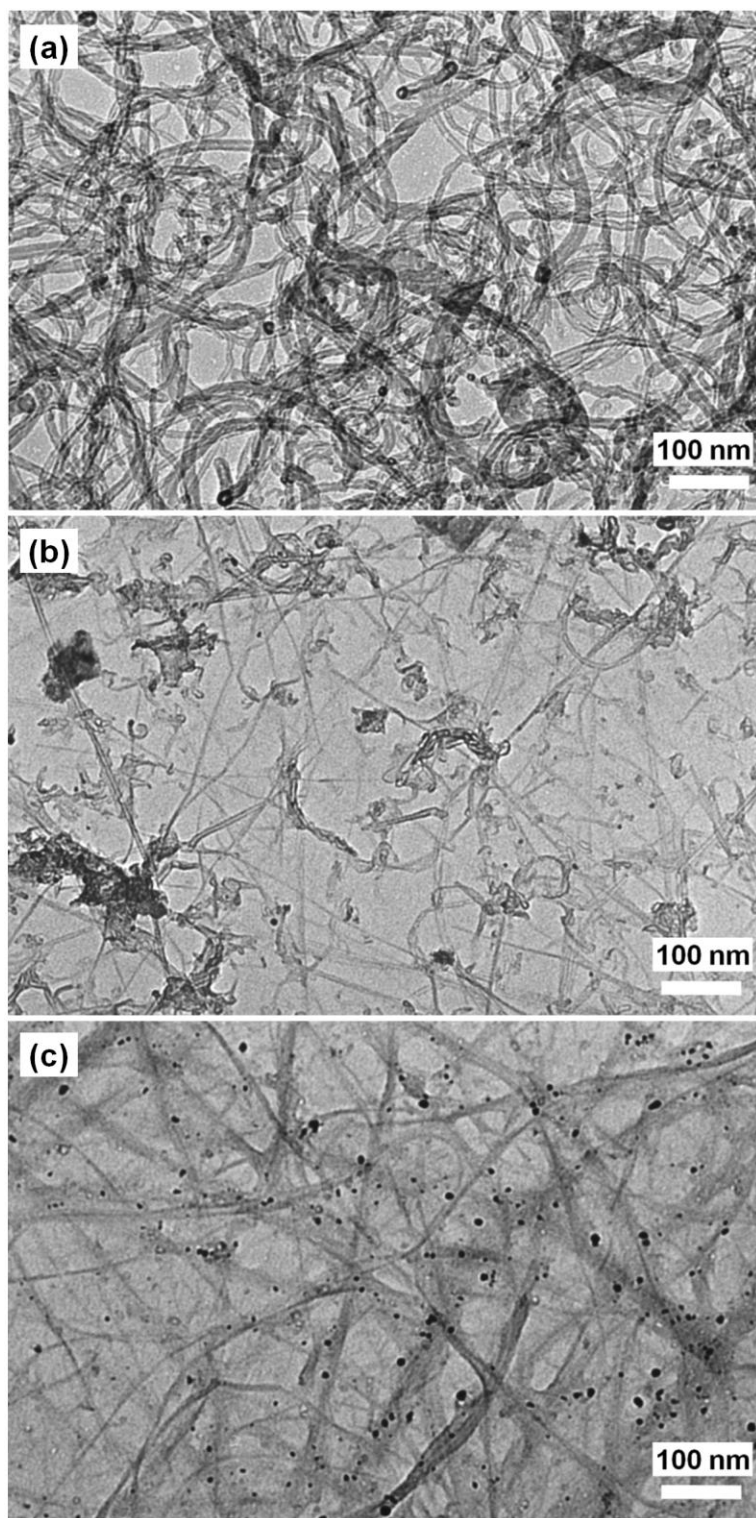


Figure 3.6. TEM surface images of (a) $[\text{PDDA}/(\text{MWNT}+\text{DOC})]_2$, (b) $[\text{PDDA}/(\text{FWNT}+\text{DOC})]_2$, and (c) $[\text{PDDA}/(\text{SWNT}+\text{DOC})]_2$ assemblies on Formvar grids.

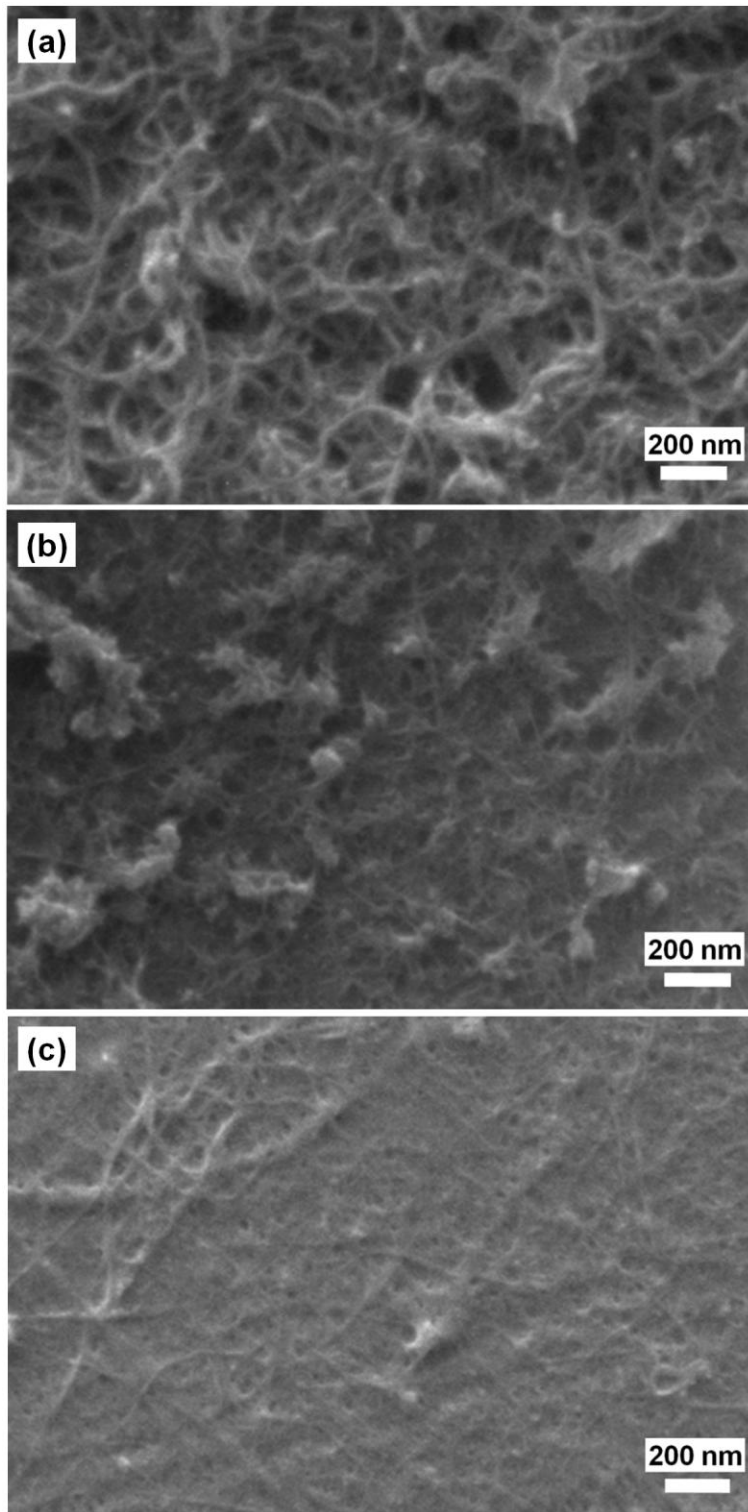


Figure 3.7. SEM surface images of (a) [PDDA/(MWNT+DOC)]₂₀, (b) [PDDA/(FWNT+DOC)]₂₀, and (c) [PDDA/(SWNT+DOC)]₂₀ assemblies on PS film.

These surface images further support the suggestion that PDDA infiltrates into, and adsorbs onto, each underlying CNT layer. TEM and SEM images provide complementary information because each reveals structural differences, having been deposited on formvar grids and PS film, respectively. In addition, SEM images (**Figure 3.7**) show that all of the 20 BL thin films deposit uniformly onto the substrates, but larger nanotubes give the PDDA/(MWNT+DOC) system a somewhat rougher surface than the other two systems. The 20 BL PDDA/(MWNT+DOC) films have a greater roughness than PDDA/(SWNT+DOC) due to larger nanotube size and complexity of the three-dimensional structure. **Figure 3.6(b)** clearly shows greater space between nanotubes and what appears to be reduced bundle size in the FWNT thin films, whereas **Figure 3.6(c)** reveals relatively heavy bundling in the SWNT thin film. The FWNT films have greater spacing between and less bundling amongst the nanotubes, thus they produce films with greater thickness (**Figure 3.1(b)**) despite depositing comparable mass relative to SWNT (**Figure 3.2(b)**), which results in lower film density than SWNT (see **Table 3.1**). Although the resolution is not as good, **Figure 3.7** reveals many of these same observations using SEM of 20 BL film surfaces. Some of the thicker spots in the middle of **Figure 3.7(b)** could be due to accumulation of PDDA after adsorption that obscures underlying CNT bundles.

3.3.3 Optoelectronic Behavior

Figure 3.8 shows the absorbance spectra of the three [PDDA/(CNT+DOC)]₂₀ films between 200 and 850 nm, as well as changes in absorbance at 550 nm as a function of the number of bilayers deposited. The concentration of CNTs in a given film is almost

constant, irrespective of the number of bilayers deposited, as shown in the QCM measurements (**Figure 3.3**). Therefore, the increasing absorbance of the PDDA/(CNT+DOC) systems with the number of bilayers deposited is due to increasing film thickness. The [PDDA/(SWNT+DOC)]₂₀ film has over 85% transmittance across the entire visible light spectrum. Transmittance is over 97% with only two bilayers. As expected, transparency of these CNT assemblies decreases as the tube diameter increases. The PDDA/(FWNT+DOC) system has 69 and 95% transmittance (at 550 nm) with 2 and 20 bilayers, respectively. The 20 BL MWNT-based coating has only 30% transmittance, but this increases to 90% with two bilayers.

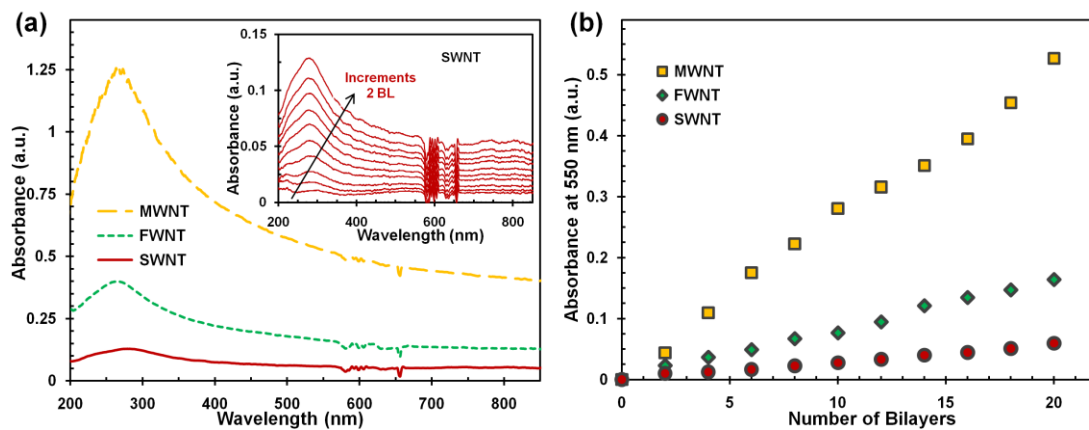


Figure 3.8. (a) Absorbance of PDDA/(CNT+DOC) assemblies on quartz slides from 200 to 850 nm. The inset is absorbance spectra of a PDDA/(SWNT+DOC) measured in 2 BL step up to 20 BLs. (b) Absorbance of the same thin films at 550 nm, as a function of the number of BLs deposited, is also shown.

Sheet resistance of these thin films was measured with a four-point probe system.

Figure 3.9(a) shows decreasing sheet resistance of [PDDA/(CNT+DOC)]_n ($n = 2-20$) thin films as a function of the number of bilayers deposited. Thicker films have a more

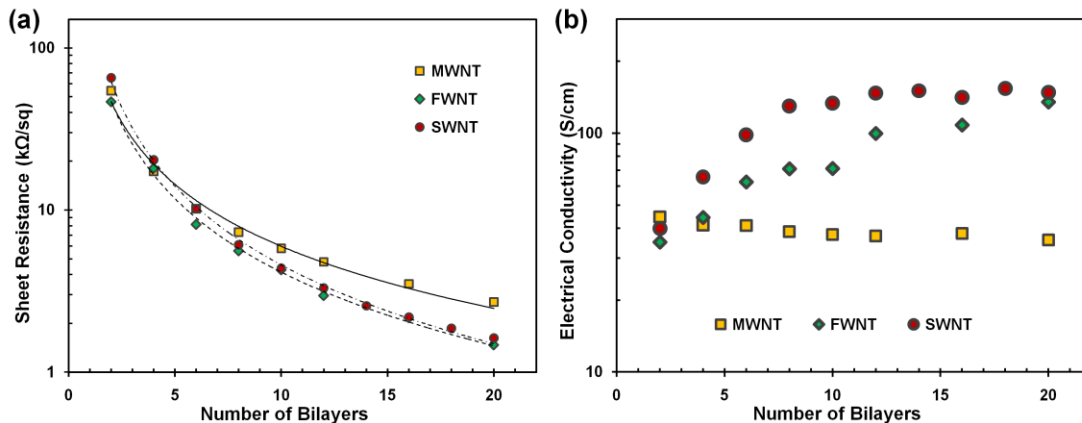


Figure 3.9. (a) Sheet resistance of $[\text{PDDA}/(\text{CNT}+\text{DOC})]_n$ thin films as a function of the number of bilayers deposited on PS film. (b) Electrical conductivity of the same systems as a function of the number of bilayers deposited, using the data in (a) multiplied by ellipsometric film thickness (**Figure 3.1**).

continuous three-dimensional CNT network that provides more efficient electron transport. Electrical conductivity of these films (**Figure 3.9(b)**) was obtained by taking the inverse of the product of the sheet resistance in **Figure 3.9(a)** and ellipsometric film thickness from **Figure 3.1(a)**. $[\text{PDDA}/(\text{SWNT}+\text{DOC})]_{20}$ thin films achieve conductivity as high as 148 S/cm (41.6 nm thick with a sheet resistance of 1.62 kΩ/sq) and 40 S/cm with just two BLs. $[\text{PDDA}/(\text{MWNT}+\text{DOC})]_n$ thin films have conductivity of 36 ($n = 20$) and 44 ($n = 2$) S/cm. With greater numbers of layers, the intrinsic nanotube conductivity becomes more important and this causes SWNT-based assemblies to exhibit significantly greater electrical conductivity. Although these conductivities are lower than some SWNT films made by vacuum filtration (6700 S/cm),²⁸ transfer printing (750–2000 S/cm),³⁶ direct CVD (2026 S/cm),⁴⁰ and spraying (5500 S/cm),⁴¹ they are high relative to vertically oriented SWNT electrodes (115 S/cm),¹⁴⁴ SWNT/polymer composites (2 S/cm),⁴⁴ and other LbL thin films with anionic polymer-wrapped SWNTs and polycations

(50 S/cm with 87% transmittance)⁶⁰ and anionic and cationic functionalized MWNTs after H₂ heat treatment (10 S/cm).⁶³ It is likely that heat treatment would further improve the conductivity of the present assemblies.^{60,61}

Polymer composites containing CNTs become electrical conductive when the CNT concentration is above the percolation threshold, which is the critical concentration necessary to form an electrical network with connection amongst conductive particles throughout the polymer matrix (causing the material to convert from an insulator to a conductor).¹⁴⁵ Beyond the percolation threshold, a gradual increase of electrical conductivity has been reported in polymer/SWNT LbL thin films,^{60,63} as well as in bulk SWNT-polymer composites,^{146,147} due to an increase of electron transport when the density of continuous intersecting pathways in the matrix are increased. In the SWNT thin film, the conductivity gradually increases from 40 to 150 S/cm as the number of bilayers increases to 20, but not dramatically like above and below percolation. This suggests that the PDDA/(SWNT+DOC) system has a CNT concentration over the percolation threshold and the density of intersecting pathways increases as the network transitions from two to three-dimensional. In contrast to the SWNT thin films, the MWNT films have constant conductivity, but essentially decrease from 44 to 36 S/cm. This slightly reduced conductivity with more layers may be due to weakened bonding amongst these relatively large nanotubes and increased porosity. These differences of two systems in conductivity, the gradual increase versus the steady state, can be explained by the nanostructure of two systems (**Figures 3.5–3.7**). SWNTs are largely deposited parallel to the substrate and generate a more two-dimensional structure, especially at low bilayer numbers. As more layers are deposited, the density of intersecting pathways can

increase due to interconnection between SWNTs in upper and lower layers. In the MWNT films, relatively homogeneous three-dimensional networks are formed from the beginning, due to greater rigidity (from larger radius) that would not allow the tubes to fully lay down on the substrate. This produces a highly interconnected three-dimensional network with just two bilayers.

Figure 3.10 compares the performance of the PDDA/(CNT+DOC) films studied here with other transparent SWNT films, by highlighting transparency as a function of sheet resistance. [PDDA/(SWNT+DOC)]₂₀ thin films have better transparency and lower sheet resistance (87% transmittance and 1.62 k Ω /sq) than spin-coated SWNT/polymer composites,⁴⁴ spin-coated Boron-doped SWNT,³⁸ electrophoretically deposited SWNTs,⁴³ sprayed SWNTs,²⁷ and vacuum filtered SWNTs.^{32,33} Additionally, these PDDA/(SWNT+DOC) films exhibit the lowest sheet resistance of any LbL assembly recipe in the absence of thermal annealing.^{58,60-63} This is believed to be due to the relatively mild dispersion conditions used (*i.e.*, 20 min of sonication in aqueous deoxycholate solution), which results in stable dispersion with relatively little damage to the nanotubes. Most LbL recipes use a polymer stabilizer and/or hours (or even days) of sonication⁶⁰ and/or oxidation treatment, usually with strong acid,^{58,59,61,63} to achieve sufficient dispersion. Long sonication time and oxidative treatments is known to shorten nanotube length and damage the conjugated sidewalls,¹⁴⁸⁻¹⁵² both of which result in reduced composite electrical conductivity. Additionally, the relatively large size of the polymer molecules likely creates an insulating barrier between neighboring tubes that further increases resistance. The dispersion/exfoliation of nanotubes with DOC requires

no oxidation step and it is assumed the small molecule size allows for more intimate contact between neighboring tubes.

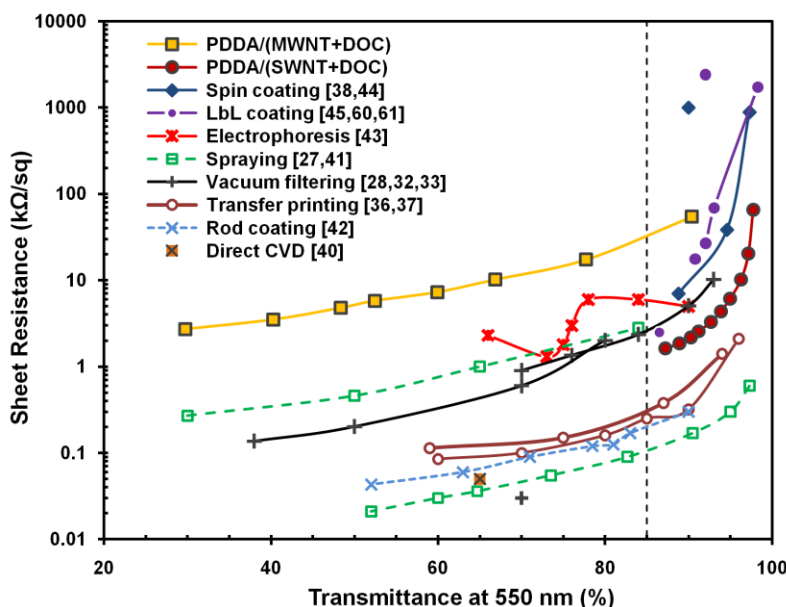


Figure 3.10. Comparison of the optoelectronic performance of $[PDDA/(CNT+DOC)]_n$ thin films with other transparent and conductive SWNT thin films.

Some other SWNT thin films exhibit better performance using transfer printing^{36,37} and rod coating,⁴² but these films are susceptible to breakage when transferred to a substrate.⁴⁵ Although not the focus of the present study, the $[PDDA/(SWNT+DOC)]_{20}$ film was annealed at 300 °C for five minutes, which resulted in a sheet resistance of 0.7 kΩ/sq and 85% transparency. This combination of low resistance and high transparency is the best ever reported for an LbL-produced carbon nanotube thin film and is competitive with the best films produced using any other technique. The required sheet resistance is 0.1 kΩ/sq for electromagnetic interference (EMI) shielding, 0.1 to 1 kΩ/sq for displays, and around 1000 kΩ/sq for electrostatic

dissipation (ESD) (combined with 85% visible light transmittance for transparent applications).²⁷ Therefore, the CNT assemblies studied here are potential candidates for ESD and possibly some flexible display applications.

3.4 Conclusions

Highly transparent and electrically conductive thin films were assembled layer-by-layer using CNTs stabilized with negatively-charged deoxycholate and positively-charged PDDA. Alternate substrate exposure to PDDA and CNT-DOC aqueous mixtures generated thin films that grow in a linear fashion as a function of bilayers deposited, as demonstrated with visible light absorbance, ellipsometry, and QCM (*i.e.*, mass). Optical and electrical performance of these CNT-based assemblies showed that SWNTs produced thinner and smoother films, with higher transparency and electrical conductivity, than comparable MWNT-based films. Even after 20-bilayers of deposition, these films are only 41.6 nm thick and contain approximately 12 wt% SWNT. Multi-walled nanotubes achieved low sheet resistance ($< 100 \text{ k}\Omega/\text{sq}$) with fewer bilayers, but the films are more opaque and have lower electrical conductivity relative to SWNT-based assemblies beyond two bilayers. The larger, stiffer MWNTs generate thicker assemblies and produce a stronger three-dimensional network that accounts for these differences. The conductivity of $[\text{PDDA}/(\text{SWNT}+\text{DOC})]_{20}$ is higher than most other SWNT-polymer composites, at 148 S/cm ($R_s = 1.62 \text{ k}\Omega/\text{sq}$) with greater than 85% visible light transmittance. These nanotube-based thin films are among the most conductive and transparent currently reported in the literature, especially after annealing at 300°C , which generates SWNT-based films with sheet resistance below $1 \text{ k}\Omega/\text{sq}$ and visible light

transmittance above 85%. Additionally, LbL assembly is a simple and convenient process relative to most competitive techniques. This study lays the groundwork for future studies to improve optoelectronic performance of transparent conductive thin film assemblies, which is likely to include the removal of PDDA following deposition (with heat or solvent). Even in their present state, these films could be useful for a variety of flexible electronics applications.

CHAPTER IV

HEATING CARBON NANOTUBE ASSEMBLIES FOR REDUCED SHEET RESISTANCE[‡]

4.1 Introduction

In Chapter III, LbL assembly was used to generate transparent, highly conductive thin films, less than 100 nm thick, containing carbon nanotubes. Three different types of nanotubes were used to evaluate their influence on transparency and conductivity.¹¹⁵ SWNTs produced the most transparent (>85% visible light transmittance) and electrically conductive (~ 1.62 k Ω /sq) 20-bilayer films, with a 41.6 nm thickness. Unfortunately, a sheet resistance of 0.1 k Ω /sq is required for EMI shielding and many flexible electrodes (combined with 85% T for transparent applications).²⁷ This means a greater reduction in sheet resistance is needed to make these transparent CNT-based LbL films suitable for these applications. Heating these films, to remove some insulating polymer, is one method to reduce sheet resistance.¹⁵³

In this chapter, transparent electrodes were assembled using layer-by-layer assembly with PDDA as the polycation and DOC-stabilized SWNT as the negatively charged layers (same system as Chapter III). Even though LbL assembly was previously used to produce a variety of SWNT-based assemblies,^{60,61,115,137} the films described here show enhanced transparency and electrical conductivity through heat treatment, resulting in the best combination of properties ever reported for LbL thin films (% T = 82.3% and

[‡] Reprinted with permission from “Heating and acid doping thin film carbon nanotube assemblies for high transparency and low sheet resistance” by Yong Tae Park, Aaron Y. Ham, and Jaime C. Grunlan, *J. Mater. Chem.* **2011**, *21*, 363-368. ©2010 Royal Society of Chemistry.

$R_S = 701 \text{ } \Omega/\text{sq}$ for a 20 BL film with a thickness of 38.4 nm). Ellipsometry, quartz crystal microbalance, and UV-vis were used to measure the linear growth of these films as a function of the number of BLs deposited, while TEM and SEM were used to visualize the morphology of these films. Films with a small number of BLs are potentially useful for anti-static films, while adding more BLs produces transparent, flexible electrodes that could potentially act as an ITO alternative.

4.2 Experimental

4.2.1 Materials

All materials used here are identical to those described in Chapter III (see Section 3.2.1).

4.2.2 Layer-by-Layer Assembly and Heat Treatment

The LbL assembly procedure was the same as that described in Chapter III (see Section 3.2.2). Following deposition and drying, heat treatment was performed at 300, 350 and 400 °C in a furnace purged with nitrogen gas, followed by drying overnight in a dry box.

4.2.3 Thin Film Characterization and Microscopic Imaging

The film characterization and microscopic imaging procedure were the same as that described in Chapter III (see Sections 3.2.3–3.2.5).

4.3 Results and Discussion

4.3.1 Influence of Deoxycholate on Carbon Nanotube Assemblies

In practical applications of CNTs, their low solubility in solvents prevents high quality and wide versatility in the various fields. Especially, in the LbL process, the availability of use of CNTs depends on the ability to yield high quality dispersions with individual CNTs and a minimum of CNT bundles. To introduce CNTs into LbL assembly, the synthetic anionic surfactant, deoxycholate (DOC), was used to create negatively charged solution. DOC, one of the best surfactant for dispersion of individual nanotube,^{138,139} has a charged polar tail which prevents aggregation of CNTs to provide a solvation shell and by the repulsive Coulomb force between DOC-attached CNTs. Examples of the DOC-stabilized CNT solutions used for LbL assembly are shown in **Figure 4.1**. After 2 months from sonication, these solutions remained well dispersed and LbL films with these solutions had the same properties as those with as-sonicated CNT solutions, suggesting that DOC accomplished stable dispersion of nanotubes.

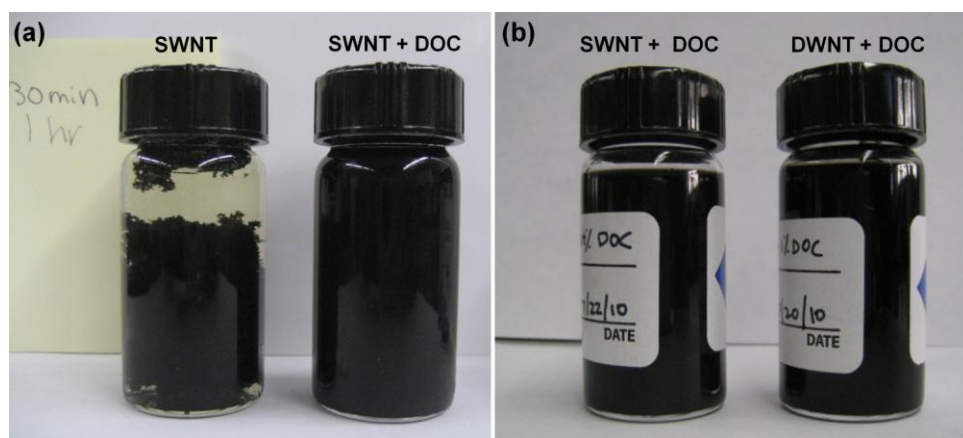


Figure 4.1. (a) Photograph of 0.05 wt% SWNT only solution and (0.05 wt% SWNT+1 wt% DOC) solution after 1 hour from sonication. (b) Photograph of (0.05 wt% SWNT+1 wt% DOC) and (0.05 wt% DWNT+1 wt% DOC) solutions after 2 months from sonication.

In an effort to optimize DOC concentration, four types of aqueous 0.05 wt% SWNT suspensions with (a) 0.5, (b) 1, (c) 2, and (d) 4 wt% DOC, were prepared. [PDDA/(SWNT+DOC)]₂₀ films were prepared with each suspension for comparison with a 0.05 wt% PDDA solution as the positively charged component. **Figure 4.2** shows the normalized properties of ellipsometric thickness, UV-vis absorbance, and electrical conductivity, based on values of SWNT assemblies prepared with the 1.0 wt% DOC solution, which had the highest of all three values amongst the four DOC concentrations. The 2 wt% DOC film exhibited less than 2% difference in thickness and absorbance, and 10% in electrical conductivity from the 1 wt% DOC film. On the other hand, the conductivity of other two samples was approximately half that of the 1 wt% DOC film. In the case of 0.5 wt% DOC, thickness and absorbance are also very low compared to 1 wt% DOC films, which suggests that a lack of DOC harms SWNT dispersion in solution and results in poor deposition of SWNT layers. Although the 4 wt% DOC film shows similar thickness and absorbance data to 2 wt%, conductivity is much lower, suggesting that an excessive amount of DOC interferes with SWNT connections. Additionally, for the thin films with the same material and composition, the absorbance is linearly proportional to their thickness (from the Beer–Lambert law).¹⁵⁴ This means that the similar level of thickness and absorbance in the 1 and 2 wt% DOC films indicates that they have a similar composition with regard to PDDA and DOC-stabilized SWNT. In contrast, the 0.5 wt% DOC film has a much lower level of absorbance than thickness, indicating a lower concentration of the light absorbing material (*i.e.*, SWNT). Based on these results, 0.25 wt% PDDA/(0.05 wt% SWNT+1 wt% DOC) has chosen as the recipe for further study.

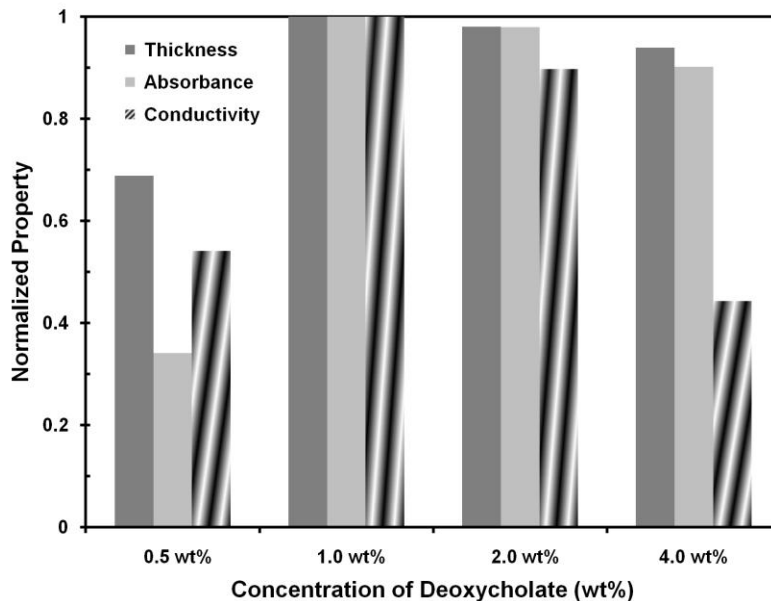


Figure 4.2. Comparison of the ellipsometric 20BL thickness, UV-vis absorbance at 550 nm, and electrical conductivity of four different films. These $[\text{PDDA}/(\text{SWNT}+\text{DOC})]_{20}$ films were fabricated with four different concentrations of DOC.

4.3.2 Growth of SWNT Assemblies

Figure 4.3(a) shows an image of a series of SWNT-based assemblies deposited on both sides of PS film, denoted as $[\text{PDDA}/(\text{SWNT}+\text{DOC})]_n$, where n is the number of bilayers deposited. The film in **Figure 4.3(b)** is a $7.5 \text{ cm} \times 7.5 \text{ cm}$ piece of PS coated with a $[\text{PDDA}/(\text{SWNT}+\text{DOC})]_{20}$ (*i.e.*, 20 BL) film that is 40 nm thick. This relatively large film demonstrates the potential for scale-up, because film size is limited only by the substrate dimension. Furthermore, this $[\text{PDDA}/(\text{SWNT}+\text{DOC})]_{20}$ film exhibits 82% transmittance at 550 nm and over 80% across the entire visible light spectrum as shown in **Figure 4.4**. A TEM micrograph of this film's cross-section, which illustrates a highly inter-diffused nanostructure, is shown in **Figure 4.3(c)**. The uniform distribution of SWNTs in the matrix is due to the effectiveness of DOC as a stabilizer for SWNTs.^{138,139}

In addition to highlighting thin film structure, the TEM image verifies the 38.4 nm thickness of a $[\text{PDDA}/(\text{SWNT}+\text{DOC})]_{20}$ film, measured independently by ellipsometry.

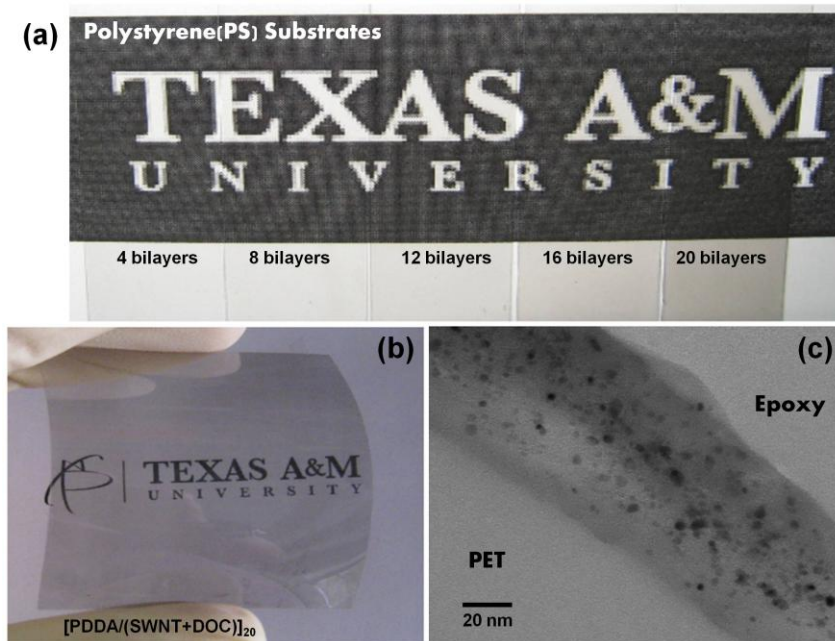


Figure 4.3. (a) Photograph of $[\text{PDDA}/(\text{SWNT}+\text{DOC})]_n$ ($n = 4\text{--}20$) assemblies on both sides of PS film. (b) Optical image of a $[\text{PDDA}/(\text{SWNT}+\text{DOC})]_{20}$ coating on both sides of the 7.5×7.5 cm PS film. (c) TEM cross-section of a $[\text{PDDA}/(\text{SWNT} + \text{DOC})]_{20}$ thin film.

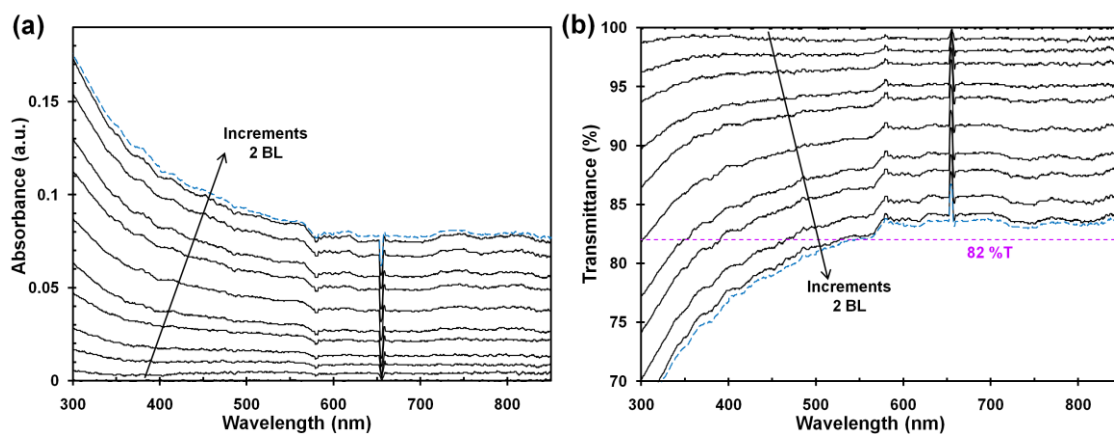


Figure 4.4. (a) Absorbance and (b) transmittance spectra of $[\text{PDDA}/(\text{SWNT}+\text{DOC})]_n$ thin films, measured in 2 BL step up to 20 BLs. The dotted line is of $[\text{PDDA}/(\text{SWNT}+\text{DOC})]_{20}$ after 300°C heating for 5 min.

Surfaces of these SWNT-based assemblies were analyzed using SEM, as shown in **Figure 4.5**. The $[\text{PDDA}/(\text{SWNT}+\text{DOC})]_{20}$ surface shows a homogeneous network of SWNTs in **Figure 4.5(a)**. DOC exfoliation of individual SWNTs in water ultimately forms a uniform distribution in the thin film. SWNT contacts within this network offer a pathway for electron transport through the film, as shown in these SEM images (as well as in the TEM image in **Figure 4.3(c)**). Growth of this film proceeds at 1.9 nm per BL, which suggests very uniform deposition of highly individualized SWNTs.

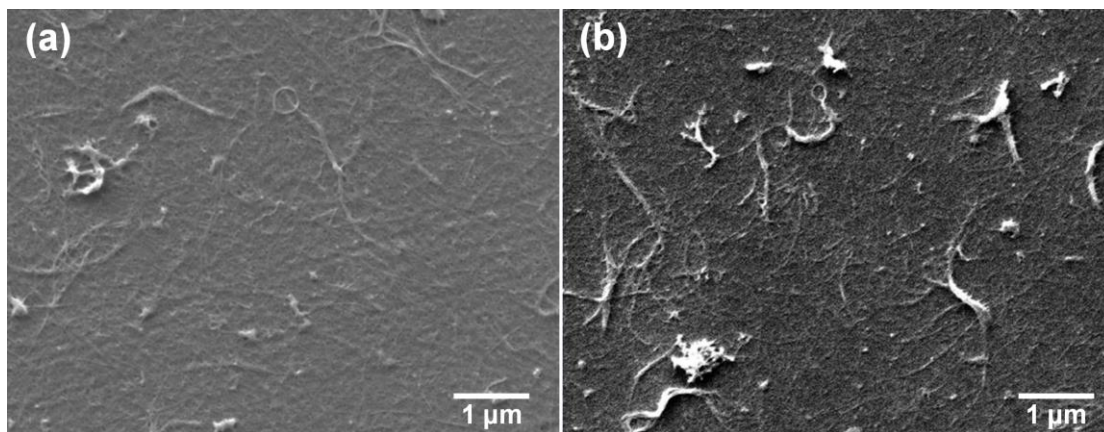


Figure 4.5. SEM surface images of $[\text{PDDA}/(\text{SWNT}+\text{DOC})]_{20}$ (on a silicon wafer) (a) before heat treatment and (b) after heating at 300 °C for 10 min.

Linear growth of these nanotube-based thin films up to 20 BLs was observed using several complementary techniques (ellipsometry for thickness, QCM for mass, and UV-vis for absorbance), as shown in **Figure 4.6(a)**. The constant concentration of SWNTs in every bilayer, determined with QCM, supports the assumption that the increasing absorbance of $[\text{PDDA}/(\text{SWNT}+\text{DOC})]_n$ is due to increasing film thickness.

Linear growth also confirms successful combination of positively and negatively charged components and constant composition up to 20 BLs. In **Figure 4.6(b)**, however, steadily increasing mass appears in contrast to slightly decreasing thickness with each polycation deposition (at half BLs). The believed mechanism for this behavior involves each PDDA layer's penetration into the SWNT layers below, resulting in denser and thinner films due to strong electrostatic interactions amongst the oppositely charged layers. TGA and QCM were performed on the PDDA/(SWNT+DOC) system, which indicates a SWNT concentration of 12.3 wt% and density of 2.04 g/cm^3 in the 20 BL film ($7.81 \text{ } \mu\text{g/cm}^2$ mass and 38.4 nm thickness). This density is larger than PDDA or SWNT individually ($\rho_{\text{SWNT}} \approx 1.3 \text{ g/cm}^3$ and $\rho_{\text{PDDA}} \approx 1.1 \text{ g/cm}^3$), which is believed to be the result of a highly ordered structure with extensive interpenetration between the deposited layers.

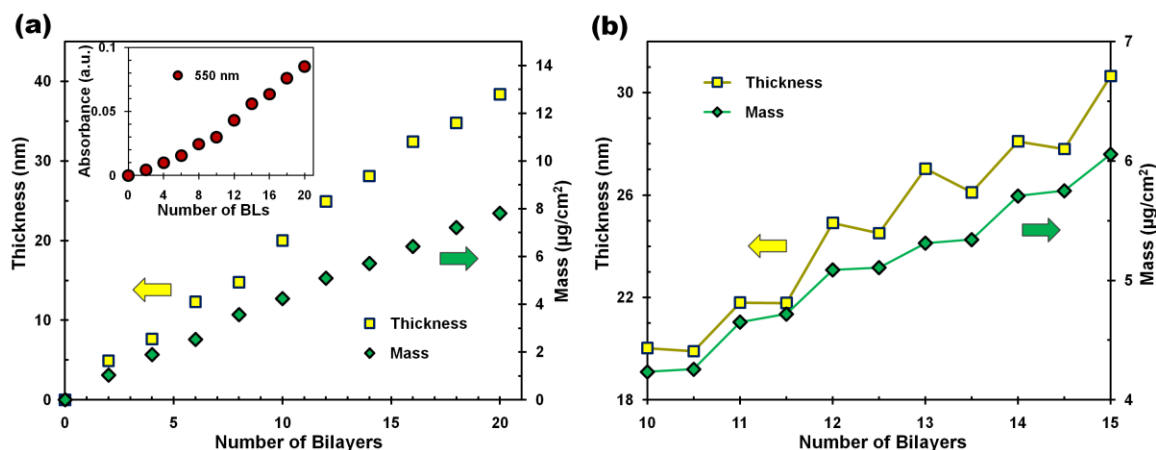


Figure 4.6. (a) Growth of PDDA/(SWNT+DOC) thin films as a function of the number of bilayers deposited. Film thickness was obtained by ellipsometry, mass by QCM, and absorbance (at 550 nm) by UV-vis (inset), respectively. (b) Thickness and mass change from 10 to 15 BLs, where a half bilayer corresponds to PDDA deposition.

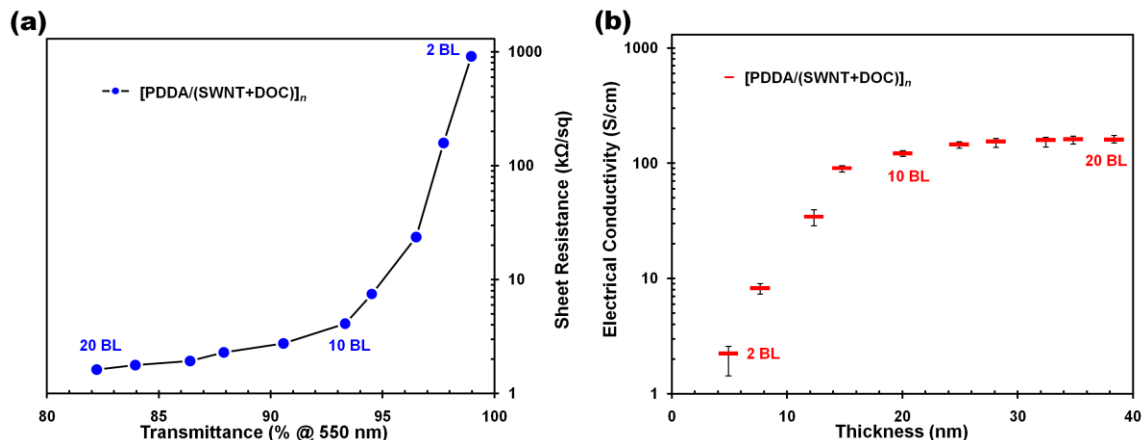


Figure 4.7. (a) Optoelectronic performance and (b) electrical conductivity of $[\text{PDDA}/(\text{SWNT}+\text{DOC})]_n$ thin films as a function of the number of bilayers deposited to 20 BL are also shown.

Sheet resistance of these thin films was measured with a four-point probe system.

Figure 4.7(a) shows the optoelectronic characteristics of $[\text{PDDA}/(\text{SWNT}+\text{DOC})]_n$ ($n = 2-20$) as a function of the number of BLs deposited. Decreasing sheet resistance and transmittance are observed as the number of BLs increases. Electrical conductivity of these films (**Figure 4.7(b)**) was calculated as the inverse of the product of sheet resistance and ellipsometric film thickness. $[\text{PDDA}/(\text{SWNT}+\text{DOC})]_{20}$ thin films on glass slides achieve a conductivity as high as 160 S/cm (38.4 nm thick with a sheet resistance of 1.62 kΩ/sq) and exhibit 2.2 S/cm (4.9 nm thick with a sheet resistance of 912 kΩ/sq) with only two BLs. This relatively high conductivity is aided by thin PDDA deposition and relatively mild dispersion conditions used for the nanotubes. Long sonication time, for hours or even days, is known to shorten nanotube length and damage the conjugated sidewalls,¹⁴⁹ resulting in reduced electrical conductivity. The gradual increase from 2 to

160 S/cm suggests that the PDDA/(SWNT+DOC) system has a SWNT concentration over the percolation threshold and the density of intersecting pathways increases as the network transitions from two to three-dimensional. As more layers are deposited, the density of intersecting pathways increases due to interconnection between SWNTs in upper and lower layers. Despite this relatively low sheet resistance ($< 2 \text{ k}\Omega/\text{sq}$ at 20 BL), a reasonable ITO replacement requires even lower values ($< 1 \text{ k}\Omega/\text{sq}$).

4.3.3 Electrical Properties after Heat Treatment

Although PDDA and DOC produce uniform dispersion and deposition of SWNTs, they also create insulating connections. Furthermore, the relatively large size of the polymer molecules likely creates an insulating barrier between nanotubes in neighboring layers that further increases resistance. Heating these films to degrade the amount of insulating material is one method to further increase electrical conductivity. PDDA has a lower degradation temperature ($300 \text{ }^\circ\text{C}$) than DOC ($> 450 \text{ }^\circ\text{C}$) and SWNT ($> 500 \text{ }^\circ\text{C}$), as determined by TGA (in **Figure 4.8**). Heating thin film assemblies between 300 and $400 \text{ }^\circ\text{C}$, under a nitrogen atmosphere, can exclusively target decomposition of PDDA. With the polymer significantly degraded, more intimate contact between neighboring tubes is possible. **Figure 4.5(b)** shows more exposed individual SWNTs on the [PDDA/(SWNT+DOC)]₂₀ surface due to PDDA decomposition by heating, compared with **Figure 4.5(a)**.

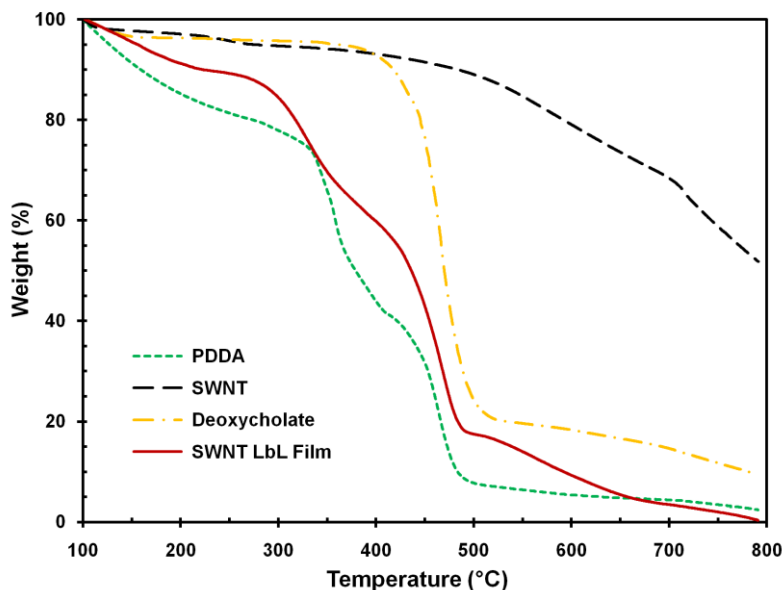


Figure 4.8. Thermogravimetry of the components of the PDDA/(SWNT+DOC) system and a fully assembled film under a nitrogen atmosphere.

Figures 4.9(a) and (b) show the sheet resistance and electrical conductivity, respectively, after heating at various temperatures for increasing time periods. The sheet resistance of [PDDA/(SWNT+DOC)]₂₀ was most significantly reduced by heating for short times (≤ 5 min) and lower temperatures (< 350 °C). For 5 min at 300 °C, sheet resistance decreases more than 52% (to 701 Ω/sq). In the case of heating more than 10 min at 400 (or even 350 °C), however, it is believed that some modest damage of SWNTs causes the observed increase in sheet resistance. It is at 300 °C where the best compromise between removal of insulating barriers and minimal harm to nanotubes is achieved. It should also be noted that heat treatment can also reduce film thickness.

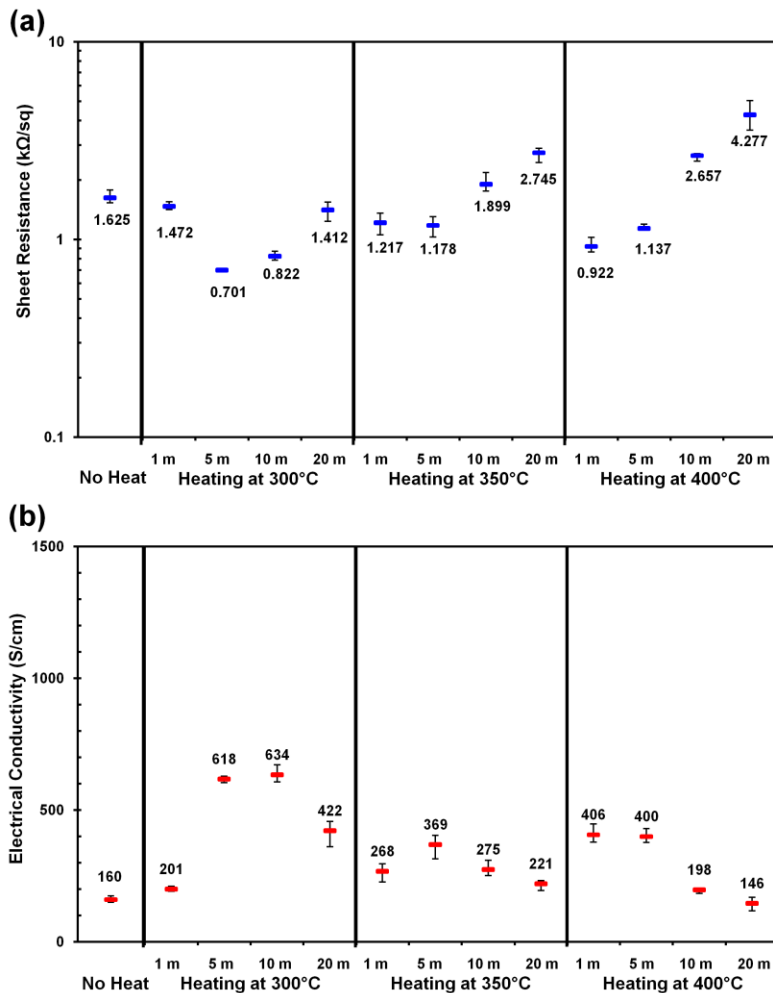


Figure 4.9. (a) Sheet resistance and (b) electrical conductivity of [PDDA/(SWNT+DOC)]₂₀ thin films after 300, 350, and 400 °C heating, for 1 to 20 min.

Heating at 300 °C for 10 min produced conductivity as high as 634 S/cm (19.2 nm thick with a sheet resistance of 822 Ω/sq) partly due to a 49% decrease in film thickness. **Figure 4.10** shows the normalized sheet resistance and thickness after heating. Sheet resistance generally decreases after heat treatment, but excessive heating causes an increase in resistance due to damage of the SWNT network. Heating at 300 °C for 5–10 min provides the lowest resistance, while 20 min heating results in the highest value. In

the cases of 350 and 400 °C, more than 10 min of heating made the sheet resistance higher than the original untreated value. As expected, thickness gradually decreases for all three heating temperatures, as a function of exposure time up to 20 min, down to some plateau at the value of 0.43. For 1 min heating, the decrease in film thickness is 12% at 300 °C and around 30% at 400 °C, but there is no difference in thickness among all three heating temperatures beyond 5 min (40%, 50%, and 57% for 5, 10, and 20 min heating, respectively), suggesting that PDDA can be effectively degraded within the first 10 minutes.

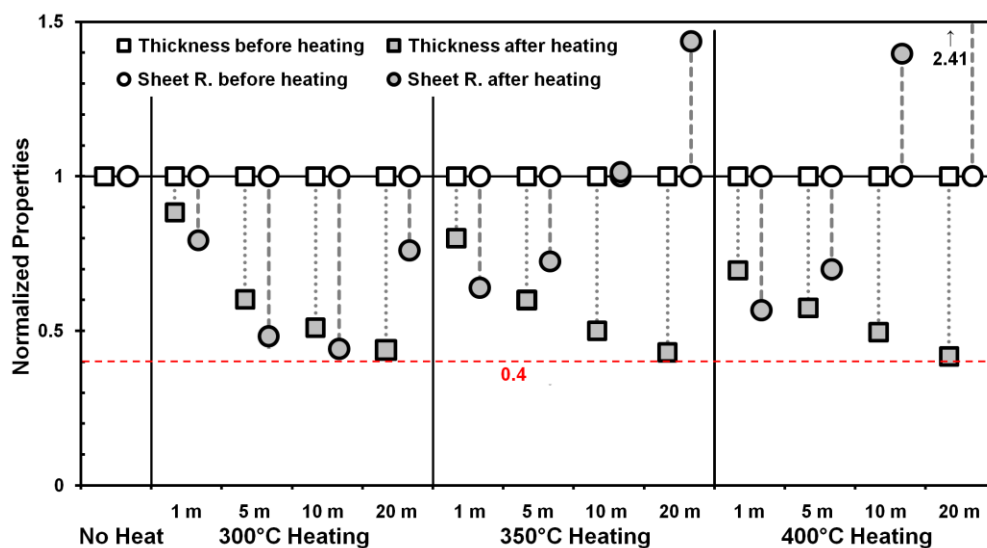


Figure 4.10. Normalized thickness and sheet resistance after heat treatment. White and grey colors mean before and after heating, respectively.

UV-vis absorption measurements show there is little change of transmittance regardless of heat treatment, as shown in **Figure 4.4**, which is presumably because the amount of nanotube remains constant. The transmittance after 300 °C heating for 5 min is

82.1% (at 550 nm) and averages over 80% (from 500 to 800 nm). This combination of low resistance and high transparency makes these post treated [PDDA/(SWNT+DOC)]₂₀ films are more conductive than any other LbL-produced SWNT thin films ever reported and are competitive with the best SWNT-based films produced using any other technique when accounting for transparency and flexibility. The sheet resistance and transmittance criteria for various optoelectronic applications suggest these SWNT assemblies are potential candidates for electrostatic dissipation and some flexible display applications.²⁷

4.4 Conclusions

Highly transparent and electrically conductive thin films were assembled using the layer-by-layer method. Alternate substrate exposure to aqueous mixtures of positively-charged PDDA and SWNTs stabilized with negatively-charged DOC produced thin films that grow in a linear fashion as a function of the number of bilayers deposited (evidenced by visible light absorbance, ellipsometric thickness, and mass). [PDDA/(SWNT+DOC)]₂₀ films have a 38.4 nm thickness, 160 S/cm conductivity ($R_s = 1.62 \text{ k}\Omega/\text{sq}$), 82% visible light transmittance, and contain 12 wt% SWNT. Post heating this film for 10 min at 300 °C resulted in a 54% lower resistance and raised the bulk conductivity by 4 times. These improvements are largely due to the removal of PDDA by heating to provide more intimate nanotube connections. With visible light transmittance >82% and sheet resistance of 701 Ω/sq , this SWNT-based thin film is a flexible transparent electrode capable of replacing ITO in some optoelectronic applications. Acid treatment further reduces sheet resistance of these films, as described in Chapter II.

CHAPTER V

ACID TREATMENT OF CARBON NANOTUBE ASSEMBLIES FOR REDUCED SHEET RESISTANCE

5.1 Introduction

In Chapter IV, SWNT-based assemblies were shown to exhibit low sheet resistance and high transparency through heat treatment (% T = 82.3% and $R_s = 701 \Omega/\text{sq}$ for a 20 BL film with a thickness of 38.4 nm).¹¹⁵ This low sheet resistance was partly due to the removal of insulating polymer, which provided more intimate nanotube connections. Unfortunately, heating beyond 300 °C is not practical for the polymer substrates typically used to produce flexible electronics. Exposing nanotube films to strong acid has been shown to enhance conductivity and this can be done at relatively low temperature. Although the mechanism of acid treatment for CNT-based assemblies is still uncertain, the increase in electrical conductivity has been attributed to acid anion doping^{155,156} and removal of surfactant.^{41,157} In the case of doping, strong acidic anions penetrate the thin carbon nanotube network, creating an acidic anion layer around individual nanotubes that act as a highly dense charge-transfer complex.¹⁵⁵ Other studies have reported large improvements in electrical conductivity of the CNT-based thin film with acid treatment due to removal of surfactant.⁴¹ This acid treatment can be done in the vapor phase at temperatures below 100 °C, making this more amenable to polymer films.

This chapter examines the influence of acid treatment on the optoelectronic performance of these nanotube-based thin films. For each film studied, optoelectronic behavior was characterized before and after acid treatment, using various acid types

(nitric, sulfuric, and hydrochloric acids) and time. The results are compared to other systems using sulfuric acid,^{41,42,137,155,156,158} nitric acid,^{32,42,156,158-160} and thionyl chloride doping.^{32,161} Replacing SWNT with double-walled carbon nanotubes (DWNT) provided further reduction in sheet resistance due to the greater metallic and longer average length of DWNT.^{162,163} A 5 BL assembly, containing double-walled carbon nanotubes (DWNTs), exhibits a significant reduction in sheet resistance, from 309 to 112 Ω/sq , after two minutes of exposure to HNO_3 vapor. This film is highly flexible and electrochemically stable, making it a potential alternative for ITO. Transparent electrodes made from metal oxides suffer from poor flexibility and durability.^{3,65} After 100 bending cycles, the CNT LbL films exhibit the same resistance, but the resistance of ITO-coated PET increases two orders of magnitude. In addition to mechanical stability, cyclic voltammetry was used to evaluate the electrochemical stability of these transparent electrodes. This combination of optoelectronic performance, mechanical flexibility, and electrochemical stability make this a suitable candidate for replacing ITO.

5.2 Experimental

5.2.1 Materials

As-produced CNTs have largely various properties due to different types of wall, diameters, lengths, chiralities, and impurities (amorphous carbon, metal catalyst, etc.) which depend on the manufactures. Selection of CNTs is the key factor for high performance of transparent conductive CNT thin films. One of CNTs used in this study is purified electric arc (EA) SWNTs (P2-SWNT, individual tube: average 0.5–3 μm length and 1.4 nm diameter, $\text{C} \geq 90 \text{ wt}\%$) synthesized using Ni/Y catalysts from Carbon

Solutions, Inc. (Riverside, CA). The other is high-pressure CO conversion (HiPCO) DWNTs (XB type, + 1 μm length and ~ 3.0 nm diameter, $C \geq 90$ wt%) purchased from Continental Carbon Nanotechnologies, Inc. (Houston, TX). Fuming sulfuric acid (oleum, $\text{H}_2\text{SO}_4 \cdot (\text{SO}_3)_x$, 20% free SO_3 basis), fuming nitric acid (HNO_3 , 99.5%), and fuming hydrochloric acid (HCl , 37%) were purchased from Sigma-Aldrich (Milwaukee, WI) for acid treatment. All chemicals were used as received. A 100 Ω/sq ITO-coated PET sheet was purchased from Sigma-Aldrich and cut to size to measure the optical transmittance and the change in sheet resistance during bending cycles. All other materials used here are identical to those described in Chapter III (see Section 3.2.1).

5.2.2 Layer-by-Layer Assembly and Acid Treatment

The LbL assembly procedure is described in detail in Chapter III (see Section 3.2.2). Assembled CNT films were held in a saturated acid vapor environment, as illustrated in **Figure 5.1**. Three types of acids (fuming sulfuric, nitric, and hydrochloric acids) in the petri dishes were maintained at 70 $^\circ\text{C}$ with a water bath (*caution*: dangerous oxidizing agents). After 2 to 30 min vapor treatment, the CNT films were rinsed with deionized water and dried with filtered air.

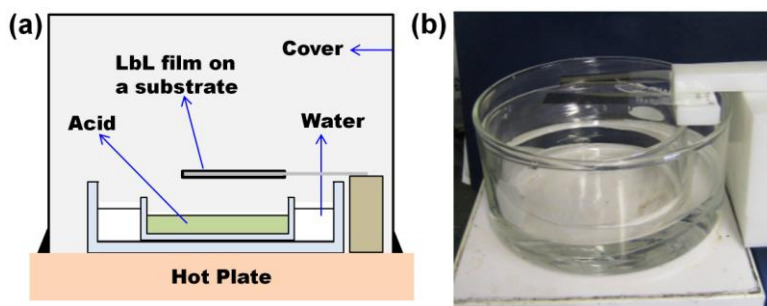


Figure 5.1. (a) Schematic of acid treatment apparatus and (b) picture of actual apparatus without cover.

5.2.3 Thin Film Characterization

Film characterization and microscopic imaging were the same as that described in Chapter III (see Sections 3.2.3–3.2.5). The Fourier-transform infrared (FT-IR) spectra were obtained from a ALPHA FTIR spectrometer (Bruker Optics, Billerica, MA). Energy dispersive X-ray (EDX) analysis was carried out using the Oxford EDX system associated with FE-SEM and equipped with X-ray mapping. An Epsilon 851 electrochemical workstation (BASi Instrumentation, West Lafayette, IN) was used for electrochemical characterization. A CNT- or ITO-coated PET electrode, a platinum wire, and an Ag/AgCl (3M KCl) electrode were used as the working, counter, and reference electrodes, respectively. These measurements were performed at ambient temperature (22 ± 2 °C) in 0.1 M Na₂SO₄ solution that had been purged with N₂ gas for more than 20 min prior to measurement. Cyclic voltammetry was performed between -0.2 and 0.8 V at a scan rate of 100 mV/s.

5.3 Results and Discussion

5.3.1 Growth and Microstructure of Carbon Nanotube Assemblies before and after Acid Treatment

Figure 5.2 shows the linear growth of this LbL assembly of cationic PDDA and anionic DOC-stabilized double-walled carbon nanotubes up to 10 BLs, denoted as [PDDA/(DWNT+DOC)]_{*n*}, where *n* is the number of bilayers deposited. Ellipsometric thickness was obtained by depositing these thin films on silicon wafers. The average thickness of one DWNT-containing bilayer is 4.4 nm, which is much thicker than an individual thickness of double-walled carbon nanotube (1.5–3 nm), suggesting that stabilizing surfactant (DOC) and PDDA fully enveloped the DWNT network deposited.

In agreement with film thickness, the graph of optical absorbance confirms that these CNT-based LbL assemblies grow linearly up to 10 BL. A [PDDA/(DWNT+DOC)]₅ film on PET is highly transparent, with 84.2% transmittance at 550 nm, which is comparable to ITO-coated PET (84.6% T at 550 nm), as shown in **Figure 5.3**. These complementary ellipsometry and UV-vis results further suggest a constant concentration of DWNTs and polymer in every bilayer, which is in agreement with the PDDA/(SWNT+DOC) system described in Chapter IV.

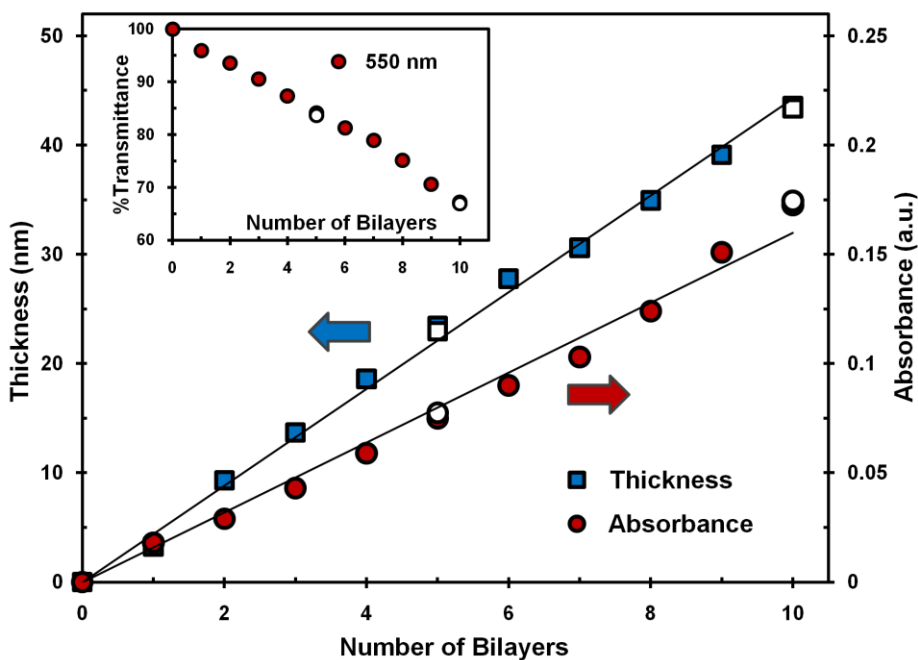


Figure 5.2. Thickness of PDDA/(DWNT+DOC) thin films as a function of the number of bilayers deposited. The solid lines are linear curve fits. Transmittance was calculated from absorbance data. White points with black outlines are values after 20 min of exposure to nitric acid vapor.

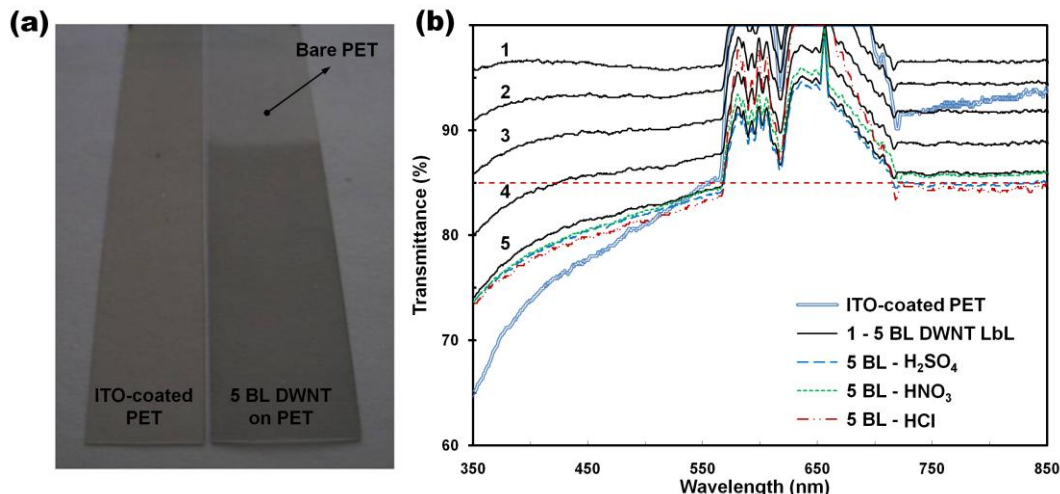


Figure 5.3. (a) Photograph of a 100 Ω/sq single side ITO-coated PET and a 5 BL DWNT assembly (103 Ω/sq) on both sides of PET. (b) Transmittance spectra of a ITO-coated PET and $[\text{PDDA}/(\text{DWNT}+\text{DOC})]_n$ ($n = 1-5$) on PET. Absorbance of the LbL thin films, coated on both sides of PET was divided by two to produce the data shown in (b). The dotted lines are transmittance of $[\text{PDDA}/(\text{DWNT}+\text{DOC})]_5$ after sulfuric, nitric, and hydrochloric acid treatment.

Figure 5.2 shows there is very little change in thickness and absorbance following acid vapor exposure. Previous studies indicated that swelling of CNT networks (increase in CNT spacing) occurred with acid doping due to denser layers of acidic anions around the individual nanotubes.^{155,159} In spite of this swelling effect, some CNT thin films have shown a significant decrease in thickness following acid doping. For example, a sprayed SWNT film was reported to have undergone a 25% thickness reduction due to the removal of bulky surfactant.⁴¹ The minimal reduction of thickness for the present LbL assemblies suggests a minimum amount of surfactant associated with CNT during deposition. In some LbL systems, CNT assemblies with a polymeric stabilizer showed more than 30% thickness reduction after sulfuric acid treatment,¹³⁷ suggesting that these films contained an excessive amount of polymer.

SEM surface images of [PDDA/(DWNT+DOC)]₆ films before and after nitric acid treatment are shown in **Figure 5.4**. What appears to be a bundled DWNT network is more clearly seen following acid treatment (**Figure 5.4(b)**). DOC exfoliation of individual DWNTs in deionized water ultimately results in a uniform distribution on the substrates.^{138,139} During deposition, the nanotubes bundle somewhat due to their high concentration in the deposited film, which creates a strong network and high electrical conductivity. Before treatment (**Figure 5.4(a)**), the surface of the film was covered by an insulating layer (polymer and/or surfactant) that made the DWNT network difficult to observe. After nitric acid treatment for 20 min, a homogeneous DWNT network was exposed due to removal of PDDA and DOC (**Figure 5.4(b)**). This removal of insulating materials enables more direct contacts between the highly conductive nanotubes. It is also believed that HNO₃ enhances conductivity through the formation of a charge-transfer complex between DWNTs and NO₃⁻ layers around the individual nanotubes, which promote bundling into thicker nanotube ropes and improved alignment of these ropes.^{155,159,161} TEM cross-sectional micrographs (**Figures 5.4(c)** and **(d)**) illustrate a highly inter-diffused nanostructure, indicating that dark and light grey areas are DWNT-rich and PDDA-rich regions, respectively, and the darkest black dots are catalyst impurities from the HIPCO process. In addition to highlighting thin film structure, the TEM images verify the inner diameter of an individual DWNT (~ 3 nm) and the lack of little change in the [PDDA/(DWNT+DOC)]₁₀ film thickness by nitric acid treatment.

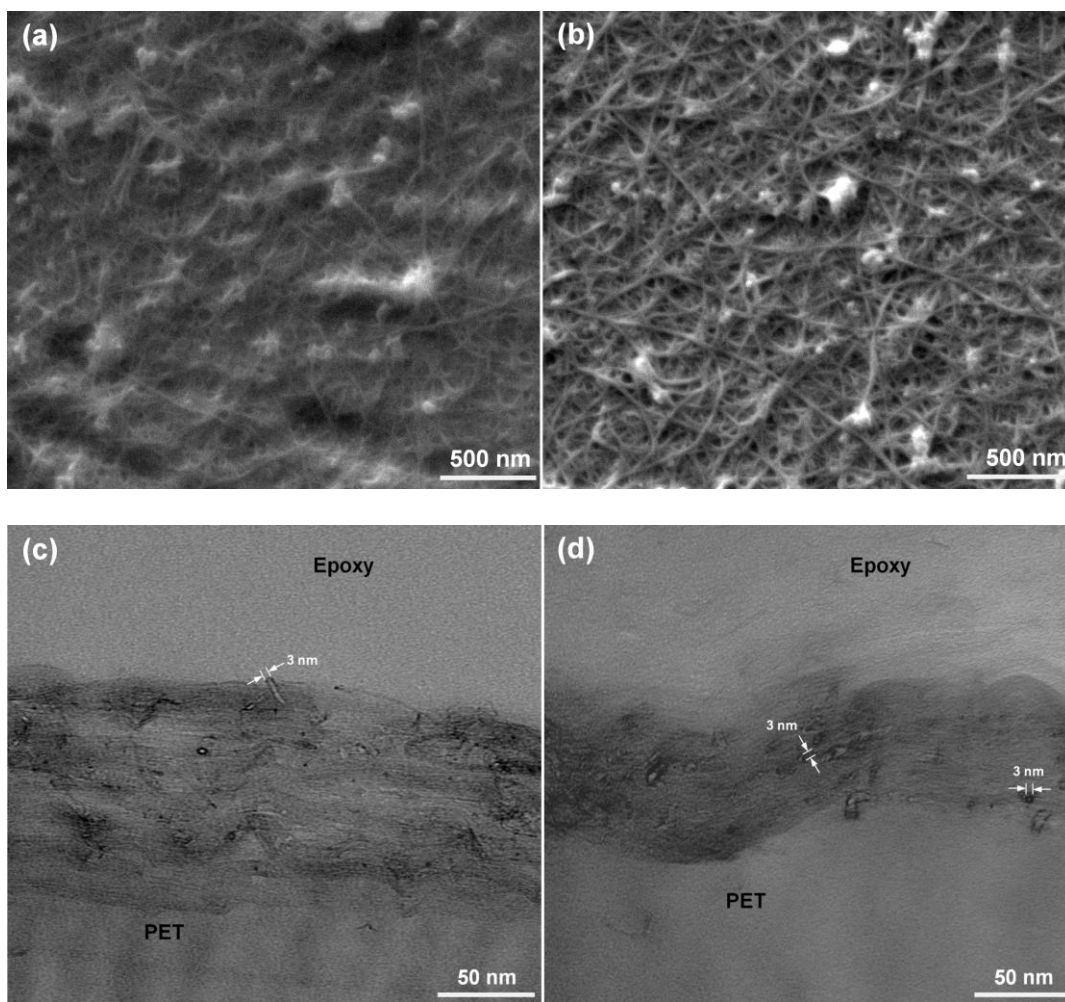


Figure 5.4. SEM surface images of [PDDA/(DWNT+DOC)]₆ on PET (a) before and (b) after 20 min exposure to nitric acid vapor. TEM cross-sections of [PDDA/(DWNT+DOC)]₁₀ (a) before and (b) after 20 min treatment with nitric acid.

5.3.2 Optoelectronic Performance of Carbon Nanotube Assemblies

Sheet resistance of [PDDA/(DWNT+DOC)]_n and [PDDA/(EA-SWNT+DOC)]_n assemblies on PET was measured and plotted as a function of their visible light transmittance, which decreased with increasing the number of BLs deposited, as shown in **Figure 5.5(a)**. Sheet resistance significantly decreases with increasing the number of BLs, along with a gradual decrease in %T. [PDDA/(DWNT+DOC)]₁₀ thin films achieve sheet

resistance as low as 127 Ω/sq (with 67.2% transmittance) at 10 bilayers and 1180 Ω/sq (with 93.5% T) for just two BLs. The PDDA/(EA-SWNT+DOC) system exhibits the same optoelectronic trend, with higher sheet resistance than, and similar transmittance to, the DWNT system. This reduction in sheet resistance is due to increased connectivity of the nanotube network.¹¹⁵ A 5 BL PDDA/(DWNT+DOC) film has the best optoelectronic performance of 309 Ω/sq with 84.2% transmittance, which meets the criteria for touch screens (500 Ω/sq , 85% T).²⁷

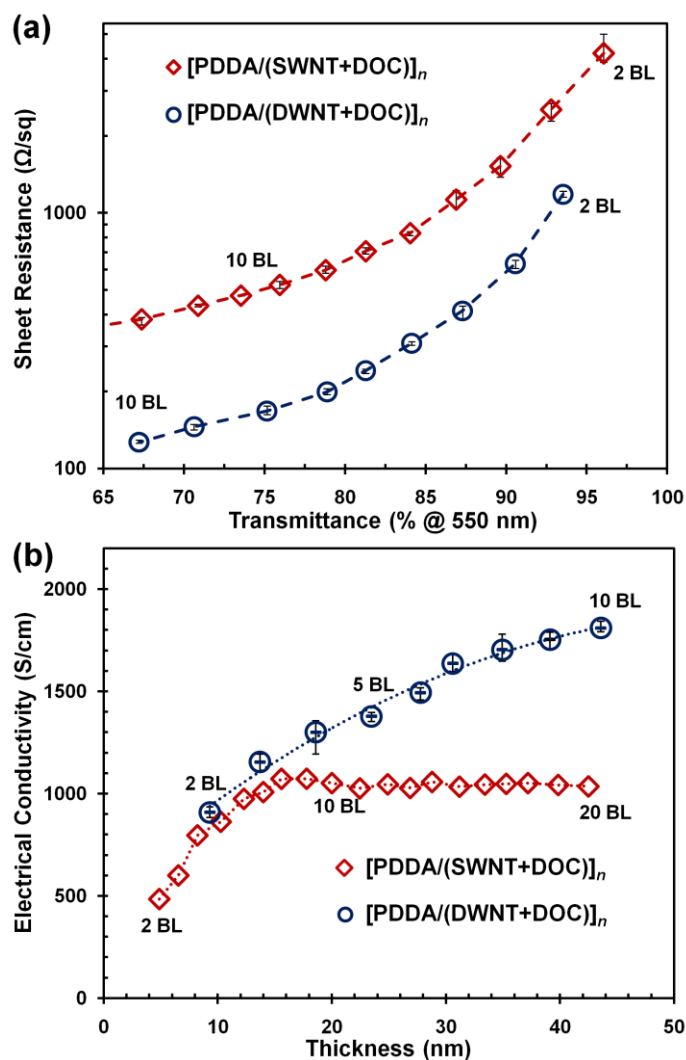


Figure 5.5. (a) Optoelectronic performance and (b) electrical conductivity as a function of thickness for the $[\text{PDDA}/(\text{EA-SWNT}+\text{DOC})]_n$ and $[\text{PDDA}/(\text{DWNT}+\text{DOC})]_n$ systems.

Electrical conductivity of these films, shown in **Figure 5.5(b)**, was obtained by multiplying the inverse of sheet resistance by ellipsometric film thickness. The gradual increase from 909 to 1810 S/cm, for the PDDA/(DWNT+DOC) system, suggests an increase in the density of intersecting pathways for electron transport (due to interconnection between DWNTs in upper and lower layers) as the nanotube network transitions from two to three-dimensional with increasing layers. The DWNT-based assembly's conductivity is expected to converge on a constant value beyond 10 bilayers, much like the EA-SWNT film. The PDDA/(EA-SWNT+DOC) system also shows a gradual increase in conductivity up to 10 BLs and then levels off at ~ 1050 S/cm. This behavior matches the previous study of CNT types described in Chapter III. The conductivity of 1810 S/cm is low relative to a vacuum filtered SWNT film (6700 S/cm)²⁸ and sprayed SWNT film (5500 S/cm),⁴¹ but it is higher than other CNT-based LbL assemblies.^{60,61,63} This relatively high conductivity is due to thin PDDA and DWNT deposition and relatively mild sonication used for the individual nanotubes. Acid treatment further improves the conductivity of the present assemblies, making them comparable to the highest conductivity CNT films.

5.3.3 Influence of Acid Treatment on Sheet Resistance

Even when SWNT is replaced by DWNT, the sheet resistance of as-assembled nanotube films is higher than the requirement for replacing the best ITO. It is believed that excessive polymer and surfactant disrupt connections between CNTs. Several studies have reported the improvements in electrical conductivity of SWNTs with acid treatment,^{41,42,137,155} but the combination of heat and acid treatments on the transparency

and electrical conductivity of CNT assemblies has never been examined, especially when using surfactant-stabilized SWNTs. This combination of two treatments results in greater electrical conductivity for a thin film prepared using the LbL method. As previously mentioned, strong acidic anions form a charge-transfer complex around individual CNTs. Additionally, similar to previous surfactant/CNT thin films,^{41,157,160} strong acids remove the insulating materials from these PDDA/(CNT+DOC) films.

In **Figure 5.6**, nitric acid treatment is shown to dramatically reduce the sheet resistance of PDDA/(HiPCO-SWNT+DOC) assemblies on glass slides, regardless of whether prior heat treatment had been performed. These are the same SWNT assemblies described in Chapter III. An unheated 20 BL thin film achieves a resistance of 324 Ω/sq following nitric acid treatment. When nitric acid treatment follows heating for 5 min at 300 °C, resistance drops to 303 Ω/sq . Moreover, the combined effect of heat and acid treatments results in a film that is an order of magnitude more conductive than it was prior to the post treatments. The conductivity of a [PDDA/(HiPCO-SWNT+DOC)]₂₀ film reaches 1430 S/cm (23 nm thick with a sheet resistance of 303 Ω/sq) after 300 °C heating for 5 min and nitric acid treatment. This conductivity is much higher than that of a heated 20 BL film prior to acid treatment (618 S/cm) and LbL thin films with anionic polymer-wrapped SWNTs and polycations (< 50 S/cm).^{60,61} Although some SWNT films made by vacuum filtration (6700 S/cm)²⁸ and direct CVD (2026 S/cm)⁴⁰ have higher conductivities than the present LbL films, they do not exhibit high transparency (< 70% T), which precludes them from use in optoelectronic devices.

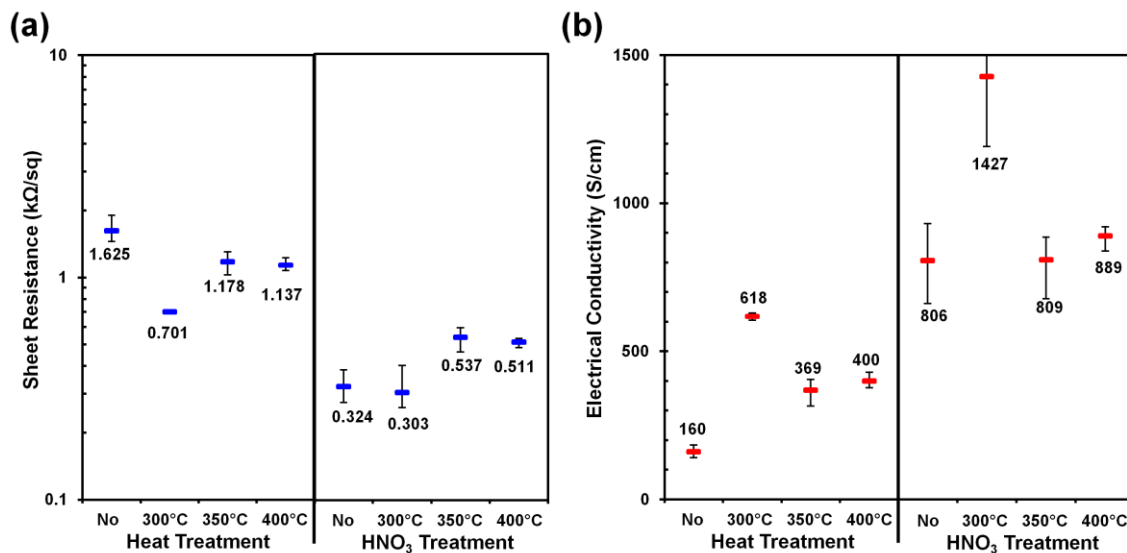


Figure 5.6. (a) Sheet resistance and (b) electrical conductivity of [PDDA/(HiPCO-SWNT+DOC)]₂₀ thin films after 300, 350, and 400 °C heat treatment for 5 min and nitric acid treatment. The values after heat treatment are from **Figure 4.9** in Chapter IV.

The changes in sheet resistance and thickness of LbL films due to heat and acid treatments are summarized in **Figure 5.7**. Reduction of sheet resistance with acid treatment is greater than heat treatment, becoming as much as 82 % lower than that of untreated 20 BL films. Much like the DWNT films in Section 5.3.1, acid treatment alone does not alter film thickness, so white and black (a) and grey and black rectangles (c, g, k, and m) have the same values in **Figure 5.7**. This suggests that LbL assembly minimizes the amount of surfactant associated with SWNT during deposition (*i.e.*, there is little excess surfactant within the conductive thin films). Additionally, annealing of acid treated films increases the sheet resistance, suggesting that the acid doping can be reversed with heat (c" and k" in **Figure 5.7**). If both treatments are used, the proper order is heat followed by acid treatment.

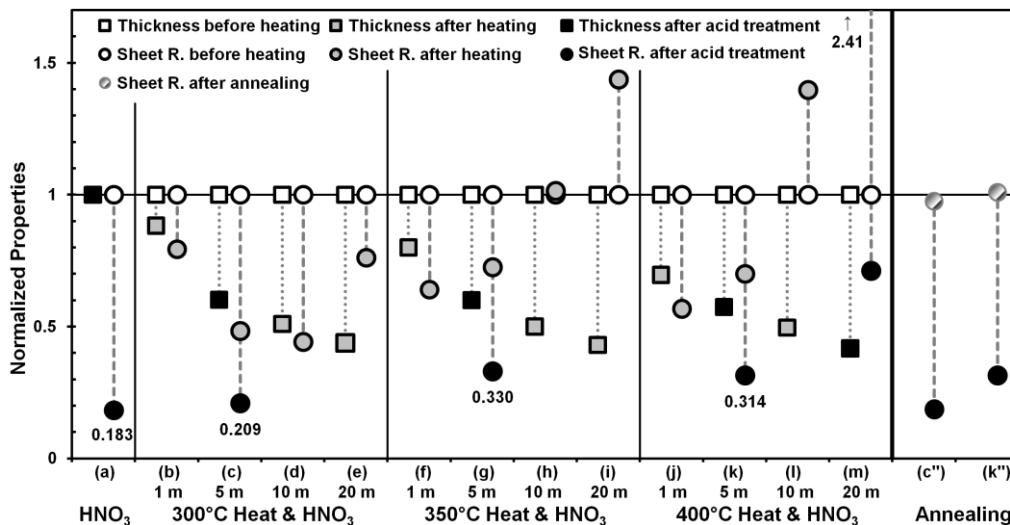


Figure 5.7. Normalized thickness and sheet resistance of [PDDA/(HiPCO-SWNT+DOC)]₂₀ thin films after post-treatments, such as only nitric acid treatment (a), heat treatment (b–m), heat and acid treatments (c, g, k, m), and annealing after heat and acid treatments (c'', k''). Rectangles and circles mean thickness and sheet resistance, respectively. White, grey, black, and gradient colors are samples before heat treatment, after heat treatment, after acid treatment, and after annealing, respectively.

Most prior acid treatment studies have been performed with dip treatment (*i.e.*, immersing the films into a strong acid bath).¹⁶⁰ Dip treating makes PET substrates brittle or even causes shrinkage. Moreover, dip treated CNT thin films readily de-adhere from substrates during rinsing. This instability due to acid treatment has been reported in multiple studies.^{158,160} In the present study, acid treatment involved exposing films to vapor by heating the acid in a 70 °C water bath. **Figure 5.8** shows sheet resistance of DWNT assemblies after acid treatment with nitric, hydrochloric, or sulfuric acid for increasing time periods. Nitric acid (b–m in **Figure 5.8**) dramatically reduced the sheet resistance of as-assembled 5 BL PDDA/(DWNT+DOC) thin films, from 309 to 107 Ω/sq, after a 10 min acid exposure. Acid type plays a significant role in reducing sheet resistance. Nitric acid treatment provides the lowest resistance, while hydrochloric and

sulfuric acids result in values that are nearly double that of HNO_3 . Uncertainty remains about why nitric acid is the most effective dopant, although it can be reasonably assumed that it is related to the intensity of doping of individual nanotubes and degradation of the surrounding insulating material. Dipped films have shown that H_2SO_4 is a stronger dopant than HNO_3 (and much more than HCl).^{156,158} The use of vapor treatment in the present work is a significant difference. In dip treatment, the amount of acidic anions is that of the solution, while the vapor pressure is a more important factor for vapor treatment. The vapor pressure is 2, 8, and 167 mm Hg at room temperature for fuming H_2SO_4 , HNO_3 , and HCl , respectively.¹⁶⁴ The size of the sulfate anion is bigger than the nitrate anion and much more than the chloride. Additionally, it's been suggested that removal of insulating surfactant is more important than classical doping for these acid treatments.⁴¹ Nitric acid more effectively removes residual surfactant than sulfuric acid.

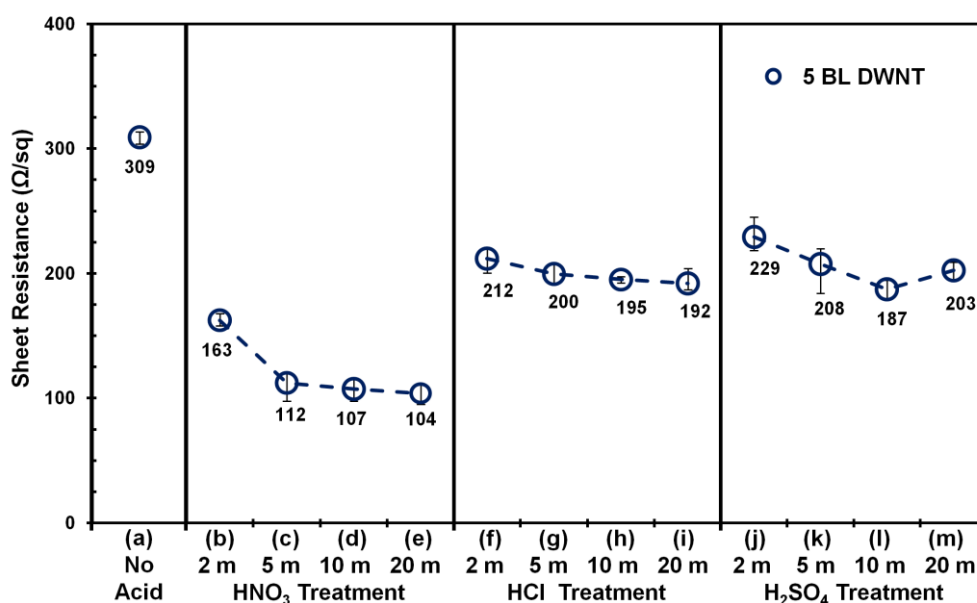


Figure 5.8. Sheet resistance of $[\text{PDDA}/(\text{DWNT}+\text{DOC})]_5$ after acid treatment for 2 to 20 min with nitric acid, hydrochloric acid, and sulfuric acid, respectively. (a) is the sheet resistance of an as-assembled 5 BL DWNT thin film.

To understand the effect of each acid treatment, CNT LbL films were characterized by EDX, FT-IR, and SEM. **Figure 5.9** shows the EDX analysis, which shows the composition of each thin film. Before acid treatment, 5 BL DWNT films were composed of 93.4 wt% carbon and 2.76 wt% oxygen. The content of carbon increased, and that of oxygen decreased, after each acid treatment. **Table 5.1** summarizes these changes. Nitric acid treatment for 20 min resulted in a 0.89% increase in carbon content (by weight) and a 29.7% decrease in oxygen content. There were 0.51% and 0.12% increase and 17.1% and only 4.0% decrease after hydrochloric and sulfuric acid treatments, respectively. This result suggests that PDDA and DOC molecules are more effectively removed by nitric acid vapor than other two acids.

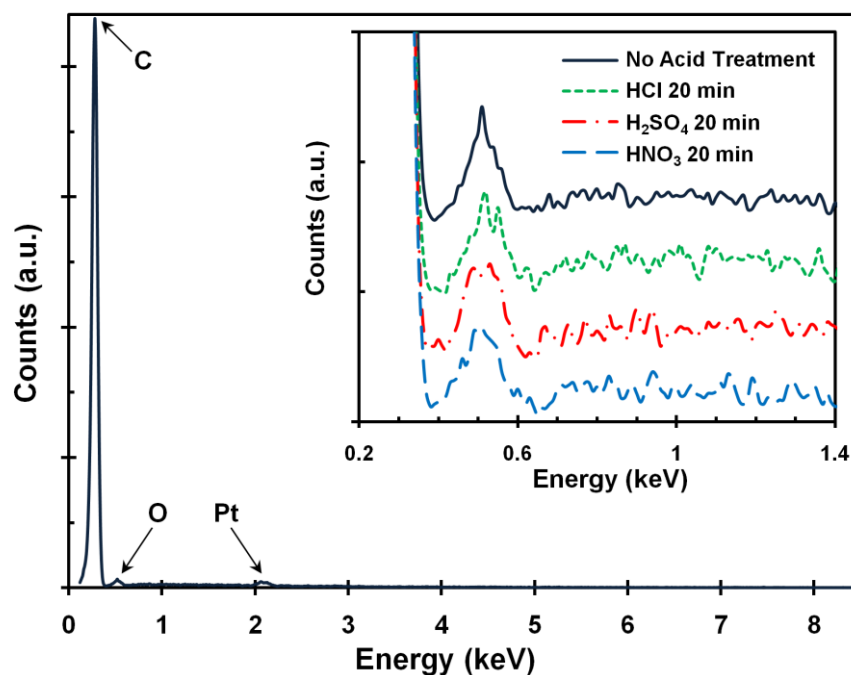


Figure 5.9. EDX spectrum of [PDDA/(DWNT+DOC)]₅ before acid treatment. Platinum was from ~ 10 nm thin coating for SEM images. The inset contains spectra of the 5BL DWNT films after 20 min nitric acid and sulfuric acid treatments, respectively.

Table 5.1. Carbon and Oxygen Contents in DWNT and EA-SWNT Films before and after Acid Treatment

System	Acid Treatment	C Content (wt%)	C Increase (%)	O Content (wt%)	O Decrease (%)
[PDDA/(DWNT+DOC)] ₅	No	93.4	-	2.76	-
	2 min HNO ₃	93.6	0.16	2.53	5.6
	5 min HNO ₃	94.0	0.63	2.09	22.0
	20 min HNO ₃	94.2	0.89	1.96	29.7
	20 min HCl	93.8	0.51	2.29	17.1
	20 min H ₂ SO ₄	93.5	0.12	2.65	4.0
[PDDA/(EA-SWNT+DOC)] ₁₀	No	97.0	-	2.97	-
	20 min HNO ₃	98.4	1.41	1.60	46.1

The DWNT networks after each acid treatment were also characterized by SEM (**Figure 5.10**). 20 min nitric acid treatment exposes a homogeneous DWNT network, while more hazy DWNT networks are observed after 20 min hydrochloric and sulfuric acid treatments due to less removal of insulating molecules. EDX and SEM together suggest that the removal of insulating material is the main factor in resistance reduction of DWNT-based assemblies, rather than acid doping effect. Nitric acid seems to be the most effective at degrading PDDA and DOC, despite having a lower vapor pressure than HCl. The low solution concentration of hydrochloric acid (37%) may account for this discrepancy.

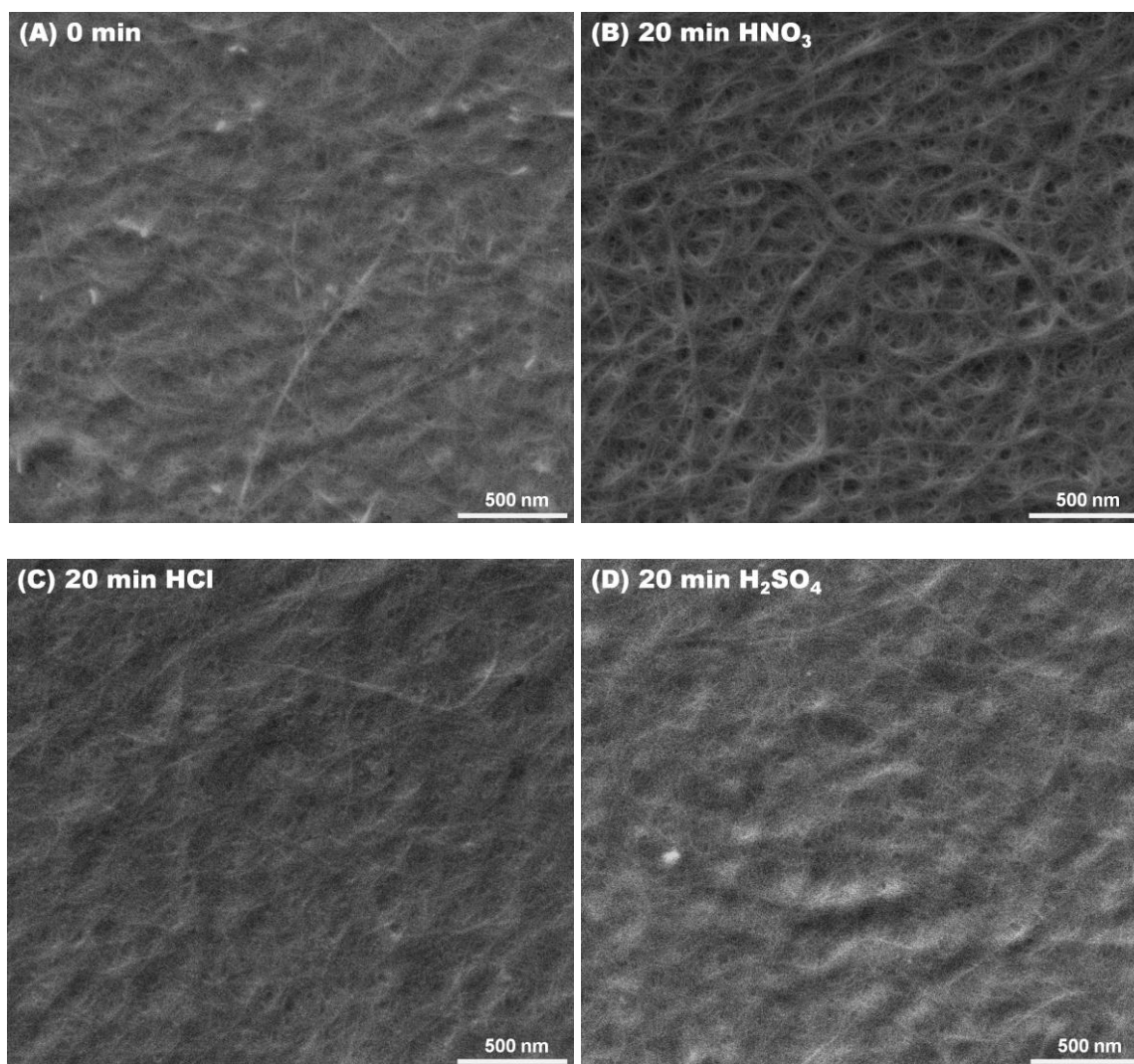


Figure 5.10. SEM surface images of [PDDA/(DWNT+DOC)]₅ on PET (a) before and after (b) 20 min HNO₃, (c) 20 min HCl, and (d) 20 min H₂SO₄ treatments, respectively.

Figure 5.11 shows the effect of nitric acid treatment on [PDDA/(EA-SWNT+DOC)]₅, [PDDA/(DWNT+DOC)]₅, and [PDDA/(DWNT+DOC)]₁₀ as a function of exposure time (from 2 to 20 min). In just two minutes, all three films exhibit a remarkable decrease in sheet resistance. Further acid treatment, however, results in only a modest decrease in sheet resistance, relative to the first 2 min, especially beyond five minutes of exposure. 20 min nitric acid treatment did not achieve significantly lower

sheet resistance than a 10 min treatment. It is likely that any insulating material present is degraded very quickly due to the very thin nature of these films (< 50 nm).

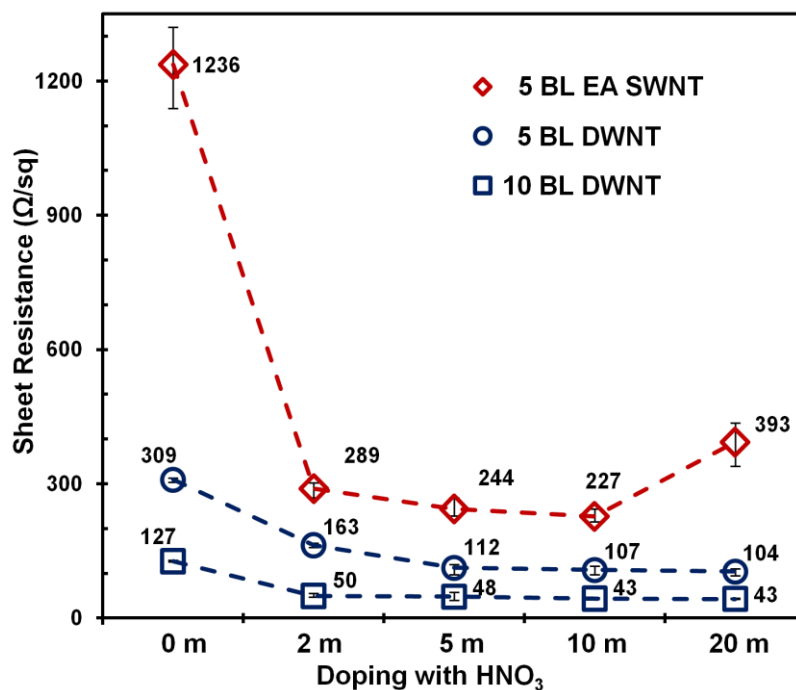


Figure 5.11. Sheet resistance of $[\text{PDDA}/(\text{EA-SWNT}+\text{DOC})]_5$, $[\text{PDDA}/(\text{DWNT}+\text{DOC})]_5$, and $[\text{PDDA}/(\text{DWNT}+\text{DOC})]_{10}$ as a function of nitric acid treatment time.

To better understand the compositional changes due to nitric acid treatment, FT-IR analysis of $[\text{PDDA}/(\text{DWNT}+\text{DOC})]_{25}$ films was performed, as shown in **Figure 5.12(a)**. The FT-IR spectrum of the film before nitric acid treatment is similar to that of the (PDDA+MWNT) nanocomposite film in a previous study, providing the peak assignments of PDDA and the (PDDA+MWNT) film.^{165,166} Those absorbance peaks at 3386, 2928, and 2864 cm^{-1} in the $[\text{PDDA}/(\text{DWNT}+\text{DOC})]_{25}$ film were also observed in the (PDDA+MWNT) film. The 3386 cm^{-1} peak is attributed to a strong O–H stretching

vibration due to DOC. As expected, this peak disappeared from the spectrum after nitric acid treatment, along with a decrease in the intensity of the peaks at 2928 and 2864 cm^{-1} , both attributed to CH stretching from PDDA and DOC. Additionally, the C=O of carboxylic groups on DOC exhibits a sharp band at 1715 cm^{-1} before acid treatment, but this became a broad band centered at 1695 cm^{-1} afterward, which indicates that this vibration band is changed due to PDDA and DOC removal. FT-IR spectra after nitric acid treatment, from 2 to 20 min, did not show any significant differences, indicating removal of insulating materials due to nitric acid vapor was largely completed in the first two minutes. As a complementary result, EDX (**Figure 5.12(b)**) shows no significant decrease in oxygen concentration from 5 to 20 min exposure. As shown in **Table 5.1**, nitric acid treatment for 5 min caused a 22.0% decrease in oxygen content, which is almost the same after 20 min. FT-IR and EDX analyses suggest that the penetration of acid vapors through the film is nearly instantaneous. Furthermore, the SEM surface images in **Figure 5.13** support this assertion by showing that most insulating materials were removed after 2 min exposure to nitric acid vapor (and a 5 min treatment exhibited the same DWNT network as a 20 min treatment). Additionally, acid treating beyond 10 min produced no additional improvement for DWNT films and an increased sheet resistance for SWNT films. It is believed that some modest damage of CNTs occurs due to excessive acid treatment (*e.g.*, sidewall oxidation),¹⁵² causing the observed increase in sheet resistance.¹⁵⁹

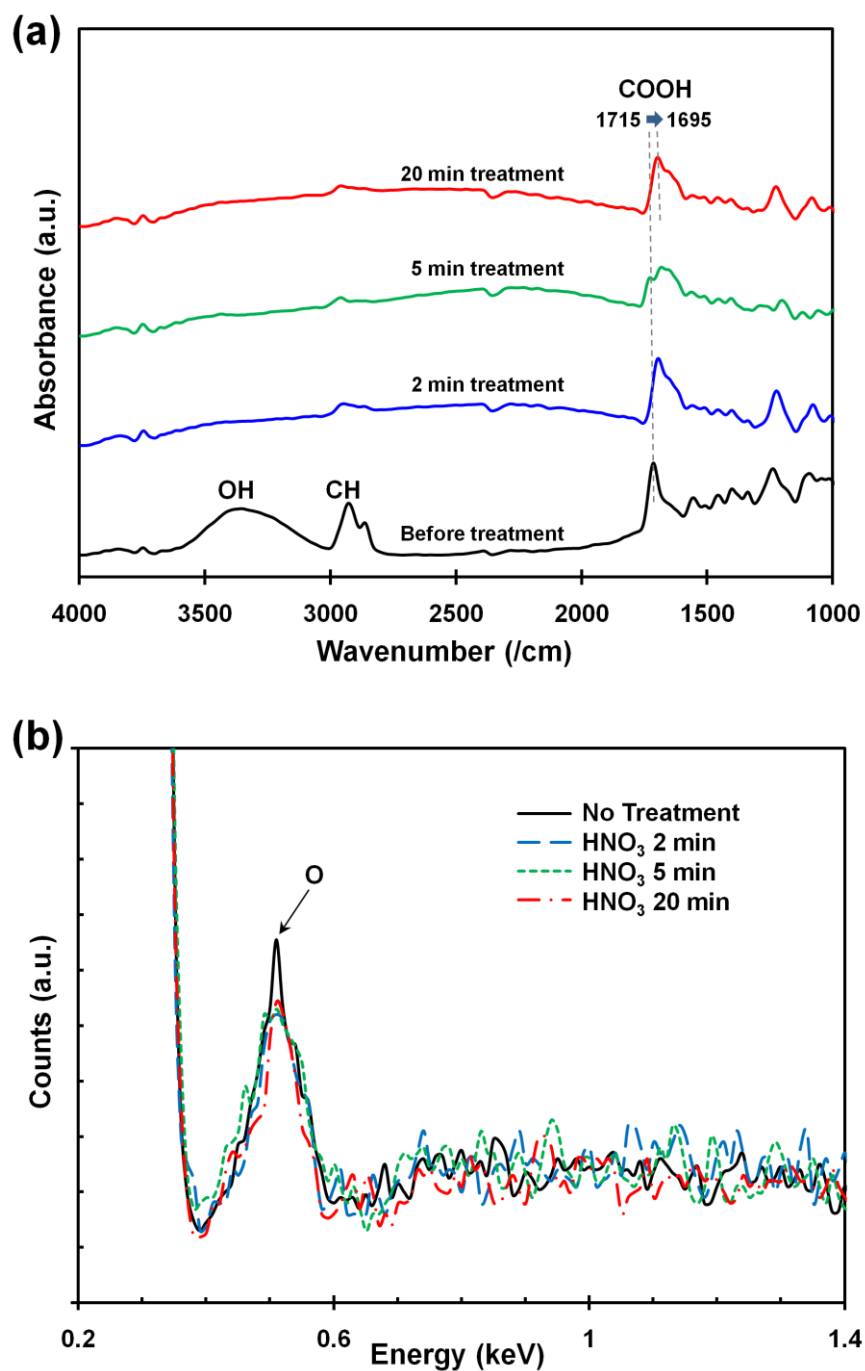


Figure 5.12. (a) FT-IR spectra of [PDDA/(DWNT+DOC)]₂₅ before and after nitric acid treatment, from 2 to 20 min. These spectra are magnified and overlaid with arbitrary offset for clarity. (b) EDX spectra of the [PDDA/(DWNT+DOC)]₅ before and after nitric acid treatment, from 2 to 20 min exposure time.

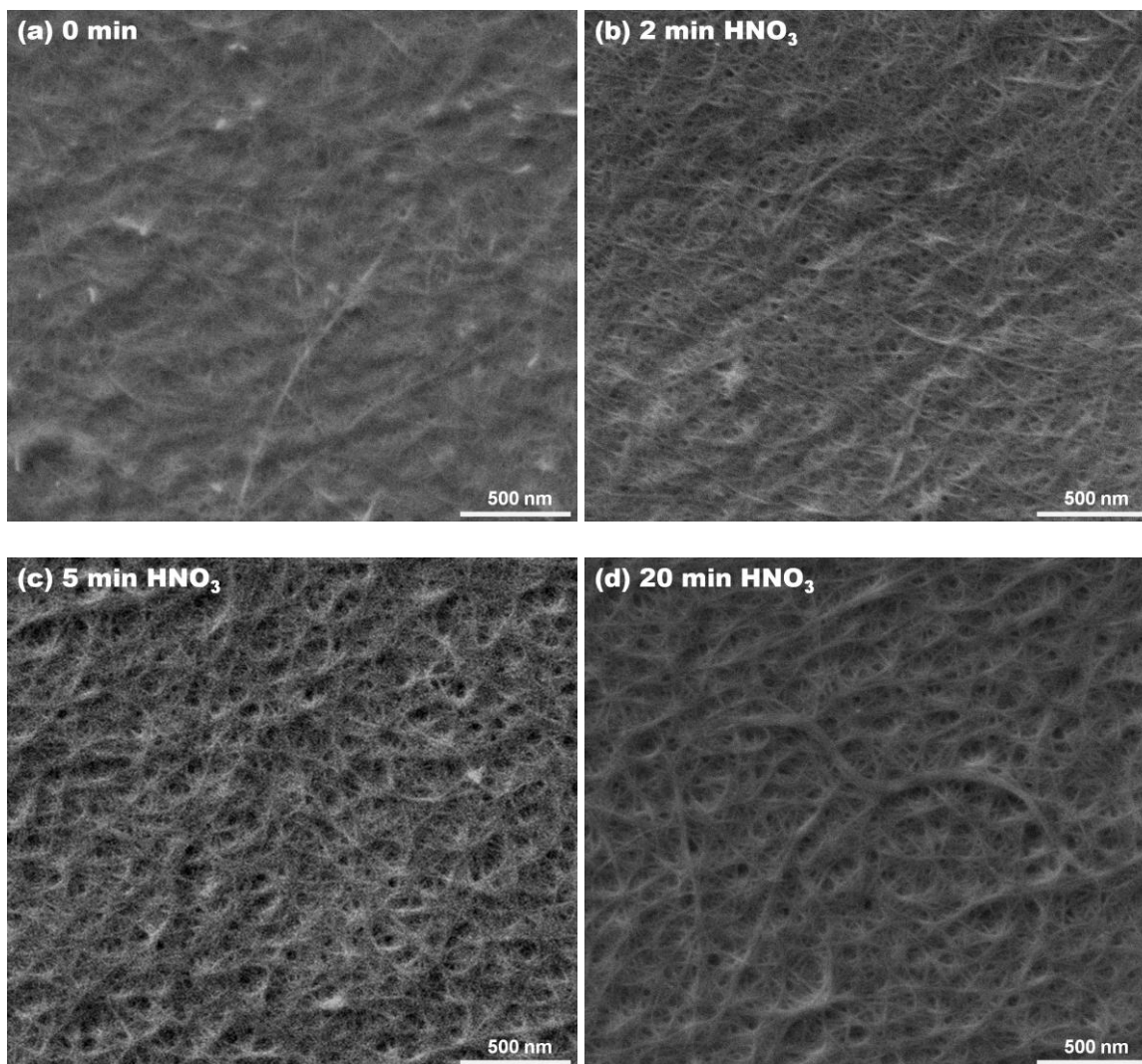


Figure 5.13. SEM surface images of [PDDA/(DWNT+DOC)]₅ on PET (a) before and (b) after 2 min, (c) 5 min, and (d) 20 min HNO₃ exposure, respectively.

In addition to exposure time, CNT type shows a different trend of sheet resistance by nitric acid treatment. In the first five minutes, the 5 BL EA-SWNT film exhibits an order of magnitude decrease in sheet resistance, while the 5 BL DWNT film decreases by only a factor of three. A 10 BL DWNT film exhibits the same trend in sheet resistance as the 5 BL DWNT film. EDX analysis, in **Figure 5.14** and **Table 5.1**, helps to explain this

trend by revealing a 46.1% decrease in oxygen weight of the 10 BL EA-SWNT film and more than a 29.7% decrease in the 5 BL DWNT film, suggesting more significant removal of insulating materials from the SWNT films. EA-SWNT films likely contain more insulating material than DWNT, in as-deposited assemblies, due to enhanced surface area (smaller diameter tubes and greater exfoliation). The SEM surface images in **Figure 5.15** support this idea by showing blurrier SWNT film surface than DWNT (**Figure 5.13(a)**) before acid treatment.

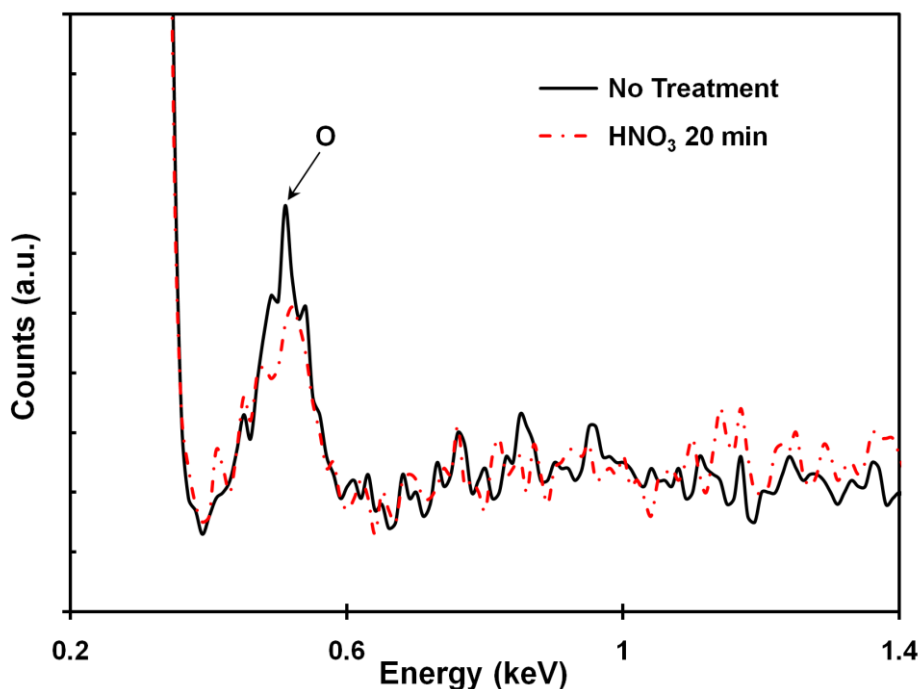


Figure 5.14. EDX spectra of $[PDDA/(EA-SWNT+DOC)]_{10}$ before and after 20 min nitric acid treatment. These spectra are magnified to emphasize oxygen content.

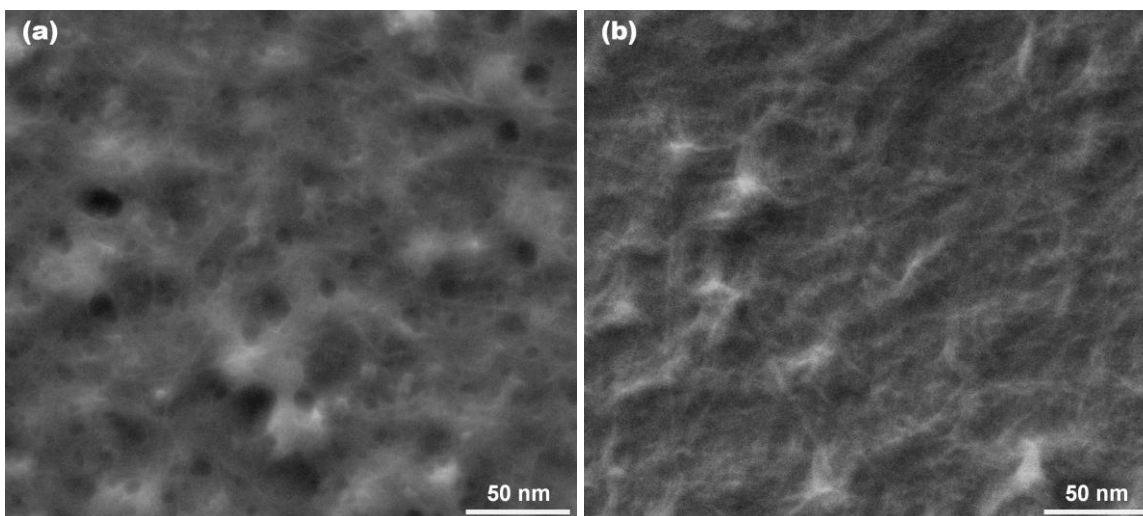


Figure 5.15. SEM surface images of [PDDA/(EA-SWNT+DOC)]₁₀ on PET (a) before and (b) after 20 min exposure to nitric acid vapor.

Three thin films, [PDDA/(EA-SWNT+DOC)]₅, [PDDA/(DWNT+DOC)]₅, and [PDDA/(DWNT+DOC)]₁₀, achieved 227, 107, and 43 Ω/sq sheet resistance, respectively, after 10 min exposure to HNO_3 vapor. These values are low enough to use for many optoelectronic applications. Optical transmittance of these films is 86.8%, 84.0%, and 67.1% T, respectively, as shown in **Figure 5.16**. The influence of acid treatment on the optoelectronic performance of several other CNT-based LbL films is also included in **Figure 5.16**, which highlights sheet resistance and transmittance. Sheet resistance of SWNT films, due to nitric acid treatment, is consistently reduced by a factor of five in this study and others,^{137,153} regardless of number of bilayers, while that of DWNT films was reduced by a factor of three. DWNT films with more than five bilayers exhibit sheet resistance below 100 Ω/sq , which is the lowest currently reported in the literature. This value is comparable with the best SWNT-based films produced using any other techniques and is competitive with high transparency ($\sim 85\%$ T) ITO coatings.⁴¹ The

transmittance of the 5 BL DWNT film ($> 80\%$) is unaltered by the acid treatment, as shown in **Figure 5.3**. This optoelectronic performance demonstrates the ability of LbL assemblies to achieve high transparency and low sheet resistance. Taking the inverse of the product of sheet resistance and thickness shows that the electrical conductivity of 5 BL and 10 BL DWNT films reaches 4100 and 5300 S/cm, respectively, after nitric acid treatment for 10 min. This conductivity is higher than most CNT films made by any method, except for vacuum filtration whose films are too low transparency ($\sim 70\%$) for use as ITO replacement.²⁸

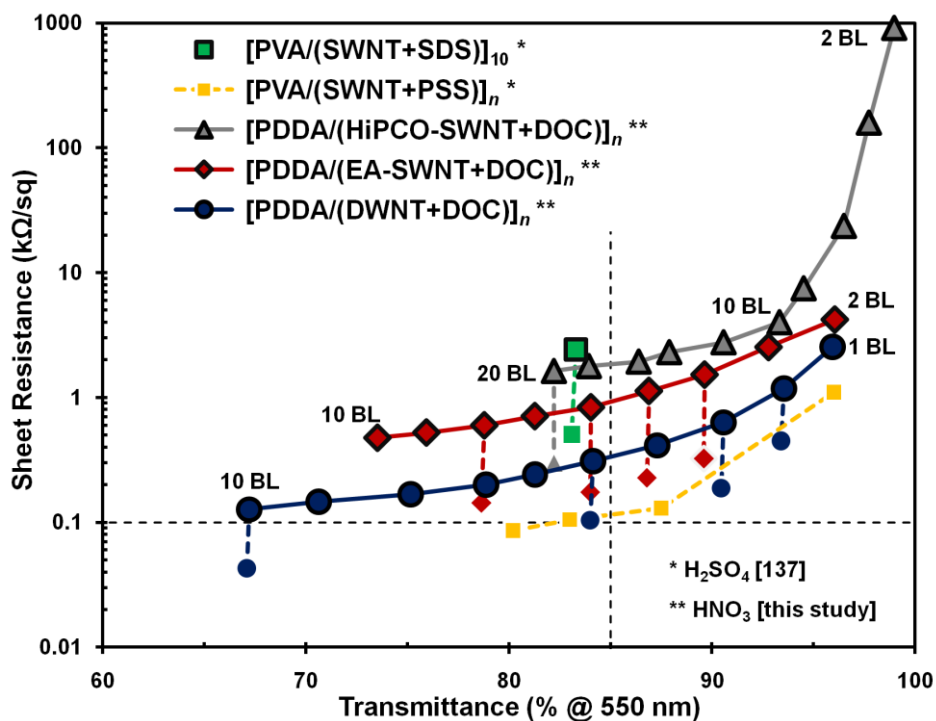


Figure 5.16. Optoelectronic performance of several CNT LbL systems before and after acid treatment. Points with the black outline are values of as-assembled LbL films and those with no outline are acid-treated LbL films.

5.3.4 Mechanical and Electrochemical Stability of Carbon Nanotube Assemblies

The bending stability of electrodes is becoming more important as flexible electronic applications continue to grow. Nitric acid-treated DWNT LbL films were compared to a commercial 100 Ω/sq ITO-coated PET sheet during a number of bending cycles, as shown in **Figure 5.17**. These films were repeatedly bent to a 1.0 cm radius of curvature (inset of **Figure 5.17**), with sheet resistance measured at the center of each specimen after each bend. DWNT films maintained constant resistance up to 100 bending cycles. In contrast, the ITO-coated PET exhibited a two order of magnitude increase in sheet resistance after 100 bending cycles. ITO and other metal oxide semiconductors readily crack due to their ceramic brittleness, while DWNT LbL films have polymeric behavior, which is ductile enough to withstand severe bending strain. This exceptional mechanical stability in LbL films can potentially be useful for flexible electronics.

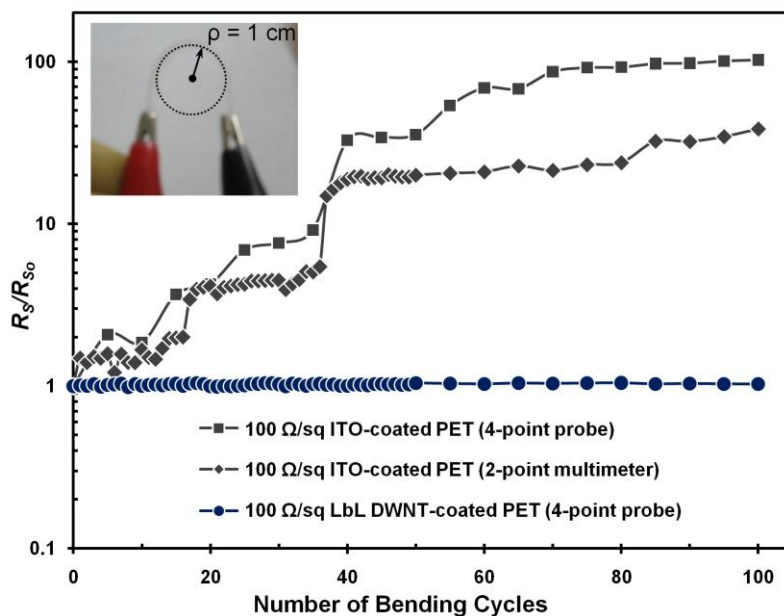


Figure 5.17. Sheet resistance as a function of bending cycles (to 1 cm radius of curvature) for 5 BL DWNT and 100 Ω/sq ITO-coated PET films. R_{s0} indicates the value prior to any bending.

Figure 5.18 compares cyclic voltammograms (CV) of HNO₃-treated 5 BL DWNT film and an ITO film (both on PET). The potential was cycled between -0.2 and 0.8 V vs. an Ag/AgCl reference electrode, with a scan rate of 100 mV/s, in 0.1 M Na₂SO₄ aqueous solution. ITO shows oxidation-reduction (redox) peaks at 0.1 and 0.3 V, respectively, indicating that ITO undergoes chemical changes under these potentiodynamic stresses. Similar peaks were found in a previous study of ITO coated glass.¹⁶⁷ A relatively large peak-to-peak separation of 0.2 V (between 0.1 and 0.3 V) is due to the physical transformation (irreversible change) occurring in the ITO film during electrochemical cycling. The DWNT LbL films have no redox peaks, suggesting they are electrochemically stable in this potential range.

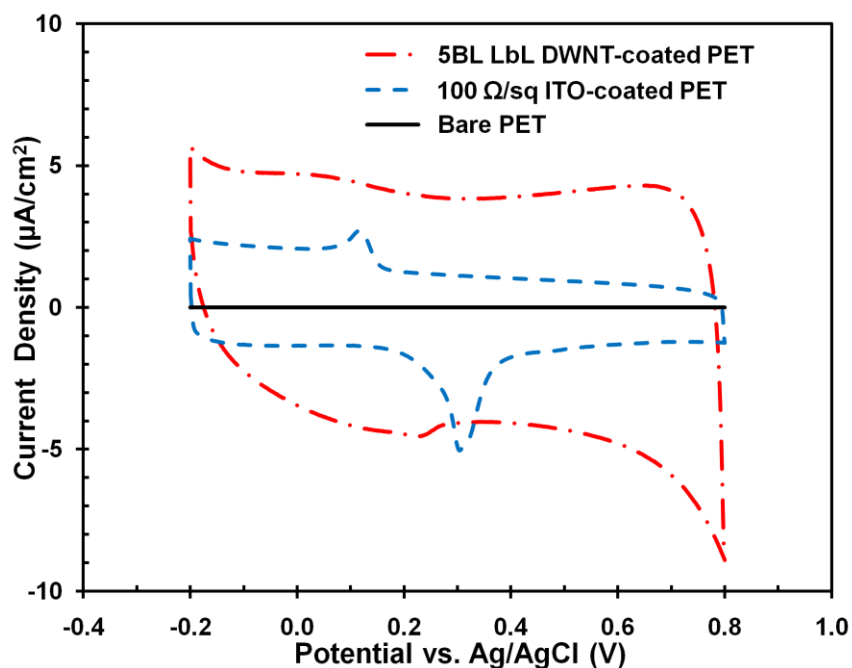


Figure 5.18. Cyclic voltammograms of a [PDDA/(DWNT+DOC)]₅ thin film on PET and a commercial $100 \Omega/\text{sq}$ ITO-coated PET. Measurements were made in 0.1 M Na₂SO₄, at room temperature, with a scan rate of 100 mV/s.

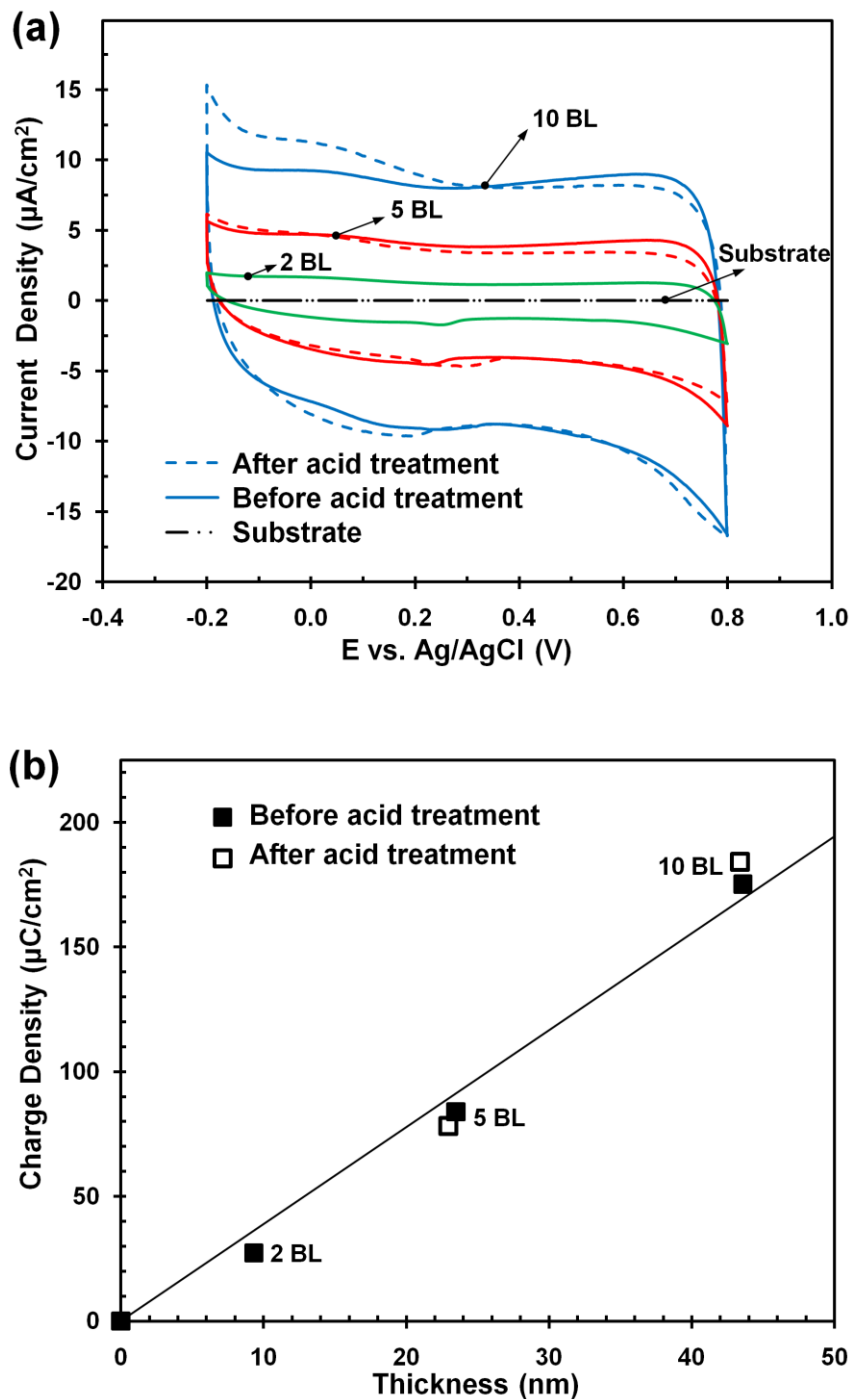


Figure 5.19. (a) Cyclic voltammograms of [PDDA/(DWNT+DOC)]_n assemblies deposited on PET. (b) Integrated charge density of each film, as a function of film thickness, was calculated from cyclic voltammograms and electrode area.

Cyclic voltammograms of nitric acid-treated DWNT films were also collected as a function of the number of BLs deposited, as shown in **Figure 5.19(a)**. These rectangular shaped curves are indicative of capacitive behavior found in carbon materials.⁶³ These voltammograms show little change before and after acid treatment, which suggests there is no chemical damage of individual nanotubes. Integrated charge density from adsorbed and desorbed ions on the DWNT film was calculated by integrating these CV curves with potential differentials. **Figure 5.19(b)** shows the linear increase in charge density as a function of the film thickness. This thickness-dependent electrochemical behavior demonstrates the tailorability of electrochemical behavior in these LbL assemblies by varying the number of BLs.

5.4 Conclusions

Highly transparent thin film electrodes were assembled through the alternate exposure of flexible substrates to aqueous mixtures of positively-charged PDDA and CNTs, stabilized with negatively-charged DOC, using the layer-by-layer method. Double-walled carbon nanotubes were substituted for SWNTs to achieve lower sheet resistance in these flexible transparent electrodes. The film growth is linear as a function of the number of DWNT bilayers deposited. DWNT thin films exhibit a significant increase in electrical conductivity after exposure to nitric acid vapor. Strong acid dopes the individual nanotubes and removes insulating material (polymer and surfactant). Additionally, these DWNT LbL coatings on PET substrates have excellent flexibility without any loss of conductivity after 100 bending cycles, unlike ITO. The sheet resistance, transparency, mechanical flexibility, and electrochemical stability of these

CNT-based LbL assemblies meet the criteria for ITO replacement in most electronics applications.

CHAPTER VI

CONCLUSION AND FUTURE WORK

The ultimate goal of this research is to fabricate transparent and flexible carbon nanotube-based electrodes that could serve as an ITO replacement. Layer-by-layer assembly was used to generate highly dense nanotube networks. A series of studies were performed to obtain thin films with the lowest sheet resistance and highest transparency. Four types of CNTs, along with heat and acid treatments, were evaluated in an effort to achieve a sheet resistance below 100 Ω/sq and visible light transmittance greater than 85%. The three stages of this work, described in Chapters III – V, and some ideas about the next steps are described here.

6.1 Influence of Carbon Nanotube Type on Optoelectronic Performance

Layer-by-layer assembly, with PDDA and CNT+DOC aqueous mixtures, generated highly transparent and electrically conductive thin films that linearly grow as a function of the number of bilayers deposited. SWNT, FWNT, and MWNT were the types of nanotubes compared. Optical transmittance and sheet resistance of these CNT assemblies showed that SWNTs produced thinner and smoother films, with higher transparency and electrical conductivity, than comparable MWNT-based films. SWNTs produced the most transparent ($> 85\%$ visible light transmittance) and electrically conductive (148 S/cm, 1.62 $\text{k}\Omega/\text{sq}$) 20-bilayer films, with a 41.6 nm thickness. With just two bilayers of PDDA/(SWNT+DOC), these films have an electrical conductivity of 40 S/cm (3.8 nm thickness with 65 $\text{k}\Omega/\text{sq}$) and transmittance greater than 97% at 550 nm.

This study demonstrates the ability of the LbL technique to produce highly transparent and conductive nanotube-based thin films.

6.2 Heat Treatment for Reducing Sheet Resistance

The PDDA/(SWNT+DOC) system produced transparent ($> 85\%$ visible light transmittance) and electrically conductive ($R_s = 1.62 \text{ } \Omega/\text{sq}$) 20-bilayer films. Heating this film to $300 \text{ } ^\circ\text{C}$ for 5 min decreased sheet resistance to $701 \text{ } \Omega/\text{sq}$ (618 S/cm conductivity), with no change in transparency, owing to the removal of insulating PDDA and DOC. Heating at 350 and $400 \text{ } ^\circ\text{C}$ actually increased sheet resistance in less than five minutes due to weakened films and possible degradation (*e.g.*, oxidation) of the nanotubes.

6.3 Acid Treatment for Reducing Sheet Resistance

Transparent electrodes made from metal oxides suffer from poor flexibility and durability. The influence of strong acids on optoelectronic properties of CNT thin films was investigated. The strong acidic anions largely removed insulating PDDA and DOC, much like heating. Unlike heating, acid doping can be performed without harming the underlying plastic substrate. Replacing SWNT with DWNT brought out further reduction in sheet resistance due to the greater metallic of DWNT. DWNT-based 5 BL assemblies exhibit $104 \text{ } \Omega/\text{sq}$ sheet resistance (4200 S/cm conductivity with 22.9 nm thickness) and 84% light transmittance at 550 nm , following nitric acid exposure. These same films are highly flexible and electrochemically stable, making them a real alternative for ITO replacement.

6.4 Future Research Plan

Transparent conductive electrodes have been studied for more than half a century and many types have been used in commercial electronic applications. These are essential for the next generation of optoelectronic devices, which are required to be lightweight, flexible, cheap, and compatible with large-scale manufacturing.¹⁶⁸ Recently, increasing demand for flexible and robust optoelectronic devices is driving the need for alternatives to metal oxides. ITO is the most widely used material for transparent electrodes, but it is brittle and becoming increasingly expensive. The work in this dissertation showed that layer-by-layer assembly, with carbon nanotubes as the conducting material, could potentially resolve this problem. It may be possible to further reduce sheet resistance, and improve transparency of these films, by incorporating graphene. Additionally, these carbon-based thin films will need to be evaluated in actual devices. These two topics of future work are described in more detail below.

6.4.1 *Graphene-Based Layer-by-Layer Transparent Electrodes*

Carbon nanomaterials, including carbon nanotubes, carbon fibers, and graphene, have generated great interest because of their unique properties. Graphene, a single layer of carbon lattice, was the subject of the most recent Nobel Prize in Physics.¹⁶⁹ Intense study has followed a simple exfoliation study of graphene (by Novoselov and co-workers in 2004) because of its remarkable electrical, chemical, and mechanical properties.¹⁷⁰⁻¹⁷³ A requirement for high-end application of graphene in electronics and photonics is tight control over lateral size, layer thickness homogeneity, and purity.¹⁷¹ Currently, the most promising methods for large scale production of graphene are based on the exfoliation

and reduction of graphene oxide.^{172,173} Graphene oxide (GO), whose structure is shown in **Figure 6.1a**, is the product of chemical exfoliation of graphite. Although GO has been known to disperse well in water, and in organic solvents after chemical modification,¹⁷² it has low electrical conductivity and is thermally unstable. Many methods have been reported to reduce GO back to graphene, using either chemical or thermal treatments.¹⁷³

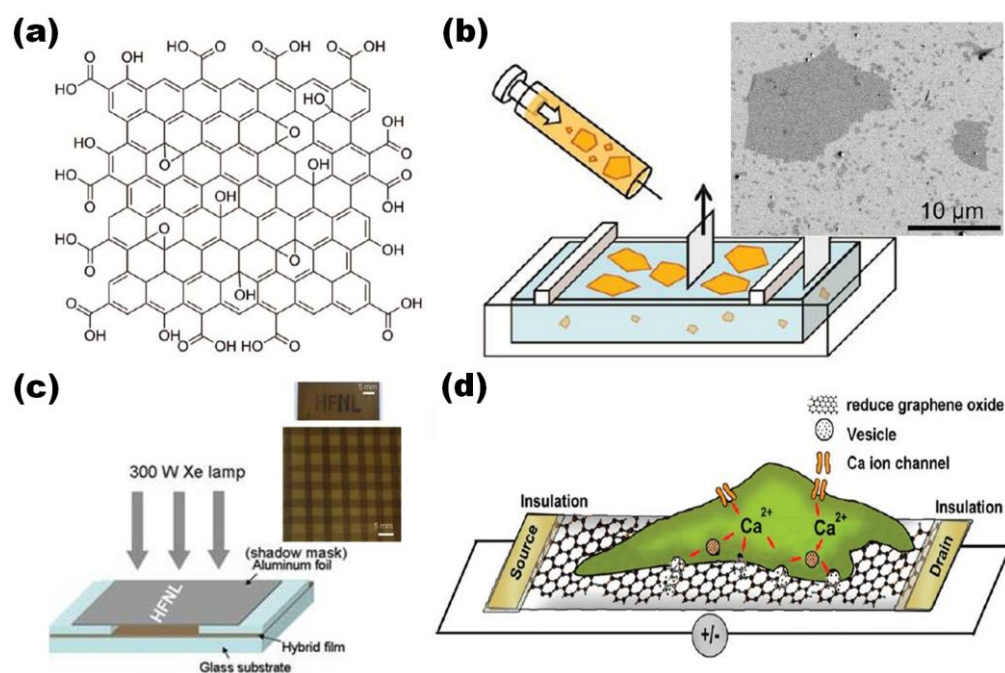


Figure 6.1. (a) Graphene oxide structure. (b) Deposition of graphene oxide sheet by dip coating and an SEM image of deposited graphene oxide pieces (reproduced from [172]). (c) Photo reduction lithography approach for fabrication of patterns on (PDDA/Graphene Oxide/PDDA/TiO)₂₀ LbL thin films (reproduced from [180]). (d) Schematic illustration of a reduced graphene oxide field-effect transistor for biosensing applications (reproduced from [183]).

Current research shows strong potential for graphene as a transparent conductor.^{168,174,175} Graphene-based thin films have been investigated with several fabrication methods, including conventional polymer/graphene composites,¹⁷³ vacuum

filtration,¹⁷⁶ and dip coating with a graphene sheet floated on an air-liquid interface (**Figure 6.1b**).^{172,177} Unfortunately, these films have not met the requirement for transparent electrodes (*i.e.*, low transparency and high sheet resistance). Layer-by-layer assembly of graphene has also been investigated.¹⁷⁸⁻¹⁸² Additionally, these films have been applied to several kinds of electronic devices, such as micro-patterning and biosensing highlighted in **Figures 6.1c** and **d**.^{180,183} At this point, only mechanical properties of these thin films are shown to be impressive. The insulating polymer molecules in these LbL assemblies prohibit them from exhibiting the low sheet resistance ($< 100 \text{ } \Omega/\text{sq}$) necessary for transparent electrodes.

Building upon the doping procedure developed in Chapter V, it is believed that graphene-based assemblies, with or without CNTs, could achieve very low sheet resistance. Thin films containing both CNT and graphene may eliminate the current problem of insulating polymer hindering the electrical contact between graphene sheets. A previous study of CNT/graphene nanocomposite thin films, prepared by vacuum filtration, showed good optoelectronic performance ($100 \text{ } \Omega/\text{sq}$ and 80% light transmittance).¹⁷⁶ An LbL assembly with MWNT and reduced GO was also reported recently,¹⁸² but the properties were not good enough for ITO replacement. Replacing MWNT with DWNT could likely dramatically improve these films. Much like with DWNT-only assemblies, graphene assemblies would be studied with regard to number of bilayers, doping acid and exposure time, and influence of nanotubes used in combination. In theory, graphene should be more conductive and transparent than DWNT, but connectivity may be an issue.

6.4.2 *Electronic Devices with Layer-by-Layer Assemblies*

Random networks of CNTs have shown promise for use in the field of transparent and flexible electronics.^{184,185} Although these networks lose the electrical properties of individual nanotubes, when metallic percolation pathways can be formed, these networks exhibit impressive characteristics. A variety of deposition techniques have been developed, but only a few can be readily scaled up. With more work, these CNT-based devices can be used as transparent displays in the next generation of hand-held electronics. Transparent electrodes are useful for flat touch panel displays (FPDs),⁸² high mobility thin film field-effect transistors (TF-FETs),^{19,185} photovoltaics,^{23,70} and organic light-emitting diodes (OLEDs).^{5,37} Most of these devices currently use ITO, although this material has several disadvantages.⁸² At present, CNT- or graphene-based electrodes are being heavily investigated for use in these optoelectronic applications. High conductivity, transparency, carrier mobility, flexibility, robustness, and environmental resistance, as shown in this dissertation, indicate that LbL assemblies are ready for proof of concept in these types of electronic devices.

Future work would include building several electronic devices using LbL assembly and evaluating their performance. Carbon-based conductive polymer composite multilayer thin films have already been fabricated by LbL assembly and shown to be useful for smart sensing (**Figure 6.2(a)**).¹⁸⁶ Sensitivity and selectivity towards types of vapors will be measured and characterized as a function of composition and number of bilayers deposited. Also, transparent capacitors and transistors could be investigated using CNT assemblies in place of ITO or other metal oxides, like those shown in **Figure 6.2(b)**.¹⁸⁵ The optically and electrically outstanding electrodes in this

study will advance the electronic performances of current capacitors and TF-FETs. In addition, tailorability of their electronic properties will be expected due to the precise tailorability of composition and thickness of LbL assembly.

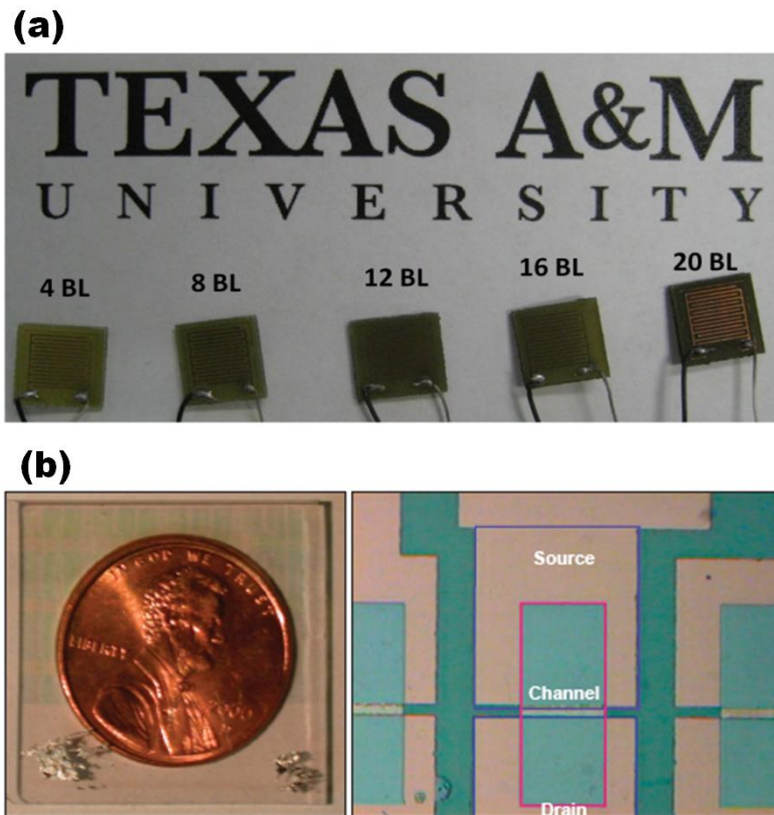


Figure 6.2. (a) An image of a series of SWNT-based assemblies deposited on vapor sensing electrodes (reproduced from [186]). (b) Metal oxide-based transparent transistors. An ITO lower layer as a gate, an aluminum–titanium oxide (ATO) upper layer as the gate dielectric, and a ZnO channel layer on a glass substrate (reproduced from [185]).

REFERENCES AND NOTES

1. Granqvist, C. G.; Hultaker, A., Transparent and conducting ITO films: New developments and applications. *Thin Solid Films* **2002**, *411* (1), 1-5.
2. Nath, P.; Bunshah, R. F.; Basol, B. M.; Staffsud, O. M., Electrical and optical properties of $\text{In}_2\text{O}_3\text{:Sn}$ films prepared by activated reactive evaporation. *Thin Solid Films* **1980**, *72* (3), 463-468.
3. Lin, Y. C.; Shi, W. Q.; Chen, Z. Z., Effect of deflection on the mechanical and optoelectronic properties of indium tin oxide films deposited on polyethylene terephthalate substrates by pulse magnetron sputtering. *Thin Solid Films* **2009**, *517* (5), 1701-1705.
4. Lan, Y. F.; Peng, W. C.; Lo, Y. H.; He, J. L., Durability under mechanical bending of the indium tin oxide films deposited on polymer substrate by thermionically enhanced sputtering. *Org. Electron.* **2010**, *11* (4), 670-676.
5. Gu, G.; Shen, Z. L.; Burrows, P. E.; Forrest, S. R., Transparent flexible organic light-emitting devices. *Adv. Mater.* **1997**, *9* (9), 725-728.
6. Cairns, D. R.; Witte, R. P.; Sparacin, D. K.; Sachsman, S. M.; Paine, D. C.; Crawford, G. P.; Newton, R. R., Strain-dependent electrical resistance of tin-doped indium oxide on polymer substrates. *Appl. Phys. Lett.* **2000**, *76* (11), 1425-1427.
7. Leterrier, Y.; Medico, L.; Demarco, F.; Manson, J. A. E.; Betz, U.; Escola, M. F.; Olsson, M. K.; Atamny, F., Mechanical integrity of transparent conductive oxide films for flexible polymer-based displays. *Thin Solid Films* **2004**, *460* (1-2), 156-166.
8. Wang, L. D.; Yang, L.; Chun, C.; Lian, D.; Yong, Q., Research on the adhesive ability between ITO anode and PET substrate improved by polyimide buffer layer. *Chin. Sci. Bull.* **2005**, *50* (6), 505-508.
9. Dawidczyk, T. J.; Walton, M. D.; Jang, W. S.; Grunlan, J. C., Layer-by-layer assembly of UV-resistant poly(3,4-ethylenedioxythiophene) thin films. *Langmuir* **2008**, *24* (15), 8314-8318.
10. Mu, H.; Li, W.; Jones, R.; Steckl, A.; Klotzkin, D., A comparative study of electrode effects on the electrical and luminescent characteristics of Alq_3 /TPD OLED: Improvements due to conductive polymer (PEDOT) anode. *J. Lumin.* **2007**, *126* (1), 225-229.
11. Радущкевич, Л. В., О Структуре Углерода, Образующегося При Термическом Разложении Окиси Углерода На Железном Контакте. *Журнал Физической Химии* **1952**, *26*, 88-95.

12. Oberlin, A.; Endo, M.; Koyama, T., Filamentous growth of carbon through benzene decomposition. *J. Cryst. Growth* **1976**, *32* (3), 335-349.
13. Iijima, S., Helical microtubules of graphitic carbon. *Nature* **1991**, *354* (6348), 56-58.
14. Thess, A.; Lee, R.; Nikolaev, P.; Dai, H.; Petit, P.; Robert, J.; Xu, C.; Lee, Y. H.; Kim, S. G.; Rinzler, A. G.; Colbert, D. T.; Scuseria, G. E.; Tomanek, D.; Fischer, J. E.; Smalley, R. E., Crystalline ropes of metallic carbon nanotubes. *Science* **1996**, *273* (5274), 483-487.
15. Dresselhaus, M. S.; Dresselhaus, G.; Charlier, J. C.; Hernandez, E., Electronic, thermal and mechanical properties of carbon nanotubes. *Philos. Trans. R. Soc. London, Ser. A* **2004**, *362* (1823), 2065-2098.
16. Yu, M. F.; Files, B. S.; Arepalli, S.; Ruoff, R. S., Tensile loading of ropes of single wall carbon nanotubes and their mechanical properties. *Phys. Rev. Lett.* **2000**, *84* (24), 5552-5555.
17. Sánchez-Portal, D.; Artacho, E.; Soler, J. M.; Rubio, A.; Ordejón, P., Ab initio structural, elastic, and vibrational properties of carbon nanotubes. *Phys. Rev. B* **1999**, *59* (19), 12678-12688.
18. Hu, J. T.; Odom, T. W.; Lieber, C. M., Chemistry and physics in one dimension: Synthesis and properties of nanowires and nanotubes. *Acc. Chem. Res.* **1999**, *32* (5), 435-445.
19. Kang, S. J.; Kocabas, C.; Ozel, T.; Shim, M.; Pimparkar, N.; Alam, M. A.; Rotkin, S. V.; Rogers, J. A., High-performance electronics using dense, perfectly aligned arrays of single-walled carbon nanotubes. *Nat. Nanotechnol.* **2007**, *2* (4), 230-236.
20. Xue, W.; Liu, Y.; Cui, T. H., High-mobility transistors based on nanoassembled carbon nanotube semiconducting layer and SiO₂ nanoparticle dielectric layer. *Appl. Phys. Lett.* **2006**, *89* (16), 163512.
21. Loh, K. J.; Kim, J.; Lynch, J. P.; Kam, N. W. S.; Kotov, N. A., Multifunctional layer-by-layer carbon nanotube-polyelectrolyte thin films for strain and corrosion sensing. *Smart Mater. Struct.* **2007**, *16* (2), 429-438.
22. Modi, A.; Koratkar, N.; Lass, E.; Wei, B. Q.; Ajayan, P. M., Miniaturized gas ionization sensors using carbon nanotubes. *Nature* **2003**, *424* (6945), 171-174.
23. Lowman, G. M.; Hammond, P. T., Solid-state dye-sensitized solar cells combining a porous TiO₂ film and a layer-by-layer composite electrolyte. *Small* **2005**, *1* (11), 1070-1073.

24. Endo, M.; Hayashi, T.; Kim, Y. A.; Terrones, M.; Dresselhaus, M. S., Applications of carbon nanotubes in the twenty-first century. *Philos. Trans. R. Soc. London, Ser. A* **2004**, 362 (1823), 2223-2238.
25. Cao, Q.; Kim, H. S.; Pimparkar, N.; Kulkarni, J. P.; Wang, C. J.; Shim, M.; Roy, K.; Alam, M. A.; Rogers, J. A., Medium-scale carbon nanotube thin-film integrated circuits on flexible plastic substrates. *Nature* **2008**, 454 (7203), 495-500.
26. Friedman, R. S.; McAlpine, M. C.; Ricketts, D. S.; Ham, D.; Lieber, C. M., Nanotechnology high-speed integrated nanowire circuits. *Nature* **2005**, 434 (7037), 1085.
27. Kaempgen, M.; Duesberg, G. S.; Roth, S., Transparent carbon nanotube coatings. *Appl. Surf. Sci.* **2005**, 252 (2), 425-429.
28. Wu, Z. C.; Chen, Z. H.; Du, X.; Logan, J. M.; Sippel, J.; Nikolou, M.; Kamaras, K.; Reynolds, J. R.; Tanner, D. B.; Hebard, A. F.; Rinzler, A. G., Transparent, conductive carbon nanotube films. *Science* **2004**, 305 (5688), 1273-1276.
29. Zhang, K.; Zhu, F. R.; Huan, C. H. A.; Wee, A. T. S., Indium tin oxide films prepared by radio frequency magnetron sputtering method at a low processing temperature. *Thin Solid Films* **2000**, 376 (1-2), 255-263.
30. Sun, J.; Gerberich, W. W.; Francis, L. F., Electrical and optical properties of ceramic-polymer nanocomposite coatings. *J. Polym. Sci., Part B: Polym. Phys.* **2003**, 41 (14), 1744-1761.
31. Kirchmeyer, S.; Reuter, K., Scientific importance, properties and growing applications of poly(3,4-ethylenedioxythiophene). *J. Mater. Chem.* **2005**, 15 (21), 2077-2088.
32. Parekh, B. B.; Fanchini, G.; Eda, G.; Chhowalla, M., Improved conductivity of transparent single-wall carbon nanotube thin films via stable postdeposition functionalization. *Appl. Phys. Lett.* **2007**, 90 (12), 121913.
33. Green, A. A.; Hersam, M. C., Colored semitransparent conductive coatings consisting of monodisperse metallic single-walled carbon nanotubes. *Nano Lett.* **2008**, 8 (5), 1417-1422.
34. Li, Z. R.; Kandel, H. R.; Dervishi, E.; Saini, V.; Xu, Y.; Biris, A. R.; Lupu, D.; Salamo, G. J.; Biris, A. S., Comparative study on different carbon nanotube materials in terms of transparent conductive coatings. *Langmuir* **2008**, 24 (6), 2655-2662.

35. Hu, L.; Hecht, D. S.; Gruner, G., Percolation in transparent and conducting carbon nanotube networks. *Nano Lett.* **2004**, 4 (12), 2513-2517.
36. Zhou, Y. X.; Hu, L. B.; Gruner, G., A method of printing carbon nanotube thin films. *Appl. Phys. Lett.* **2006**, 88 (12), 123109.
37. Zhang, D. H.; Ryu, K.; Liu, X. L.; Polikarpov, E.; Ly, J.; Tompson, M. E.; Zhou, C. W., Transparent, conductive, and flexible carbon nanotube films and their application in organic light-emitting diodes. *Nano Lett.* **2006**, 6 (9), 1880-1886.
38. Williams, Q. L.; Liu, X.; Walters, W.; Zhou, J. G.; Edwards, T. Y.; Smith, F. L., Boron-doped carbon nanotube coating for transparent, conducting, flexible photonic devices. *Appl. Phys. Lett.* **2007**, 91 (14), 143116.
39. Spotnitz, M. E.; Ryan, D.; Stone, H. A., Dip coating for the alignment of carbon nanotubes on curved surfaces. *J. Mater. Chem.* **2004**, 14 (8), 1299-1302.
40. Ma, W. J.; Song, L.; Yang, R.; Zhang, T. H.; Zhao, Y. C.; Sun, L. F.; Ren, Y.; Liu, D. F.; Liu, L. F.; Shen, J.; Zhang, Z. X.; Xiang, Y. J.; Zhou, W. Y.; Xie, S. S., Directly synthesized strong, highly conducting, transparent single-walled carbon nanotube films. *Nano Lett.* **2007**, 7 (8), 2307-2311.
41. Geng, H. Z.; Kim, K. K.; So, K. P.; Lee, Y. S.; Chang, Y.; Lee, Y. H., Effect of acid treatment on carbon nanotube-based flexible transparent conducting films. *J. Am. Chem. Soc.* **2007**, 129 (25), 7758-7759.
42. Dan, B.; Irvin, G. C.; Pasquali, M., Continuous and scalable fabrication of transparent conducting carbon nanotube films. *ACS Nano* **2009**, 3 (4), 835-843.
43. Lima, M. D.; de Andrade, M. J.; Bergmann, C. P.; Roth, S., Thin, conductive, carbon nanotube networks over transparent substrates by electrophoretic deposition. *J. Mater. Chem.* **2008**, 18 (7), 776-779.
44. Sung, J.; Jo, P. S.; Shin, H.; Huh, J.; Min, B. G.; Kim, D. H.; Park, C., Transparent, low-electric-resistance nanocomposites of self-assembled block copolymers and SWNTs. *Adv. Mater.* **2008**, 20 (8), 1505-1510.
45. Yu, X.; Rajamani, R.; Stelson, K. A.; Cui, T., Fabrication of carbon nanotube based transparent conductive thin films using layer-by-layer technology. *Surf. Coat. Technol.* **2008**, 202 (10), 2002-2007.
46. Bertrand, P.; Jonas, A.; Laschewsky, A.; Legras, R., Ultrathin polymer coatings by complexation of polyelectrolytes at interfaces: Suitable materials, structure and properties. *Macromol. Rapid Commun.* **2000**, 21 (7), 319-348.

47. Hammond, P. T., Form and function in multilayer assembly: New applications at the nanoscale. *Adv. Mater.* **2004**, *16* (15), 1271-1293.
48. Ariga, K.; Hill, J. P.; Ji, Q. M., Layer-by-layer assembly as a versatile bottom-up nanofabrication technique for exploratory research and realistic application. *Phys. Chem. Chem. Phys.* **2007**, *9* (19), 2319-2340.
49. Decher, G.; Schlenoff, J., *Multilayer thin films: Sequential assembly of nanocomposite materials*. Wiley-VCH: New York, 2003.
50. Nepal, D.; Balasubramanian, S.; Simonian, A. L.; Davis, V. A., Strong antimicrobial coatings: Single-walled carbon nanotubes armored with biopolymers. *Nano Lett.* **2008**, *8* (7), 1896-1901.
51. Dvoracek, C. M.; Sukhonosova, G.; Benedik, M. J.; Grunlan, J. C., Antimicrobial behavior of polyelectrolyte-surfactant thin film assemblies. *Langmuir* **2009**, *25* (17), 10322-10328.
52. Priolo, M. A.; Gamboa, D.; Grunlan, J. C., Transparent clay-polymer nano brick wall assemblies with tailorable oxygen barrier. *ACS Appl. Mater. Interfaces* **2010**, *2* (1), 312-320.
53. Wang, Y.; Stedronsky, E.; Regen, S. L., Defects in a polyelectrolyte multilayer: The inside story. *J. Am. Chem. Soc.* **2008**, *130* (49), 16510-16511.
54. Nohria, R.; Khillan, R. K.; Su, Y.; Dikshit, R.; Lvov, Y.; Varshramyan, K., Humidity sensor based on ultrathin polyaniline film deposited using layer-by-layer nano-assembly. *Sens. Actuators, B* **2006**, *114* (1), 218-222.
55. Li, Y.-C.; Schulz, J.; Grunlan, J. C., Polyelectrolyte/nanosilicate thin-film assemblies: Influence of pH on growth, mechanical behavior, and flammability. *ACS Appl. Mater. Interfaces* **2009**, *1* (10), 2338-2347.
56. Jain, V.; Khiterer, M.; Montazami, R.; Yochum, H. M.; Shea, K. J.; Heflin, J. R., High-contrast solid-state electrochromic devices of viologen-bridged polysilsesquioxane nanoparticles fabricated by layer-by-layer assembly. *ACS Appl. Mater. Interfaces* **2009**, *1* (1), 83-89.
57. Kim, B. S.; Park, S. W.; Hammond, P. T., Hydrogen-bonding layer-by-layer assembled biodegradable polymeric micelles as drug delivery vehicles from surfaces. *ACS Nano* **2008**, *2* (2), 386-392.
58. Kovtyukhova, N. I.; Mallouk, T. E., Ultrathin anisotropic films assembled from individual single-walled carbon nanotubes and amine polymers. *J. Phys. Chem. B* **2005**, *109* (7), 2540-2545.

59. Mamedov, A. A.; Kotov, N. A.; Prato, M.; Guldi, D. M.; Wicksted, J. P.; Hirsch, A., Molecular design of strong single-wall carbon nanotube/polyelectrolyte multilayer composites. *Nat. Mater.* **2002**, *1* (4), 257-257.
60. Shim, B. S.; Tang, Z. Y.; Morabito, M. P.; Agarwal, A.; Hong, H. P.; Kotov, N. A., Integration of conductivity transparency, and mechanical strength into highly homogeneous layer-by-layer composites of single-walled carbon nanotubes for optoelectronics. *Chem. Mater.* **2007**, *19* (23), 5467-5474.
61. Park, H. J.; Oh, K. A.; Park, M.; Lee, H., Electrical Properties and Conductivity Mapping of Thin Multilayered Films Containing Different Types of Carbon Nanotubes. *J. Phys. Chem. C* **2009**, *113* (30), 13070-13076.
62. Gheith, M. K.; Pappas, T. C.; Liopo, A. V.; Sinani, V. A.; Shim, B. S.; Motamedi, M.; Wicksted, J. R.; Kotov, N. A., Stimulation of neural cells by lateral layer-by-layer films of single-walled currents in conductive carbon nanotubes. *Adv. Mater.* **2006**, *18* (22), 2975-2979.
63. Lee, S. W.; Kim, B. S.; Chen, S.; Shao-Horn, Y.; Hammond, P. T., Layer-by-layer assembly of all carbon nanotube ultrathin films for electrochemical applications. *J. Am. Chem. Soc.* **2009**, *131* (2), 671-679.
64. Paloniemi, H.; Lukkarinen, M.; Ääritalo, T.; Areva, S.; Leiro, J.; Heinonen, M.; Haapakka, K.; Lukkari, J., Layer-by-layer electrostatic self-assembly of single-wall carbon nanotube polyelectrolytes. *Langmuir* **2006**, *22* (1), 74-83.
65. Hu, L.; Hecht, D. S.; Gruener, G., Carbon nanotube thin films: Fabrication, properties, and applications. *Chem. Rev.* **2010**, *110* (10), 5790-5844.
66. Smith, G. B.; Niklasson, G. A.; Svensson, J. S. E. M.; Granqvist, C. G., Noble-metal-based transparent infrared reflectors - experiments and theoretical analyses for very thin gold-films. *J. Appl. Phys.* **1986**, *59* (2), 571-581.
67. Granqvist, C. G., Transparent conductive electrodes for electrochromic devices - a review. *Appl. Phys. A* **1993**, *57* (1), 19-24.
68. Van Attekum, P. M. T. M.; Woerlee, P. H.; Verkade, G. C.; Hoebe, A. A. M., Influence of grain-boundaries and surface debye temperature on the electrical-resistance of thin gold-films. *Phys. Rev. B* **1984**, *29* (2), 645-650.
69. Valkonen, E.; Karlsson, B.; Ribbing, C. G., Solar optical-properties of thin-films of Cu, Ag, Au, Cr, Fe, Co, Ni and Al. *Sol. Energy* **1984**, *32* (2), 211-222.
70. Granqvist, C. G., Transparent conductors as solar energy materials: A panoramic review. *Sol. Energy Mater. Sol. Cells* **2007**, *91* (17), 1529-1598.

71. Gao, H. W.; Henzie, J.; Odom, T. W., Direct evidence for surface plasmon-mediated enhanced light transmission through metallic nanohole arrays. *Nano Lett.* **2006**, 6 (9), 2104-2108.
72. Xu, H.; Hong, R.; Wang, X. Y.; Arvizo, R.; You, C. C.; Samanta, B.; Patra, D.; Tuominen, M. T.; Rotello, V. M., Controlled formation of patterned gold films via site-selective deposition of nanoparticles onto polymer-templated surfaces. *Adv. Mater.* **2007**, 19 (10), 1383-1386.
73. Granqvist, C. G., *Materials science for solar energy conversion systems*. 1st ed.; Pergamon: Oxford [England] ; New York, 1991; p 106-167.
74. Sahu, D. R.; Lin, S. Y.; Huang, J. L., ZnO/Ag/ZnO multilayer films for the application of a very low resistance transparent electrode. *Appl. Surf. Sci.* **2006**, 252 (20), 7509-7514.
75. Nath, P.; Bunshah, R. F.; Basol, B. M.; Staffsud, O. M., Electrical and Optical-Properties of In₂O₃-Sn Films Prepared by Activated Reactive Evaporation. *Thin Solid Films* **1980**, 72 (3), 463-468.
76. Igasaki, Y.; Saito, H., Substrate-temperature dependence of electrical-properties of ZnO-Al epitaxial-films on sapphire (1210). *J. Appl. Phys.* **1991**, 69 (4), 2190-2195.
77. Randhawa, H. S.; Matthews, M. D.; Bunshah, R. F., SnO₂ films prepared by activated reactive evaporation. *Thin Solid Films* **1981**, 83 (2), 267-271.
78. Nanto, H.; Minami, T.; Shooji, S.; Takata, S., Electrical and optical-properties of zinc-oxide thin-films prepared by Rf magnetron sputtering for transparent electrode applications. *J. Appl. Phys.* **1984**, 55 (4), 1029-1034.
79. Wong, F. L.; Fung, M. K.; Tong, S. W.; Lee, C. S.; Lee, S. T., Flexible organic light-emitting device based on magnetron sputtered indium-tin-oxide on plastic substrate. *Thin Solid Films* **2004**, 466 (1-2), 225-230.
80. Hoshi, Y.; Kiyomura, T., ITO thin films deposited at low temperatures using a kinetic energy controlled sputter-deposition technique. *Thin Solid Films* **2002**, 411 (1), 36-41.
81. Lan, Y. F.; Peng, W. C.; Lo, Y. H.; He, J. L., Indium tin oxide films deposited by thermionic-enhanced DC magnetron sputtering on unheated polyethylene terephthalate polymer substrate. *Mater. Res. Bull.* **2009**, 44 (8), 1760-1764.
82. Gordon, R. G., Criteria for choosing transparent conductors. *MRS Bull.* **2000**, 25 (8), 52-57.

83. Fallah, H. R.; Ghasemi, M.; Hassanzadeh, A.; Steki, H., The effect of annealing on structural, electrical and optical properties of nanostructured ITO films prepared by e-beam evaporation. *Mater. Res. Bull.* **2007**, 42 (3), 487-496.
84. Boehme, M.; Charton, C., Properties of ITO on PET film in dependence on the coating conditions and thermal processing. *Surf. Coat. Technol.* **2005**, 200 (1-4), 932-935.
85. Park, S. K.; Han, J. I.; Moon, D. G.; Kim, W. K., Mechanical stability of externally deformed indium-tin-oxide films on polymer substrates. *Jpn. J. Appl. Phys., Part 1* **2003**, 42 (2A), 623-629.
86. Chiang, C. K.; Fincher, C. R.; Park, Y. W.; Heeger, A. J.; Shirakawa, H.; Louis, E. J.; Gau, S. C.; MacDiarmid, A. G., Electrical conductivity in doped polyacetylene. *Phys. Rev. Lett.* **1977**, 39 (17), 1098.
87. Heeger, A. J., Semiconducting and metallic polymers: The fourth generation of polymeric materials (Nobel lecture). *Angew. Chem. Int. Ed.* **2001**, 40 (14), 2591-2611.
88. DeLongchamp, D. M.; Hammond, P. T., High-contrast electrochromism and controllable dissolution of assembled Prussian blue/polymer nanocomposites. *Adv. Funct. Mater.* **2004**, 14 (3), 224-232.
89. Choulis, S. A.; Choong, V. E.; Mathai, M. K.; So, F., The effect of interfacial layer on the performance of organic light-emitting diodes. *Appl. Phys. Lett.* **2005**, 87 (11), 113503
90. Mabeck, J. T.; DeFranco, J. A.; Bernards, D. A.; Malliaras, G. G.; Hocde, S.; Chase, C. J., Microfluidic gating of an organic electrochemical transistor. *Appl. Phys. Lett.* **2005**, 87 (1), 013503.
91. Chen, P. C.; Shen, G.; Sukcharoenchoke, S.; Zhou, C., Flexible and transparent supercapacitor based on In_2O_3 nanowire/carbon nanotube heterogeneous films. *Appl. Phys. Lett.* **2009**, 94 (4), 043113.
92. Mo, C. B.; Hwang, J. W.; Cha, S. I.; Hong, S. H., Multi-walled carbon nanotube/Co composite field emitters fabricated by in situ spray coating. *Carbon* **2009**, 47 (5), 1276-1281.
93. Tseng, A., *Nanofabrication: Fundamentals and applications*. World Scientific Publishing Co.: Singapore; Hackensack, 2008.
94. Blodgett, K. B., Monomolecular films of fatty acids on glass. *J. Am. Chem. Soc.* **1934**, 56, 495-495.

95. Decher, G., Fuzzy nanoassemblies: Toward layered polymeric multicomposites. *Science* **1997**, 277 (5330), 1232-1237.
96. Keller, S. W.; Kim, H.-N.; Mallouk, T. E., Layer-by-layer assembly of intercalation compounds and heterostructures on surfaces: Toward molecular "beaker" epitaxy. *J. Am. Chem. Soc.* **1994**, 116 (19), 8817-8818.
97. Hatzor, A.; Moav, T.; Cohen, H.; Matlis, S.; Libman, J.; Vaskevich, A.; Shanzer, A.; Rubinstein, I., Coordination-controlled self-assembled multilayers on gold. *J. Am. Chem. Soc.* **1998**, 120 (51), 13469-13477.
98. Yang, S. Y.; Rubner, M. F., Micropatterning of polymer thin films with pH-sensitive and cross-linkable hydrogen-bonded polyelectrolyte multilayers. *J. Am. Chem. Soc.* **2002**, 124 (10), 2100-2101.
99. Sukhishvili, S. A.; Granick, S., Layered, erasable polymer multilayers formed by hydrogen-bonded sequential self-assembly. *Macromolecules* **2001**, 35 (1), 301-310.
100. Tang, T.; Qu, J.; Müllen, K.; Webber, S. E., Molecular layer-by-layer self-assembly of water-soluble perylene diimides through π - π and electrostatic interactions. *Langmuir* **2005**, 22 (1), 26-28.
101. Ariga, K.; Lvov, Y.; Kunitake, T., Assembling alternate dye-polyion molecular films by electrostatic layer-by-layer adsorption. *J. Am. Chem. Soc.* **1997**, 119 (9), 2224-2231.
102. Inoue, H.; Anzai, J.-i., Stimuli-sensitive thin films prepared by a layer-by-layer deposition of 2-iminobiotin-labeled poly(ethyleneimine) and avidin. *Langmuir* **2005**, 21 (18), 8354-8359.
103. Rauf, S.; Zhou, D.; Abell, C.; Klenerman, D.; Kang, D.-J., Building three-dimensional nanostructures with active enzymes by surface templated layer-by-layer assembly. *Chem. Commun.* **2006**, (16), 1721-1723.
104. Shimazaki, Y.; Nakamura, R.; Ito, S.; Yamamoto, M., Molecular weight dependence of alternate adsorption through charge-transfer interaction. *Langmuir* **2000**, 17 (3), 953-956.
105. Lee, S.-W.; Ichinose, I.; Kunitake, T., Molecular imprinting of azobenzene carboxylic acid on a TiO₂ ultrathin film by the surface sol-gel process. *Langmuir* **1998**, 14 (10), 2857-2863.
106. Gamboa, D.; Priolo, M. A.; Ham, A.; Grunlan, J. C., Note: Influence of rinsing and drying routines on growth of multilayer thin films using automated deposition system. *Rev. Sci. Instrum.* **2010**, 81 (3), 036103.

107. Ma, H.; Zhang, L.; Pan, Y.; Zhang, K.; Zhang, Y., A novel electrochemical DNA biosensor fabricated with layer-by-layer covalent attachment of multiwalled carbon nanotubes and gold nanoparticles. *Electroanalysis* **2008**, *20* (11), 1220-1226.
108. Seo, H. S.; Kim, S. E.; Park, J. S.; Lee, J. H.; Yang, K. Y.; Lee, H.; Lee, K. E.; Han, S. S.; Lee, J., A three-dimensional nanostructured array of protein nanoparticles. *Adv. Funct. Mater.* **2010**, *20* (23), 4055-4061.
109. Park, J.; Fouché, L.; Hammond, P., Multicomponent patterning of layer-by-layer assembled polyelectrolyte/nanoparticle composite thin films with controlled alignment. *Adv. Mater.* **2005**, *17* (21), 2575-2579.
110. Koo, H.; Yi, D.; Yoo, S.; Kim, D. Y., A snowman-like array of colloidal dimers for antireflecting surfaces. *Adv. Mater.* **2004**, *16* (3), 274-277.
111. Park, Y. T.; Grunlan, J. C., Fast switching electrochromism from colloidal indium tin oxide in tungstate-based thin film assemblies. *Electrochim. Acta* **2010**, *55* (9), 3257-3267.
112. Li, Y.-C.; Schulz, J.; Mannen, S.; Delhom, C.; Condon, B.; Chang, S.; Zammarano, M.; Grunlan, J. C., Flame retardant behavior of polyelectrolyte-clay thin film assemblies on cotton fabric. *ACS Nano* **2010**, *4* (6), 3325-3337.
113. Hendricks, T. R.; Lu, J.; Drzal, L. T.; Lee, I., Intact pattern transfer of conductive exfoliated graphite nanoplatelet composite films to polyelectrolyte multilayer platforms. *Adv. Mater.* **2008**, *20* (10), 2008-2012.
114. Osada, M.; Ebina, Y.; Funakubo, H.; Yokoyama, S.; Kiguchi, T.; Takada, K.; Sasaki, T., High- κ dielectric nanofilms fabricated from titania nanosheets. *Adv. Mater.* **2006**, *18* (8), 1023-1027.
115. Park, Y. T.; Ham, A. Y.; Grunlan, J. C., High electrical conductivity and transparency in deoxycholate-stabilized carbon nanotube thin films. *J. Phys. Chem. C* **2010**, *114* (14), 6325-6333.
116. Mamedov, A. A.; Belov, A.; Giersig, M.; Mamedova, N. N.; Kotov, N. A., Nanorainbows: Graded semiconductor films from quantum dots. *J. Am. Chem. Soc.* **2001**, *123* (31), 7738-7739.
117. Wang, D.; Rogach, A. L.; Caruso, F., Semiconductor quantum dot-labeled microsphere bioconjugates prepared by stepwise self-assembly. *Nano Lett.* **2002**, *2* (8), 857-861.
118. Park, J.; Hammond, P., Multilayer transfer printing for polyelectrolyte multilayer patterning: Direct transfer of layer-by-layer assembled micropatterned thin films. *Adv. Mater.* **2004**, *16* (6), 520-525.

119. Agarwal, M.; Lvov, Y.; Varahramyan, K., Conductive wood microfibres for smart paper through layer-by-layer nanocoating. *Nanotechnology* **2006**, *17* (21), 5319-5325.
120. Caruso, F.; Caruso, R. A.; ouml; hwald, H., Nanoengineering of inorganic and hybrid hollow spheres by colloidal templating. *Science* **1998**, 282 (5391), 1111-1114.
121. Liang, Z.; Susha, A.; Yu, A.; Caruso, F., Nanotubes prepared by layer-by-layer coating of porous membrane templates. *Adv. Mater.* **2003**, *15* (21), 1849-1853.
122. Dubas, S. T.; Schlenoff, J. B., Factors controlling the growth of polyelectrolyte multilayers. *Macromolecules* **1999**, *32* (24), 8153-8160.
123. Shinbo, K.; Suzuki, K.; Kato, K.; Kaneko, F.; Kobayashi, S., Thermally stimulated currents and electrical conduction in self-assembled ultrathin films. *Thin Solid Films* **1998**, 327-329, 209-213.
124. Yoo, D.; Shiratori, S. S.; Rubner, M. F., Controlling bilayer composition and surface wettability of sequentially adsorbed multilayers of weak polyelectrolytes. *Macromolecules* **1998**, *31* (13), 4309-4318.
125. Yang, Y.-H.; Malek, F. A.; Grunlan, J. C., Influence of deposition time on layer-by-layer growth of clay-based thin films. *Ind. Eng. Chem. Res.* **2010**, *49* (18), 8501-8509.
126. Podsiadlo, P.; Michel, M.; Lee, J.; Verploegen, E.; Wong Shi Kam, N.; Ball, V.; Lee, J.; Qi, Y.; Hart, A. J.; Hammond, P. T.; Kotov, N. A., Exponential growth of LbL films with incorporated inorganic sheets. *Nano Lett.* **2008**, *8* (6), 1762-1770.
127. Kolarik, L.; Furlong, D. N.; Joy, H.; Struijk, C.; Rowe, R., Building assemblies from high molecular weight polyelectrolytes. *Langmuir* **1999**, *15* (23), 8265-8275.
128. Hong, H.; Steitz, R.; Kirstein, S.; Davidov, D., Superlattice structures in poly(phenylenevinylene)-based self-assembled films. *Adv. Mater.* **1998**, *10* (14), 1104-1108.
129. Laschewsky, A.; Wischerhoff, E.; Kauranen, M.; Persoons, A., Polyelectrolyte multilayer assemblies containing nonlinear optical dyes. *Macromolecules* **1997**, *30* (26), 8304-8309.
130. Nolte, A. J.; Treat, N. D.; Cohen, R. E.; Rubner, M. F., Effect of relative humidity on the Young's modulus of polyelectrolyte multilayer films and related nonionic polymers. *Macromolecules* **2008**, *41* (15), 5793-5798.

131. Tan, H. L.; McMurdo, M. J.; Pan, G.; Van Patten, P. G., Temperature dependence of polyelectrolyte multilayer assembly. *Langmuir* **2003**, *19* (22), 9311-9314.
132. Chang, L.; Kong, X.; Wang, F.; Wang, L.; Shen, J., Layer-by-layer assembly of poly (N-acryloyl-N'-propylpiperazine) and poly (acrylic acid): Effect of pH and temperature. *Thin Solid Films* **2008**, *516* (8), 2125-2129.
133. Kohli, P.; Blanchard, G. J., Design and growth of robust layered polymer assemblies with molecular thickness control. *Langmuir* **1999**, *15* (4), 1418-1422.
134. Laschewsky, A.; Wischerhoff, E.; Denzinger, S.; Ringsdorf, H.; Delcorte, A.; Bertrand, P., Molecular recognition by hydrogen bonding in polyelectrolyte multilayers. *Chem. Eur. J.* **1997**, *3* (1), 34-38.
135. Lee, D.; Rubner, M. F.; Cohen, R. E., All-nanoparticle thin-film coatings. *Nano Lett.* **2006**, *6* (10), 2305-2312.
136. Lee, D.; Gemici, Z.; Rubner, M. F.; Cohen, R. E., Multilayers of oppositely charged SiO₂ nanoparticles: Effect of surface charge on multilayer assembly. *Langmuir* **2007**, *23* (17), 8833-8837.
137. Shim, B. S.; Zhu, J.; Jan, E.; Critchley, K.; Kotov, N. A., Transparent conductors from layer-by-layer assembled SWNT films: Importance of mechanical properties and a new figure of merit. *ACS Nano* **2010**, *4* (7), 3725-3734.
138. Wenseleers, W.; Vlasov, I. I.; Goovaerts, E.; Obraztsova, E. D.; Lobach, A. S.; Bouwen, A., Efficient isolation and solubilization of pristine single-walled nanotubes in bile salt micelles. *Adv. Funct. Mater.* **2004**, *14* (11), 1105-1112.
139. Haggemueller, R.; Rahatekar, S. S.; Fagan, J. A.; Chun, J. H.; Becker, M. L.; Naik, R. R.; Krauss, T.; Carlson, L.; Kadla, J. F.; Trulove, P. C.; Fox, D. F.; DeLong, H. C.; Fang, Z. C.; Kelley, S. O.; Gilman, J. W., Comparison of the quality of aqueous dispersions of single wall carbon nanotubes using surfactants and biomolecules. *Langmuir* **2008**, *24* (9), 5070-5078.
140. Bain, C. D.; Evall, J.; Whitesides, G. M., Formation of monolayers by the coadsorption of thiols on gold - variation in the head group, tail group, and solvent. *J. Am. Chem. Soc.* **1989**, *111* (18), 7155-7164.
141. Kern, W., The evolution of silicon-wafer cleaning technology. *J. Electrochem. Soc.* **1990**, *137* (6), 1887-1892.
142. Owens, D. K., The mechanism of corona and ultraviolet light-induced self-adhesion of poly(ethylene terephthalate) film. *J. Appl. Polym. Sci.* **1975**, *19*, 3315-3326.

143. Smits, F. M., Measurement of sheet resistivities with the four-point probe. *Bell Labs Tech. J.* **1958**, 37, 711-719.
144. Futaba, D. N.; Hata, K.; Yamada, T.; Hiraoka, T.; Hayamizu, Y.; Kakudate, Y.; Tanaike, O.; Hatori, H.; Yumura, M.; Iijima, S., Shape-engineerable and highly densely packed single-walled carbon nanotubes and their application as super-capacitor electrodes. *Nat. Mater.* **2006**, 5 (12), 987-994.
145. Kirkpatrick, S., Percolation and conduction. *Rev. Mod. Phys.* **1973**, 45 (4), 574-588.
146. Grunlan, J. C.; Mehrabi, A. R.; Bannon, M. V.; Bahr, J. L., Water-based single-walled-nanotube-filled polymer composite with an exceptionally low percolation threshold. *Adv. Mater.* **2004**, 16 (2), 150-153.
147. Ramasubramaniam, R.; Chen, J.; Liu, H. Y., Homogeneous carbon nanotube/polymer composites for electrical applications. *Appl. Phys. Lett.* **2003**, 83 (14), 2928-2930.
148. Liu, J.; Rinzler, A. G.; Dai, H. J.; Hafner, J. H.; Bradley, R. K.; Boul, P. J.; Lu, A.; Iverson, T.; Shelimov, K.; Huffman, C. B.; Rodriguez-Macias, F.; Shon, Y. S.; Lee, T. R.; Colbert, D. T.; Smalley, R. E., Fullerene pipes. *Science* **1998**, 280 (5367), 1253-1256.
149. Koshio, A.; Yudasaka, M.; Iijima, S., Thermal degradation of ragged single-wall carbon nanotubes produced by polymer-assisted ultrasonication. *Chem. Phys. Lett.* **2001**, 341 (5-6), 461-466.
150. Furtado, C. A.; Kim, U. J.; Gutierrez, H. R.; Pan, L.; Dickey, E. C.; Eklund, P. C., Debundling and dissolution of single-walled carbon nanotubes in amide solvents. *J. Am. Chem. Soc.* **2004**, 126 (19), 6095-6105.
151. Tran, M. Q.; Tridech, C.; Alfrey, A.; Bismarck, A.; Shaffer, M. S. P., Thermal oxidative cutting of multi-walled carbon nanotubes. *Carbon* **2007**, 45 (12), 2341-2350.
152. Simmons, T. J.; Bult, J.; Hashim, D. P.; Linhardt, R. J.; Ajayan, P. M., Noncovalent functionalization as an alternative to oxidative acid treatment of single wall carbon nanotubes with applications for polymer composites. *ACS Nano* **2009**, 3 (4), 865-870.
153. Park, Y. T.; Ham, A. Y.; Grunlan, J. C., Heating and acid doping thin film carbon nanotube assemblies for high transparency and low sheet resistance. *J. Mater. Chem.* **2011**, 21 (2), 363-368.
154. Ingle, J. D. J.; Crouch, S. R., *Spectrochemical analysis*. Prentice Hall: New Jersey, 1988.

155. Ericson, L. M.; Fan, H.; Peng, H. Q.; Davis, V. A.; Zhou, W.; Sulpizio, J.; Wang, Y. H.; Booker, R.; Vavro, J.; Guthy, C.; Parra-Vasquez, A. N. G.; Kim, M. J.; Ramesh, S.; Saini, R. K.; Kittrell, C.; Lavin, G.; Schmidt, H.; Adams, W. W.; Billups, W. E.; Pasquali, M.; Hwang, W. F.; Hauge, R. H.; Fischer, J. E.; Smalley, R. E., Macroscopic, neat, single-walled carbon nanotube fibers. *Science* **2004**, *305* (5689), 1447-1450.
156. Zhou, W.; Vavro, J.; Nemes, N. M.; Fischer, J. E.; Borondics, F.; Kamars, K.; Tanner, D. B., Charge transfer and Fermi level shift in p -doped single-walled carbon nanotubes. *Phys. Rev. B: Condens. Matter* **2005**, *71* (20), 205423.
157. Geng, H.-Z.; Kim, K. K.; Song, C.; Xuyen, N. T.; Kim, S. M.; Park, K. A.; Lee, D. S.; An, K. H.; Lee, Y. S.; Chang, Y.; Lee, Y. J.; Choi, J. Y.; Benayad, A.; Lee, Y. H., Doping and de-doping of carbon nanotube transparent conducting films by dispersant and chemical treatment. *J. Mater. Chem.* **2008**, *18* (11), 1261-1266.
158. Graupner, R.; Abraham, J.; Vencelova, A.; Seyller, T.; Hennrich, F.; Kappes, M. M.; Hirsch, A.; Ley, L., Doping of single-walled carbon nanotube bundles by Bronsted acids. *Phys. Chem. Chem. Phys.* **2003**, *5* (24), 5472-5476.
159. Zhang, X.; Sreekumar, T. V.; Liu, T.; Kumar, S., Properties and structure of nitric acid oxidized single wall carbon nanotube films. *J. Phys. Chem. B* **2004**, *108* (42), 16435-16440.
160. Wang, R.; Sun, J.; Gao, L.; Zhang, J., Base and acid treatment of SWCNT-RNA transparent conductive films. *ACS Nano* **2010**, *4* (8), 4890-4896.
161. Dettlaff-Weglikowska, U.; Skákalová, V.; Graupner, R.; Jhang, S. H.; Kim, B. H.; Lee, H. J.; Ley, L.; Park, Y. W.; Berber, S.; Tománek, D.; Roth, S., Effect of SOCl₂ treatment on electrical and mechanical properties of single-wall carbon nanotube networks. *J. Am. Chem. Soc.* **2005**, *127* (14), 5125-5131.
162. Green, A. A.; Hersam, M. C., Processing and properties of highly enriched double-wall carbon nanotubes. *Nat. Nanotechnol.* **2009**, *4* (1), 64-70.
163. Shimada, T.; Sugai, T.; Ohno, Y.; Kishimoto, S.; Mizutani, T.; Yoshida, H.; Okazaki, T.; Shinohara, H., Double-wall carbon nanotube field-effect transistors: Ambipolar transport characteristics. *Appl. Phys. Lett.* **2004**, *84* (13), 2412-2414.
164. Material Safety Data Sheet: (1) Sulfuric acid, fuming (Prod.#: 435597), (2) Nitric acid, fuming (Prod.#: 78005), (3) Hydrochloric acid, fuming (Prod.#: 84418). <http://www.sigmaaldrich.com/safety-center.html> (accessed 02/21/2011).

165. Yang, D. Q.; Rochette, J. F.; Sacher, E., Spectroscopic evidence for π - π interaction between poly(diallyl dimethylammonium) chloride and multiwalled carbon nanotubes. *J. Phys. Chem. B* **2005**, *109* (10), 4481-4484.
166. Chen, H. J.; Wang, Y. L.; Wang, Y. Z.; Dong, S. J.; Wang, E. K., One-step preparation and characterization of PDDA-protected gold nanoparticles. *Polymer* **2006**, *47* (2), 763-766.
167. Senthilkumar, M.; Mathiyarasu, J.; Joseph, J.; Phani, K. L. N.; Yegnaraman, V., Electrochemical instability of indium tin oxide (ITO) glass in acidic pH range during cathodic polarization. *Mater. Chem. Phys.* **2008**, *108* (2-3), 403-407.
168. Kumar, A.; Zhou, C. W., The race to replace tin-doped indium oxide: Which material will win? *ACS Nano* **2010**, *4* (1), 11-14.
169. Cho, A., Still in its infancy, two-dimensional crystal claims prize. *Science* **2010**, *330* (6001), 159.
170. Novoselov, K. S.; Geim, A. K.; Morozov, S. V.; Jiang, D.; Zhang, Y.; Dubonos, S. V.; Grigorieva, I. V.; Firsov, A. A., Electric field effect in atomically thin carbon films. *Science* **2004**, *306* (5296), 666-669.
171. Avouris, P., Graphene: Electronic and photonic properties and devices. *Nano Lett.* **2010**, *10* (11), 4285-4294.
172. Kim, J.; Cote, L. J.; Kim, F.; Yuan, W.; Shull, K. R.; Huang, J. X., Graphene oxide sheets at interfaces. *J. Am. Chem. Soc.* **2010**, *132* (23), 8180-8186.
173. Kim, H.; Abdala, A. A.; Macosko, C. W., Graphene/polymer nanocomposites. *Macromolecules* **2010**, *43* (16), 6515-6530.
174. Wu, J. B.; Agrawal, M.; Becerril, H. A.; Bao, Z. N.; Liu, Z. F.; Chen, Y. S.; Peumans, P., Organic light-emitting diodes on solution-processed graphene transparent electrodes. *ACS Nano* **2010**, *4* (1), 43-48.
175. Kim, K. S.; Zhao, Y.; Jang, H.; Lee, S. Y.; Kim, J. M.; Kim, K. S.; Ahn, J. H.; Kim, P.; Choi, J. Y.; Hong, B. H., Large-scale pattern growth of graphene films for stretchable transparent electrodes. *Nature* **2009**, *457* (7230), 706-710.
176. King, P. J.; Khan, U.; Lotya, M.; De, S.; Coleman, J. N., Improvement of transparent conducting nanotube films by addition of small quantities of graphene. *ACS Nano* **2010**, *4* (7), 4238-4246.
177. Zhao, J. P.; Pei, S. F.; Ren, W. C.; Gao, L. B.; Cheng, H. M., Efficient preparation of large-area graphene oxide sheets for transparent conductive films. *ACS Nano* **2010**, *4* (9), 5245-5252.

178. Zhao, X.; Zhang, Q. H.; Hao, Y. P.; Li, Y. Z.; Fang, Y.; Chen, D. J., Alternate multilayer films of poly(vinyl alcohol) and exfoliated graphene oxide fabricated via a facial layer-by-layer assembly. *Macromolecules* **2010**, *43* (22), 9411-9416.
179. Kulkarni, D. D.; Choi, I.; Singamaneni, S.; Tsukruk, V. V., Graphene oxide-polyelectrolyte nanomembranes. *ACS Nano* **2010**, *4* (8), 4667-4676.
180. Yao, H. B.; Wu, L. H.; Cui, C. H.; Fang, H. Y.; Yu, S. H., Direct fabrication of photoconductive patterns on LBL assembled graphene oxide/PDDA/titania hybrid films by photothermal and photocatalytic reduction. *J. Mater. Chem.* **2010**, *20* (25), 5190-5195.
181. Chen, D.; Wang, X. Y.; Liu, T. X.; Wang, X. D.; Li, J., Electrically conductive poly(vinyl alcohol) hybrid films containing graphene and layered double hydroxide fabricated via layer-by-layer self-assembly. *ACS Appl. Mater. Interfaces* **2010**, *2* (7), 2005-2011.
182. Hong, T. K.; Lee, D. W.; Choi, H. J.; Shin, H. S.; Kim, B. S., Transparent, flexible conducting hybrid multilayer thin films of multiwalled carbon nanotubes with graphene nanosheets. *ACS Nano* **2010**, *4* (7), 3861-3868.
183. He, Q. Y.; Sudibya, H. G.; Yin, Z. Y.; Wu, S. X.; Li, H.; Boey, F.; Huang, W.; Chen, P.; Zhang, H., Centimeter-long and large-scale micropatterns of reduced graphene oxide films: Fabrication and sensing applications. *ACS Nano* **2010**, *4* (6), 3201-3208.
184. Opatkiewicz, J.; LeMieux, M. C.; Bao, Z. N., Nanotubes on display: How carbon nanotubes can be integrated into electronic displays. *ACS Nano* **2010**, *4* (6), 2975-2978.
185. Wager, J. F., Transparent electronics. *Science* **2003**, *300* (5623), 1245-1246.
186. Kumar, B.; Park, Y. T.; Grunlan, J. C.; Feller, J. F., Transparent polymer-carbon nanotube layer-by-layer assemblies for polar vapor sensing. **2011**, to be submitted.

APPENDIX A
FAST SWITCHING ELECTROCHROMISM FROM COLLOIDAL
INDIUM TIN OXIDE IN TUNGSTATE-BASED
THIN FILM ASSEMBLIES*

A.1 Introduction

As the name suggests, electrochromism involves a color change with the application of an electrical potential. In many cases, electrochromism is reversible upon application of the electrical potential in reverse direction and, in most cases, occurs by reduction-oxidation (redox) reactions.¹⁻⁴ Non-redox electrochromism is also possible for some polarizable molecules that exhibit a spectroscopic shift with the application of a strong electric field, known as the Stark effect.^{5,6} Devices that make use of electrochromic technology include smart windows,^{7,8} helmet visors,^{9,10} electrochromic mirrors,^{11,12} and displays.^{13,14} Especially for windows and displays, it is desirable for the electrochromic species to exhibit high contrast (i.e., large transmittance difference between colorless and colored states) and fast switching speed between states. Inorganic oxides are known to exhibit good contrast, but they typically require more than 60 seconds to switch states.¹⁵ The present study focuses on improving the switching speed of tungstate (WO_4^{2-}) by depositing it as a thin film with a polycation and electrically conductive indium tin oxide (ITO) nanoparticles.

Tungsten oxide has been studied for decades because of its unique electrochemical and electrochromic properties.¹⁶⁻¹⁸ The driving force of color change in tungsten oxide (WO_3 or WO_4^{2-}) is a chemically reversible interaction with electrons and

* Reprinted with permission from “Fast switching electrochromism from colloidal indium tin oxide in tungstate-based thin film assemblies” by Yong Tae Park and Jaime C. Grunlan, *Electrochim. Acta* **2010**, 55, 3257–3267. ©2010 Elsevier Ltd.

cations, such as H^+ or Li^+ , during coloration and bleaching.^{11,19} In tungstate electrochromism, fully reversible redox coloration is generated by polarization at the cathode, where electrons penetrate into the oxide. At the same time, cations migrate toward anionic WO_4^{2-} to generate M_xWO_4 ($M = H, Li$ or Na), tinting the film a deep blue. In crystalline WO_3 films, the optical properties are based on ionized impurity scattering of free electrons.²⁰ Uncertainty remains about the coloration mechanism of amorphous WO_3 films, although it is widely accepted that the color change depends on the $W^{6+} \leftrightarrow W^{5+}$ redox reaction.²¹ In the oxidized state (W^{6+}), WO_3 is light yellow, while it is blue in the reduced state (W^{5+}). Several methods for preparation of WO_3 thin films have been introduced since the first report of WO_3 as an electrochromic material including thermal evaporation,²² chemical vapor deposition,²³ sputtering,²⁴ electrodeposition,²⁵ sol-gel by spin coating,²⁶ dip-coating,²⁷ and spray pyrolysis.²⁸ A technique known as layer-by-layer (LbL) is studied here as a means of tailoring the contrast and switching speed of tungstate-based thin films.

The LbL method produces thin films by harnessing electrostatic interactions through alternately exposing a substrate to positively and negatively-charged aqueous solutions.^{29,30} Each positive and negative pair deposited is referred to as a bilayer (BL). This cycle is repeated to add the desired number of BLs. A variety of functional thin films have been produced using the LbL technique, including antimicrobials,^{31,32} gas barriers,^{33,34} sensors,^{35,36} membranes for fuel cells,³⁷⁻³⁹ drug delivery,⁴⁰⁻⁴² field-effect transistors,^{43,44} and electrically conductive coatings.^{45,46} Additionally, many electrochromic thin films have been prepared using the LbL method with poly(3,4-ethylenedioxythiophene),⁴⁷ Ruthenium Purple,⁴⁸ Prussian Blue,⁴⁹ poly(aniline-N-

butylsulfonate)s,⁵⁰ and viologen.⁵¹ The tungstate anion goes through an analogous color change to WO_3 and can be deposited using LbL methodology.

In this study, electrochromic thin film assemblies were prepared using WO_4^{2-} alternated with poly(4-vinylpyridine-*co*-styrene) (PVP-S) and/or poly(diallyldimethyl ammonium chloride) (PDDA). Although other methods for making tungsten oxide electrochromic thin films have been previously reported,²²⁻²⁸ LbL assembly allows for film composition to be tailored throughout the thickness at the nanometer level. **Figure A.1** highlights the three different recipes studied here in an effort to improve contrast ratio of WO_4^{2-} based thin films and increase switching speed. Addition of colloidal ITO to selected layers (**Figure A.1(c)**) dramatically reduces switching time (from over 60 down to 14 seconds) and stabilizes contrast over several switching cycles.

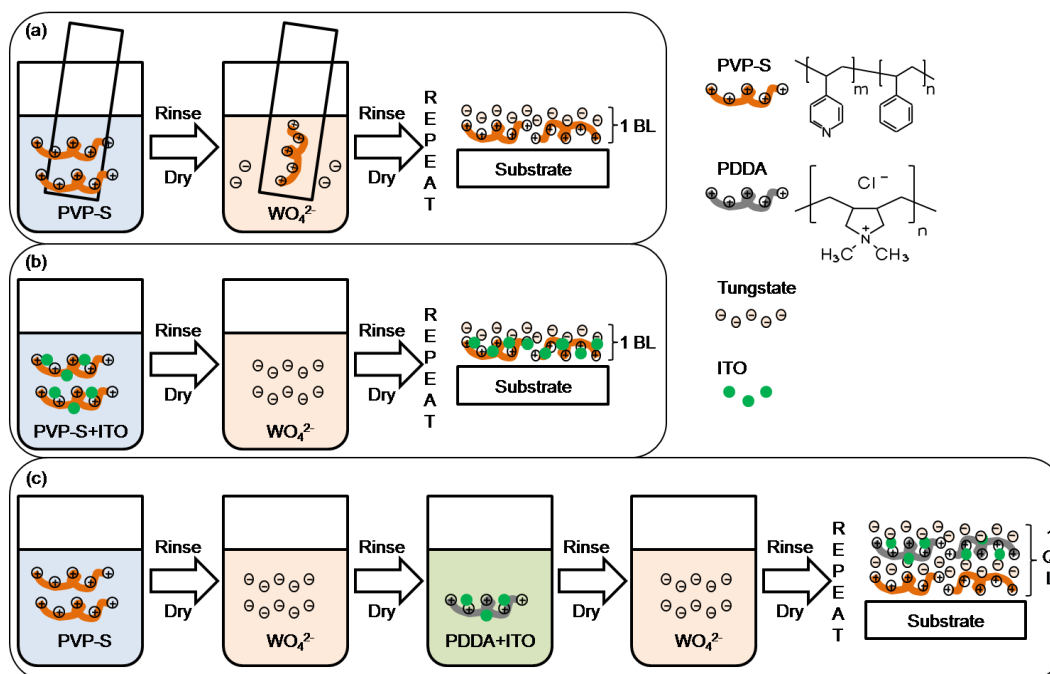


Figure A.1. Schematic of the LbL process. The three recipes studied here are each represented by their own schematic: (a) PVP-S/ WO_4^{2-} , (b) (PVP-S+ITO)/ WO_4^{2-} , and (c) PVP-S/ WO_4^{2-} /(PDDA+ITO)/ WO_4^{2-} quad-layer (QL).

A.2 Experimental

A.2.1 Materials

PVP-S (4-vinylpyridine:styrene, 9:1 mole fraction) with a molecular weight of 100 000 g/mol, PDDA with a molecular weight of 100 000–200 000 g/mol, sodium tungstate dihydrate ($\text{Na}_2\text{WO}_4 \cdot 2\text{H}_2\text{O}$, 99.995%), and lithium chloride (LiCl , 99%) were purchased from Aldrich (Milwaukee, WI). Colloidal ITO (99.5%, $\text{In}_2\text{O}_3 \cdot \text{SnO}_2$ 90:10 wt%) with a particle size of 17–28 nm was purchased from Alfa Aesar (Ward Hill, MA). Dichloromethane (99.9%), methanol (99.8%), acetone (99.5%), hydrochloric acid (HCl , 37%) were used as received from Aldrich. A 0.25 wt% PVP-S cationic aqueous solution was prepared by dissolving in 18.2 M Ω deionized water. The anionic solution was prepared by dissolving 1 wt% tungstate in deionized water. Where noted, 0.2 wt% ITO added 0.2 wt% PVP-S aqueous solution was used as cationic mixture instead of only 0.25 wt% PVP-S. A 0.02 wt% PDDA aqueous solution containing 1 wt% ITO was used as the second cationic mixture for quad-layer (QL) films. An aqueous 0.1M LiCl solution was used as the electrolyte for electrochromic measurements. All solutions were adjusted to pH 2.5 using 1M HCl . ITO-glass slides ($2.5 \text{ cm} \times 7.5 \text{ cm}$, 4–10 Ω/sq , Delta Technologies, Stillwater, MN) were cleaned by bath ultrasonication in a series of solvents: dichloromethane, methanol, acetone, and deionized water for 15 min each, followed by a 5 min oxygen plasma etch with a Harrick PDC 32G (Harrick Plasma, Ithaca, NY).⁵² Fused quartz glass slides (Structure Probe Inc., West Chester, PA) were prepared using a piranha treatment by immersing slides into a piranha solution after ultrasonication for 30 min, followed by thoroughly rinsing with deionized water and drying with filtered air.⁵³ Single side polished (1 0 0) silicon wafers (University Wafer, South Boston, MA) were

cut to size, rinsed with ethanol-acetone (1:1), followed by deionized water, and finally dried with filtered air.⁵⁴ Polystyrene (PS) film (tradename ST311125 by Goodfellow Cambridge Ltd., Cambridge, UK) substrates were cut to size, followed by rinsing with methanol, then deionized water, and drying with filtered air. The cleaned polymer substrates were then corona treated with a BD-20C Corona Treater (Electro-Technic Products Inc., Chicago, IL). Corona treatment is used to oxidize the surface of the polymers, which aids adhesion of deposited layers.⁵⁵

A.2.2 Layer-by-Layer Assembly

PVP-S/ WO_4^{2-} assemblies were built according to the procedure shown in **Figure A.1**. Clean substrates were first immersed in a 0.25 wt% aqueous PVP-S solution for 5 min, followed by rinsing with deionized water and drying with filtered air. Immersion into the 1.0 wt% WO_4^{2-} aqueous solution for 5 min came next, followed by rinsing and drying. These four steps are one cycle, yielding one bilayer. For each subsequent cycle, the immersion time for both solutions was reduced to one minute and repeated to deposit the desired number of BLs. Quad-layers required two more deposition steps for each full QL. Immersion into a (0.02 wt% PDDA+1 wt% ITO) aqueous solution for 5 min with rinsing and drying was followed by immersion into the 1.0 wt% WO_4^{2-} aqueous solution for 1 min with rinsing and drying. Immersion time for all solutions was reduced to one minute beginning with the second cycle. Following deposition, all films were stored in a dry box for a minimum of 12 hours prior to testing.

A.2.3 Characterization of Film Growth

Thickness measurements were performed with an ellipsometer and/or a profilometer on silicon wafers and glass slides, respectively. A PHE-101 Discrete Wavelength Ellipsometer (Microphonics, Allentown, PA) was used at a wavelength of 632.8 nm and an angle of 65°. Thicker films were analyzed with a Dektak 3 Stylus Profilometer (Neutronix-Quintel, Morgan Hill, CA) on fused quartz glass slides. A 12.5 μm stylus tip and 50 mg force were used to avoid damaging the film. An F20 reflectometer (Filmetrics Inc., San Diego, CA) was also used to confirm the thickness with the refractive index acquired from ellipsometry. Weight of each deposited layer was measured with a Maxtek (East Syracuse, NY) research quartz crystal microbalance (QCM) and 5 MHz gold-electrode quartz crystals. The quartz crystals were cleaned with an oxygen plasma etcher. Absorbance and transmittance of deposited films were measured between 250 and 850 nm with a USB2000 UV-Vis spectrometer (Ocean Optics, Dunedin, FL). To measure light absorbance of PVP-S films, PVP-S thin films were deposited on quartz slides with a WS-650 spin coater (Laurell Technologies, North Wales, PA) at 3500 rpm.

A.2.4 Imaging

Thin film cross sections were imaged with a JEOL 1200 EX TEM (JEOL USA Inc., Peabody, MA) with an operating voltage of 100 kV. For TEM specimens, the films on PS substrates were embedded in epoxy resin comprised of Araldite 502 modified bisphenol A and Quetol 651 ethylene glycol diglycidyl ether along with dodecenyl succinic anhydride hardener and benzyldimethylamine accelerator, which were purchased

from Electron Microscopy Sciences (Hatfield, PA). The specimens were sectioned down to 90 nm with a Reichert-Jung Ultracut E 7017014 and placed on nickel grids to dry prior to imaging. Atomic force microscope (AFM) images were obtained with a Nanosurf easyScan 2 (Nanoscience Instruments, Inc., Phoenix, AZ) in dynamic mode with an ACL-A cantilever tip.

A.2.5 Electrochemical Measurements

An Epsilon 851 cyclic voltammeter (BASi Instrumentation, West Lafayette, IN) was used for electrochemical characterization. ITO-coated glass slides were used as the working electrode, a platinum wire (0.35 mm diameter from BASi Instrumentation) as the counter electrode, and AgCl/Ag (3M KCl) as the reference electrode. These measurements were performed with a 4 cm² working electrode at ambient temperature (22±2 °C) in an aqueous 0.1M LiCl solution (pH = 2.5) that had been bubbled with N₂ gas for more than 20 minutes prior to measurement. Cyclic voltammetry was performed between two potential limits at scan rates of 25, 50, 100, and 200 mV/s. Electrochromic characterization was done in-situ with UV-Vis measurements in conjunction with changes in electrical potential. Absorbance was measured with the same UV-Vis spectrometer and potential control was provided by an E3646A Agilent power supply (Santa Clara, CA). The films deposited on ITO glass slides were immersed in 0.1M LiCl electrolyte, along with platinum foil (99.99%, 0.127 mm thickness from Aldrich) as a counter electrode.

A.3 Results and Discussion

A.3.1 Growth of Tungstate Assemblies

Film growth of the PVP-S/ WO_4^{2-} assembly onto a Si wafer was analyzed using ellipsometry, as shown in **Figure A.2**. The PVP-S/ WO_4^{2-} system increases linearly in thickness, by approximately 2.0 nm per BL, using a fixed refractive index of 1.65. This linear growth signifies the successful combination of PVP-S and WO_4^{2-} within the film. Some LbL assemblies containing two electroactive species have shown exponential growth,⁵⁶ but the continuous linear growth observed here suggests a constant level of deposition of both species up to at least 50 BLs. Thickness increase after each deposition of PVP-S is nearly the same as that of WO_4^{2-} , as shown in the inset in **Figure A.2**.

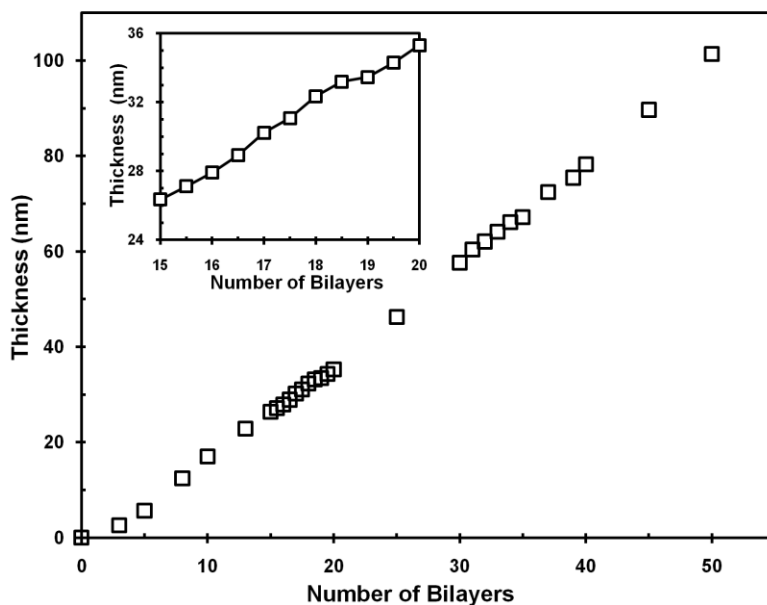


Figure A.2. Film thickness as a function of the number of PVP-S/ WO_4^{2-} BLs deposited, as determined by ellipsometry. The thickness increase from 15 to 20 BLs is shown in the inset. Half bilayers correspond to PVP-S deposition.

Using a QCM, the amounts of PVP-S and WO_4^{2-} adsorbed onto the crystal in each deposition cycle was estimated to be 0.38 and 1.27 $\mu\text{g}/\text{cm}^2$, respectively, as shown in **Figure A.3**. This trend is not surprising based upon the thickness data in **Figure A.2**, which shows that both ingredients contribute similarly. Generally, tungsten oxide has a much greater density ($7.16 \text{ g}/\text{cm}^3$)⁵⁷ than polymers included in PVP-S and should therefore contribute greater weight per layer. Assuming that each BL has an average thickness of 2 nm, this data yields a PVP-S/ WO_4^{2-} film density of $8.25 \text{ g}/\text{cm}^3$. This density is larger than either that of PVP-S or tungsten oxide individually, but is close to their sum. Thin films do not necessarily have densities that match their bulk values, so this apparent discrepancy may simply be the result of a more ordered structure, with reduced free volume, in the assembly. It is likely that WO_4^{2-} penetrates into, and adsorbs onto, an underlying PVP-S layer to form a PVP-S/ WO_4^{2-} complex.

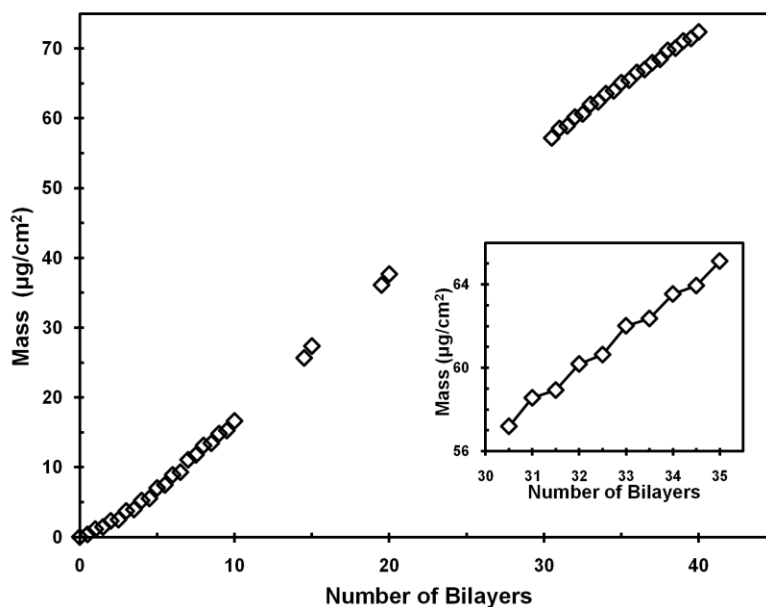


Figure A.3. Mass growth as a function of the number of PVP-S/ WO_4^{2-} BLs deposited, as measured with QCM. The inset is the mass change from 30 to 35 BLs. Half bilayers correspond to PVP-S deposition.

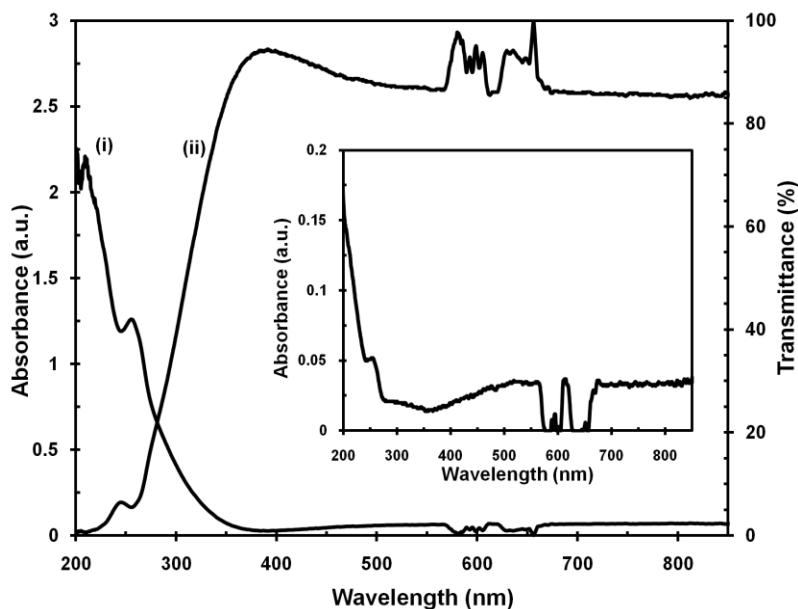


Figure A.4. Spectral absorbance (i) and transmittance (ii) of a 50 BL PVP-S/ WO_4^{2-} film produced on a fused quartz slide. The inset is the absorbance of a 145 nm PVP-S film that was spun coat on a quartz slide.

A 50 BL PVP-S/ WO_4^{2-} film on a fused quartz slide exhibits transmittance peaks at 246 and 391 nm, as shown in **Figure A.4**. In a hydrated tungsten oxide thin film, a transmittance peak appears at 390 nm,¹⁵ which suggests the presence of WO_4^{2-} into the thin film assembly without any alteration of electronic structure. Additionally, the maximum light absorption of a quartz slide, coated only with PVP-S, occurs below 200 nm (inset of **Figure A.4**) and creates no reduction of the WO_4^{2-} electrochromic performance. **Figure A.5** shows the absorbance spectra of PVP-S/ WO_4^{2-} films in the region of 200 to 850 nm as well as change of absorbance at 250 nm as a function of the number of bilayers deposited. The concentration of WO_4^{2-} in the PVP-S/ WO_4^{2-} film is almost constant, irrespective of the number of bilayers measured, as shown in the QCM measurements (**Figure A.3**). Therefore, the difference in absorbance of the PVP-S/ WO_4^{2-}

film with increasing number of BLs is due to increasing film thickness, according to the Beer-Lambert Law:⁵⁸

$$A = c \cdot \epsilon \cdot l \quad (1)$$

where c is the concentration, ϵ is the molar absorptivity, and l is the film thickness. Using UV-Vis absorbance and the reported molar absorptivity for sodium tungstate (Na_2WO_4) ($\epsilon = 6400 \text{ dm}^3/\text{mol}/\text{cm}$ at 200 nm wavelength),⁵⁹ the molar amount of WO_4^{2-} absorbed onto a quartz slide was estimated to be $4.51 \times 10^{-9} \text{ mol}/\text{cm}^2$, or $1.12 \text{ }\mu\text{g}/\text{cm}^2$ per BL, which is similar to the value obtained using QCM ($1.27 \text{ }\mu\text{g}/\text{cm}^2$). It has also been suggested that the concentration of WO_4^{2-} in the PVP-S/ WO_4^{2-} film is approximately constant irrespective of the substrate used.⁶⁰

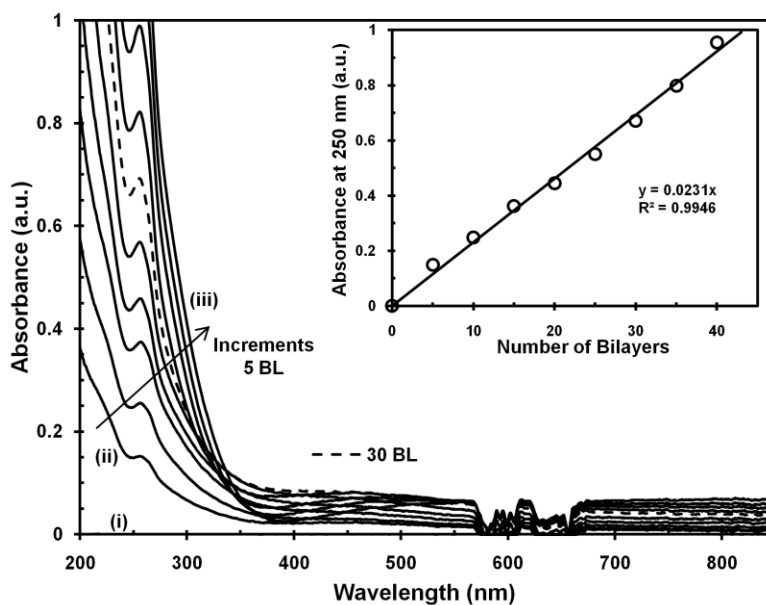


Figure A.5. Absorbance spectra of a quartz slide (i) and n BLs of PVP-S/ WO_4^{2-} , with $n = 5$ (ii) to 50 (iii), and every 5 BL step in between. The inset is absorbance at 250 nm as a function of the number of BLs deposited.

In an effort to improve electrochromic performance (see Section A.3.4), ITO was added to these tungstate-based thin films. In the first attempt to enhance its electrical conductivity and switching speed, ITO nanoparticles were added to the PVP-S deposition solution. An alternate recipe involved 30 QL films of PVP-S/ WO_4^{2-} /(PDDA+ITO)/ WO_4^{2-} for the same purpose (improved electrical conductivity and fast color switching). Film thickness and mass growth of ITO-added systems are shown in **Figure A.6**. (PVP-S+ITO)/ WO_4^{2-} BL and PVP-S/ WO_4^{2-} /(PDDA+ITO)/ WO_4^{2-} QL systems exhibit a reduction of 2.94% and 8.88% of film thickness respectively, whereas film mass decreases by 61.9% and 58.4% relative to the PVP-S/ WO_4^{2-} system (**Figures A.2 and A.3**). These results suggest that the addition of ITO particles generates lower density films. It may be that colloidal ITO disrupts the WO_4^{2-} structure in these films.

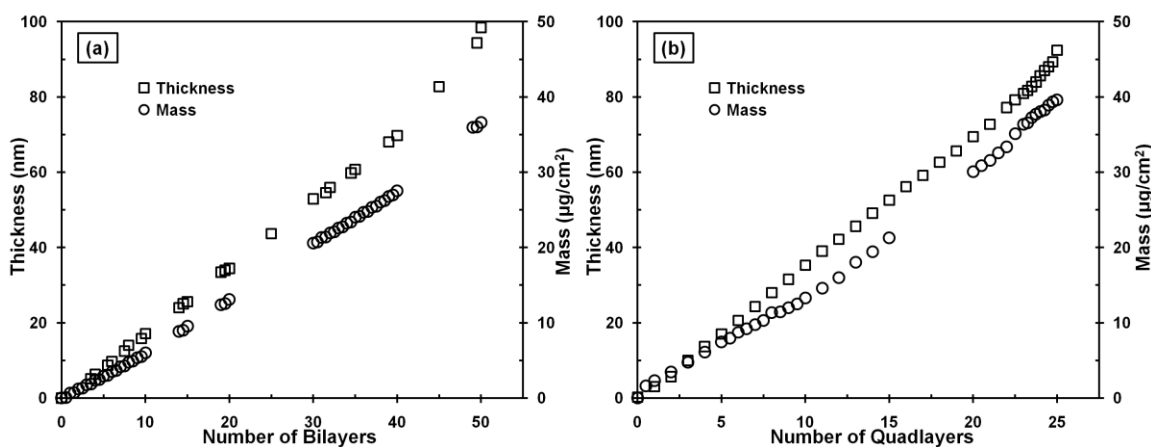


Figure A.6. Film thickness and mass growth as a function of the number of (a) (PVP-S+ITO)/ WO_4^{2-} BLs and (b) PVP-S/ WO_4^{2-} /(PDDA+ITO)/ WO_4^{2-} QLs, as determined by ellipsometry and QCM. Half bilayers correspond to PVP-S deposition.

A.3.2 Structural Characterization

TEM micrographs of a 60 BL PVP-S/ WO_4^{2-} cross-section are shown in **Figure A.7(a)**. In these images, the darker areas are WO_4^{2-} -rich regions and the lighter grey is PVP-S. Although not the goal of these images, they confirm the 120 nm thickness measured via ellipsometry and reflectometry. TEM is primarily used to visualize film structure, which in this case shows a highly inter-diffused nanostructure. These TEM images further support the suggestion, made in Section 3.1, that WO_4^{2-} penetrates into and adsorbs onto each underlying PVP-S layer. TEM cross-sections of 60 BL (PVP-S+ITO)/ WO_4^{2-} and 30 QL PVP-S/ WO_4^{2-} /(PDDA+ITO)/ WO_4^{2-} films are shown in **Figures A.7(b)** and **(c)**, respectively. In these images, the darkest black spots are ITO particles and darker and lighter grey areas are WO_4^{2-} -rich regions and PVP-S, respectively. In these two systems, several white regions are observed, indicating a looser, nano-porous structure due to the addition of ITO. These more open nano-structures contribute to the lower film densities of ITO-added systems that were measured using QCM in Section A.3.1. Also, addition of ITO particles gives these films a rougher surface

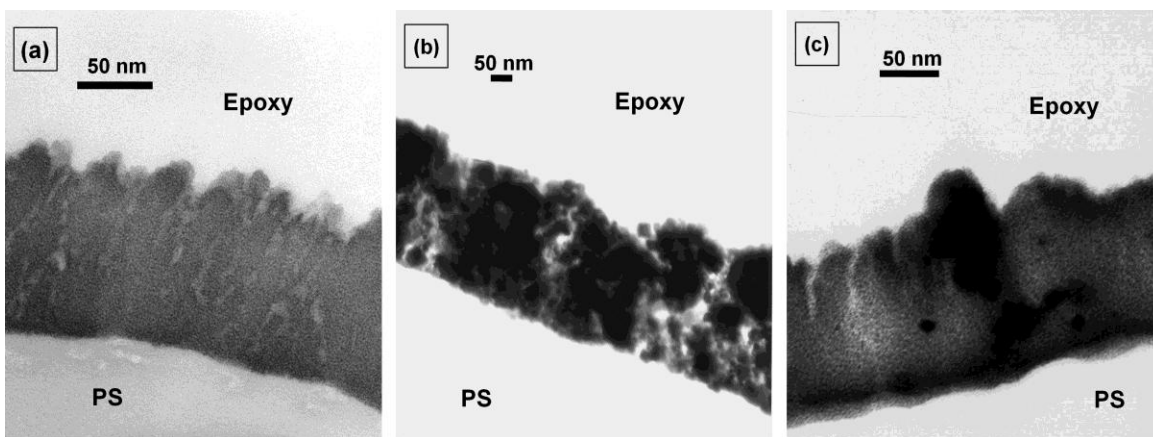


Figure A.7. TEM cross-sections of (a) a 60 BL PVP-S/ WO_4^{2-} film, (b) a 60 BL (PVP-S+ITO)/ WO_4^{2-} film, and (c) a 30 QL PVP-S/ WO_4^{2-} /PDDA+ITO/ WO_4^{2-} film.

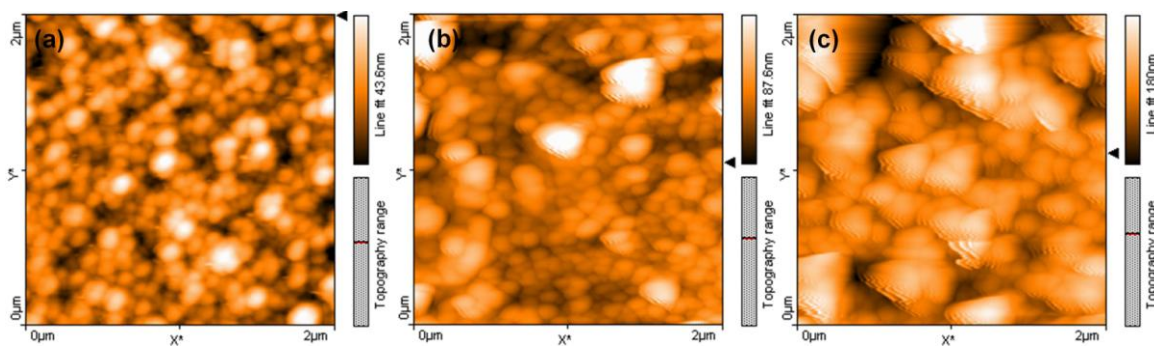


Figure A.8. AFM height images of (a) 50 BL PVP-S/ WO_4^{2-} , (b) 50 BL (PVP-S+ITO)/ WO_4^{2-} , and (c) 25 QL PVP-S/ WO_4^{2-} /(PDDA+ITO)/ WO_4^{2-} film surfaces on silicon wafers.

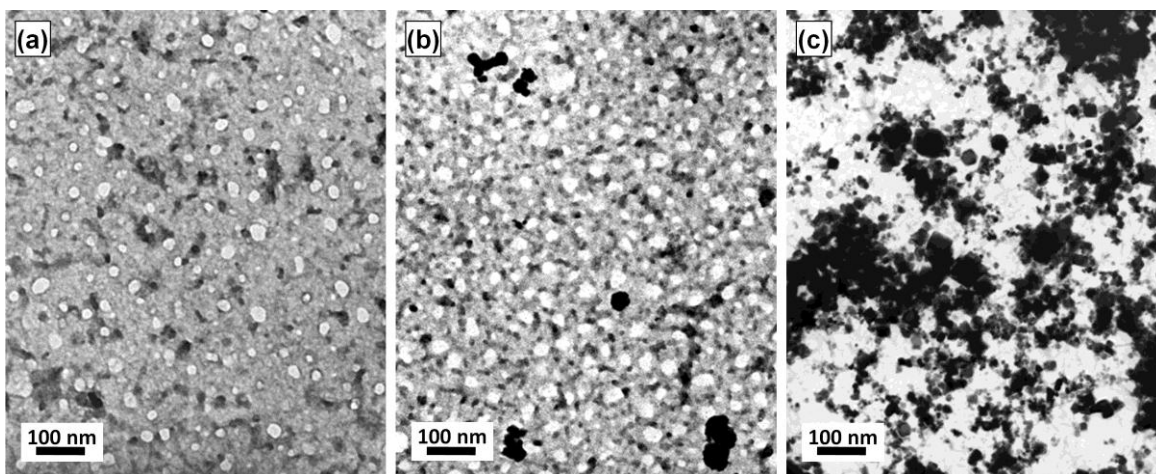


Figure A.9. TEM surface images of (a) 5 BL PVP-S/ WO_4^{2-} , (b) 5 BL (PVP-S+ITO)/ WO_4^{2-} , and (c) 3 QL PVP-S/ WO_4^{2-} /(PDDA+ITO)/ WO_4^{2-} films on formvar grids.

than the PVP-S/ WO_4^{2-} system. This surface roughness was analyzed using atomic force microscopy.

The surfaces of tungstate-based assemblies were analyzed using AFM in **Figure A.8**. PVP-S/ WO_4^{2-} , (PVP-S+ITO)/ WO_4^{2-} , and PVP-S/ WO_4^{2-} /(PDDA+ITO)/ WO_4^{2-} films (deposited onto silicon wafers) reveal structural differences. ITO addition generates greater roughness, with the range of surface height nearly doubled with the inclusion of 0.2 wt% ITO (**Figure A.8(b)**). The area roughness of a 50 BL PVP-S/ WO_4^{2-} is 5.5 nm,

whereas 50 BL (PVP-S+ITO)/WO₄²⁻ and 25 QL PVP-S/WO₄²⁻/(PDDA+ITO)/WO₄²⁻ films are 7.7 and 17.1 nm, respectively. **Figure A.9** shows TEM surface images of the each system. The darker areas are WO₄²⁻ and the lighter grey is PVP-S. Black dots in **Figures A.9(b)** and **(c)** are ITO. These images show greater ITO aggregation with higher concentration, which produces greater surface roughness. ITO aggregation forms a network within the interior of the PVP-S/WO₄²⁻/(PDDA+ITO)/WO₄²⁻ system, whereas ITO particles are isolated from each other (i.e., no network) in the (PVP-S+ITO)/WO₄²⁻ system. ITO could not be added beyond 0.2 wt% in PVP-S due to the high viscosity generated, which prevents uniform layer-by-layer deposition. This is further evidence of the strong attraction between ITO and PVP-S that ultimate reduces ITO's ability to enhance electrical conductivity in these thin films. Additionally, **Figure A.9(c)** shows interpenetration of WO₄²⁻ molecules with ITO in the polymer matrix.

A.3.3 Cyclic Voltammetry

Figure A.10 shows the cyclic voltammograms (CV) for a PVP-S/WO₄²⁻ 60 BL film deposited on an ITO coated glass electrode, illustrating the reduction process (and accompanying lithium ion insertion) via the negative current and oxidation via the positive current. Tests were run between 0.5 and -2.0 V vs. an AgCl/Ag reference electrode with 25, 50, 100, and 200 mV/s scan rates, in 0.1M LiCl aqueous solution electrolyte (pH = 2.5). During the reduction scan, the CV profile exhibits a peak near -1.0 V, which is the first reduction (WO₄²⁻ → WO₄³⁻). The PVP-S/WO₄²⁻ thin film keeps a deep blue color between -1.0 to -1.3 V, but this changes to pale yellow beyond -1.3 V due to the second reduction, suggesting conversion to tungsten bronze (i.e., WO₃²⁻). The

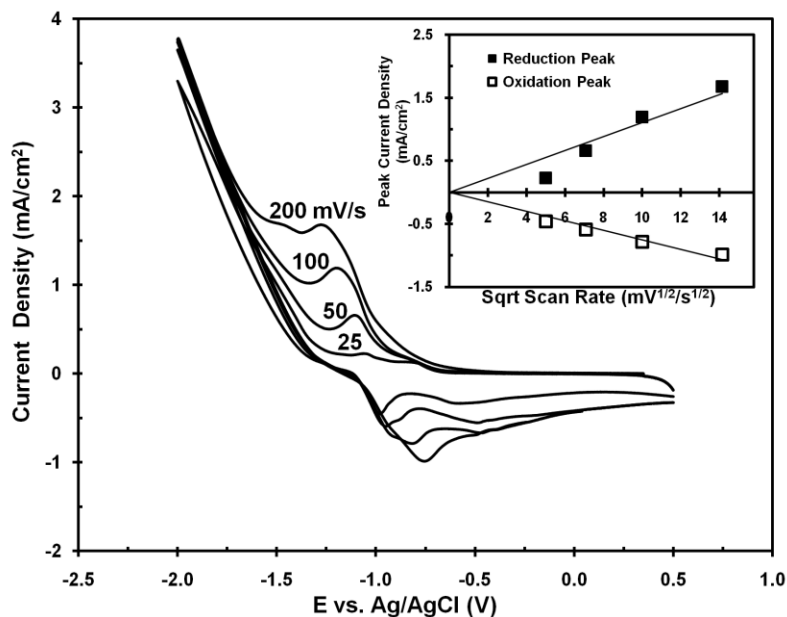


Figure A.10. Cyclic voltammetry of a 60 BL PVP-S/WO₄²⁻ film on an ITO-coated glass slide at 25, 50, 100, and 200 mV/s scan rates in an aqueous 0.1M LiCl electrolyte (pH = 2.5) with an AgCl/Ag reference electrode. Linear dependence of peak current density of a 60 BL PVP-S/WO₄²⁻ film as a function of the square root of the scan rate is shown in the inset.

current density peaks are proportional to the square root of the scan rate for both oxidation and reduction scans (inset in **Figure A.10**), suggesting that the current during the redox process is limited by the diffusion of lithium ions to the electrode surface as described by the Cottrell equation:⁶¹

$$i = n \cdot F \cdot A \cdot c_0 \cdot D^{1/2} \cdot \pi^{-1/2} \cdot t^{-1/2} \quad (2)$$

where i is the current, n is the number of electrons to reduce or oxidize one molecule of the material, F is the Faraday constant, A is the area of the planar electrode, c_0 is the initial concentration of tungstate species, D is the diffusion coefficient, and t is time. Furthermore, $(\text{scan rate})^{1/2}$ is used in place of $t^{-1/2}$. Therefore, linearity of current density peaks as a function of square root of the scan rate suggests a diffusion-controlled

system. In a prior study,⁵¹ a diffusion-controlled LbL film provided the maximum contrast possible for an electrochromic species, whereas the LbL film which was not diffusion-controlled, but rather surface-controlled (peaks increased linearly with the scan rate), produced charge trapping and film degradation.^{47,49,56}

The cyclic voltammograms of the other two systems are shown in **Figure A.11**. In the (PVP-S+ITO)/WO₄²⁻ system, the CV profile shows the same trend as the PVP-S/WO₄²⁻ system (**Figure A.10**), exhibiting the peak between -1.0 and -1.5 V and increasing beyond the first peak during the reduction scan. In the PVP-S/WO₄²⁻/(PDDA+ITO)/WO₄²⁻ system, however, the peaks during both reduction and oxidation scans are not as pronounced as the other two systems. Both ITO-containing systems also exhibit linear dependence of peak current density on the square root of the scan rate.

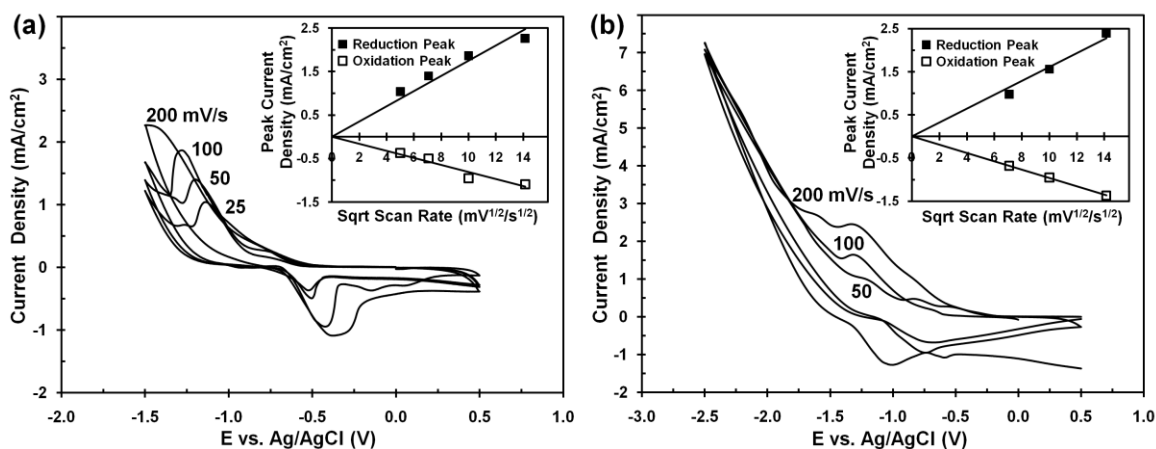


Figure A.11. Cyclic voltammetry of (a) a 60 BL (PVP-S+ITO)/WO₄²⁻ film at 25, 50, 100, and 200 mV/s scan rates and (b) a 30 QL PVP-S/WO₄²⁻/(PDDA+ITO)/WO₄²⁻ film at 50, 100, and 200 mV/s scan rates on ITO-coated glass slides with a AgCl/Ag reference electrode, in an aqueous 0.1M LiCl electrolyte (pH = 2.5). The insets highlight the linear dependence of peak current density of each film on the square root of the scan rate.

A.3.4 Electrochromic Behavior

Electrochromic behavior was investigated for 60 BL PVP-S/ WO_4^{2-} using UV-Vis absorption measurements made during application of different potentials. **Figure A.12(a)** shows the absorption spectra of a 60 BL PVP-S/ WO_4^{2-} film at +2.0, 0, and -1.0 V applied potentials. Absorbance increases as the potential becomes more cathodic, which corresponds to greater reduction of the initial WO_4^{2-} species. Beginning at +2.0 V (the oxidized state), the film is completely transparent. There is no change in absorbance between +2.0 and 0 V, but absorbance increases significantly from 0 to -1.0 V, as the tungstate is reduced. The maximum absorbance change appears at approximately 750 nm. **Figure A.12(b)** shows absorbance change at 750 nm in the PVP-S/ WO_4^{2-} system during repeated potential steps with 60 seconds time interval. The inset shows the change in the percent transmittance (% T) at this wavelength. When studying electrochromic performance, the key properties are contrast (i.e., difference of % T between dark and bleached states) and response time. High contrast and fast response are the goal. Optical

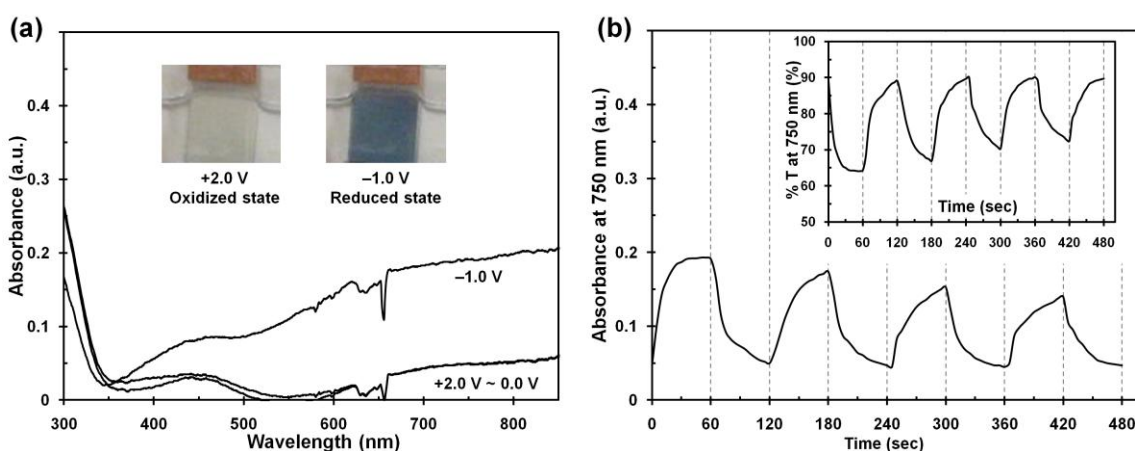


Figure A.12. (a) Absorption spectra of a 60 BL PVP-S/ WO_4^{2-} film at +2.0, 0, and -1.0 V applied potentials. (b) Absorbance at 750 nm as a function of time during repeated potential steps. The inset is the transmittance plot of this same film during the same time interval.

switching measurements were conducted by switching the electric potential between +2.0 (oxidized state) and -1.0 V (reduced state). Each switching cycle was two minutes long. The contrast of the first switching cycle is 25.2%, while at the fourth cycle it is 17.7% because tungstate coloration in the reduced state decreases with progressively with cycling. Switching time was determined as the time required to reach 90 % of the full change in absorbance (during reduction in the first cycle) after applying or switching the potential during each cycle. PVP-S/ WO_4^{2-} took 24 seconds to reach full coloration at the first cycle using this methodology, while switching time increased to over 60 seconds after the second cycle.

The addition of ITO nanoparticles to the PVP-S was done in an effort to enhance the film's electrical conductivity and improve switching speed. The absorption spectra of a 60 BL (PVP-S+ITO)/ WO_4^{2-} film is shown in **Figure A.13(a)**, which appears very similar to the 60 BL PVP-S/ WO_4^{2-} film (**Figure A.12(a)**). **Figure A.13(b)** shows absorbance changes at 750 nm, in this film made with 0.2 wt% ITO in PVP-S, by switching the same electrical potential (+2.0 \leftrightarrow -1.0 V) as with the PVP-S/ WO_4^{2-} system. The inset is the change in % T at 750 nm. With the addition of 0.2 wt% ITO, the contrast remains relatively constant (23–24 %) through four switching cycles, which was an improvement over the system that had no ITO. The system without ITO exhibits significant degradation with multiple cycles (see **Figure A.12(b)**). It is important to note that the switching time was not enough to fully oxidize or reduce during the potential switching because the response time of the ITO-based system is slower than that of the PVP-S/ WO_4^{2-} system without ITO. It is likely that PVP-S interacts too strongly with ITO to allow it to form a good conductive network.

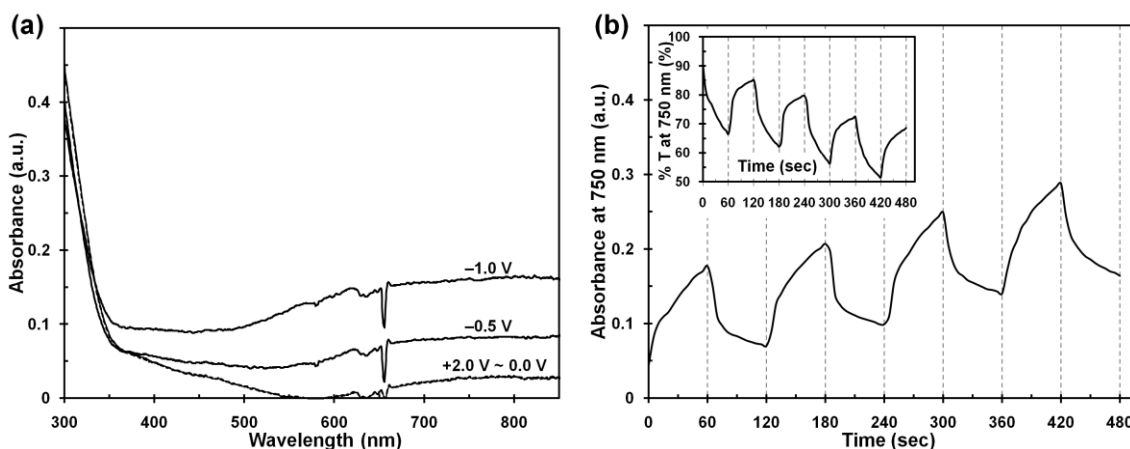


Figure A.13. (a) Absorption spectra for a 60 BL (PVP-S+ITO)/WO₄²⁻ film at applied potentials from +2.0 to -1.0 V in 0.5 V steps. (b) Absorbance changes at 750 nm during repeated potential steps.

In an alternate attempt to improve thin film conductivity, PDDA was used for layers containing ITO (in every other BL). **Figure A.14(a)** shows absorption spectra of the 30 QL PVP-S/WO₄²⁻/(PDDA+ITO)/WO₄²⁻ film, from +2.0 to -3.0 V with step size 0.5 V. Even with 1 wt% ITO added to PDDA in every other BL, 30 QL films were colorless in their deposited state. Beginning at +2.0 V, the film is in its transparent oxidized state. There is no change in absorbance between +2.0 and -1.0 V, but as the electrode potential becomes more cathodic, absorbance increases with the largest change between -1.5 to -2.0 V. A lack of peak in CV, as seen in **Figure A.11(b)**, suggests no reduction between -1.0 to -1.5 V, which is in contrast to the other two systems that had an optical change in this same range of electrical potential. Typical absorbance change of the PVP-S/WO₄²⁻/(PDDA+ITO)/WO₄²⁻ film (at 750 nm) during repeated potential step cycles of 0 ↔ -2.5 V is illustrated in **Figure A.14(b)**. The inset shows the change in % T at 750 nm. The contrast is constant at approximately 20% through four switching cycles.

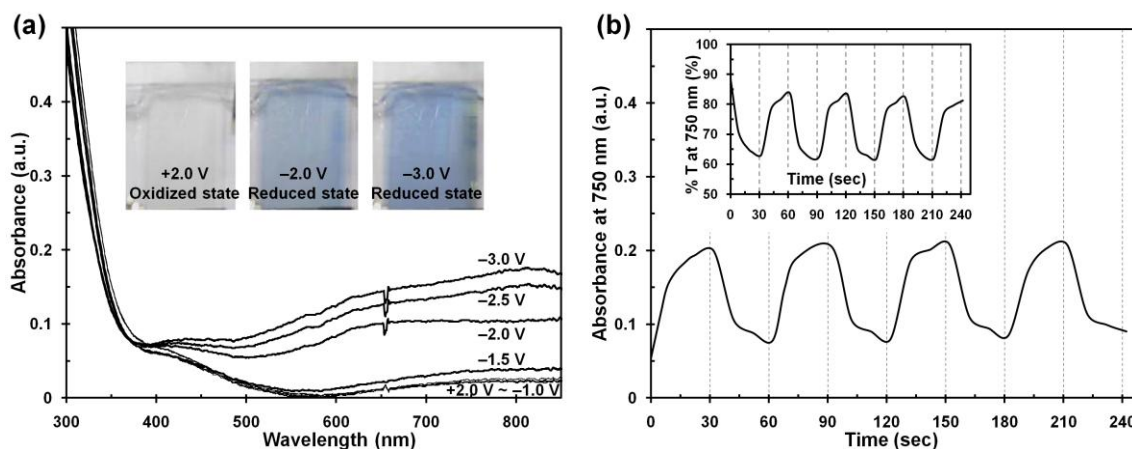


Figure A.14. (a) Absorption spectra for a 30 QL PVP-S/WO₄²⁻/(PDDA+ITO)/WO₄²⁻ film at applied potentials from +2.0 to -3.0 V in 0.5 V steps. (b) Absorbance changes at 750 nm during repeated potential steps.

This behavior is almost the same as the PVP-S/WO₄²⁻ system, but there is a constant level of coloration in the quadlayer system. This reproducibility of the optical response demonstrates the electrochromic stability of the self-assembled PVP-S/WO₄²⁻/(PDDA+ITO)/WO₄²⁻ films. Moreover, this system fully oxidizes and reduces, unlike the system with ITO added directly PVP-S (**Figure A.12(b)**) because of faster redox change. Therefore, the PVP-S/WO₄²⁻/(PDDA+ITO)/WO₄²⁻ system exhibits faster optical switching. Switching time of this system is a constant 14 seconds regardless of the number of cycles.

The relatively fast switching speed of polymer-WO₄²⁻ thin films is due to fast lithium ion migration and easy electron movement to WO₄²⁻ surfaces embedded in the film. Analysis of film growth and mass increase (See Section A.3.1) shows lower density in the ITO-added systems. Also, the TEM images (**Figure A.7**) reveal a looser film structure due to addition of ITO particles. Therefore, the lower density film construction

of ITO-added systems should offer faster lithium ion migration and the network of ITO particles, combined with their integration with WO_4^{2-} molecules, appears to provide faster electron movement than the initial PVP-S/ WO_4^{2-} system.

A.4 Conclusions

Electrochromic thin films were prepared using layer-by-layer assembly of sodium tungstate, colloidal ITO and polyelectrolytes (PVP-S and PDDA). Performance of these WO_4^{2-} -based thin films was studied with UV-Vis and cyclic voltammetry. These systems exhibit reversible color change between a transparent oxidized state and deep blue reduced state. The introduction of ITO nanoparticles to every other bilayer was shown to decrease the time to change color (i.e., switch) due to improved electrical conductivity. Using PDDA as a stabilizer for ITO, as a substitute for PVP-S in every other BL, produced fast switching and more stable contrast. Strong interaction between PVP-S and ITO prevented direct combination of these two ingredients from producing improved switching speed and electrochromic stability. The use of an electrically conductive particle to speed switching and improve stability could potentially be used in a variety of electrochromic systems. This study sets a precedent for future studies to improve electrochromic performance of thin film assemblies.

A.5 References

1. Monk, P.; Monk, P.; Mortimer, R.; Rosseinsky, D., *Electrochromism and electrochromic devices*. Cambridge Univ Pr: New York, 2007.
2. Monk, P.; Mortimer, R.; Rosseinsky, D., *Electrochromism: Fundamentals and applications*. VCH.: New York, 1995.

3. Mortimer, R. J., Electrochromic materials. *Chem. Soc. Rev.* **1997**, 26 (3), 147-156.
4. Marcel, C.; Tarascon, J. M., An all-plastic WO₃H₂O/polyaniline electrochromic device. *Solid State Ionics* **2001**, 143 (1), 89-101.
5. Vredenberg, W. J., Electrogenesis in the photosynthetic membrane: fields, facts and features. *Bioelectrochem. Bioenerg.* **1997**, 44 (1), 1-11.
6. Platt, J. R., Electrochromism, a possible change of color producible in dyes by an electric field. *J. Chem. Phys.* **1961**, 34 (3), 862-863.
7. Lampert, C. M., Towards large-area photovoltaic nanocells: experiences learned from smart window technology. *Sol. Energy Mater. Sol. Cells* **1994**, 32 (3), 307-321.
8. Granqvist, C. G.; Azens, A.; Hjelm, A.; Kullman, L.; Niklasson, G. A.; Ronnow, D.; Strome Mattsson, M.; Veszelei, M.; Vaivars, G., Recent advances in electrochromics for smart windows applications. *Sol. Energy* **1998**, 63 (4), 199-216.
9. Granqvist, C. G., Out of a niche. *Nat. Mater.* **2006**, 5 (2), 89-90.
10. Buyan, M.; Bruwiler, P. A.; Azens, A.; Gustavsson, G.; Karmhag, R.; Granqvist, C. G., Facial warming and tinted helmet visors. *Int. J. Ind. Ergon.* **2006**, 36 (1), 11-16.
11. Richardson, T. J., New electrochromic mirror systems. *Solid State Ionics* **2003**, 165 (1-4), 305-308.
12. Baucke, F. G. K.; Duffy, J. A.; Smith, R. I., Optical absorption of tungsten bronze thin films for electrochromic applications. *Thin Solid Films* **1990**, 186 (1), 47-51.
13. Kamimori, T.; Nagai, J.; Mizuhashi, M., Electrochromic devices for transmissive and reflective light control. *Sol. Energy Mater.* **1987**, 16 (1-3), 27-38.
14. Somani, P.; Mandale, A. B.; Radhakrishnan, S., Study and development of conducting polymer-based electrochromic display devices. *Acta Mater.* **2000**, 48 (11), 2859-2871.
15. Granqvist, C. G.; Avendano, E.; Azens, A., Electrochromic coatings and devices: survey of some recent advances. *Thin Solid Films* **2003**, 442 (1-2), 201-211.
16. Lavi, O.; Frey, G. L.; Siegmann, A.; Ein-Eli, Y., Enhanced tungstate electrochromism via formation of transparent conductive networks. *Electrochem. Commun.* **2008**, 10 (8), 1210-1213.
17. Granqvist, C., *Handbook of inorganic electrochromic materials*. Elsevier Science Ltd: Amsterdam, 1995.

18. Granqvist, C. G., Progress in electrochromics: tungsten oxide revisited. *Electrochim. Acta* **1999**, 44 (18), 3005-3015.
19. Patil, P. R.; Pawar, S. H.; Patil, P. S., The electrochromic properties of tungsten oxide thin films deposited by solution thermolysis. *Solid State Ionics* **2000**, 136-137, 505-511.
20. Svensson, J. S. E. M.; Granqvist, C. G., Modulated transmittance and reflectance in crystalline electrochromic WO₃ films: Theoretical limits. *Appl. Phys. Lett.* **1984**, 45 (8), 828-830.
21. Somani, P.; Radhakrishnan, S., Electrochromic materials and devices: present and future. *Mater. Chem. Phys.* **2003**, 77 (1), 117-133.
22. Sun, S.-S.; Holloway, P. H., Modification of vapor-deposited WO₃ electrochromic films by oxygen backfilling. *J. Vac. Sci. Technol. A* **1983**, 1 (2), 529-533.
23. Tägtström, P.; Jansson, U., Chemical vapour deposition of epitaxial WO₃ films. *Thin Solid Films* **1999**, 352 (1-2), 107-113.
24. Pennisi, A.; Simone, F.; Barletta, G.; Di Marco, G.; Lanza, M., Preliminary test of a large electrochromic window. *Electrochim. Acta* **1999**, 44 (18), 3237-3243.
25. Monk, P. M. S.; Akhtar, S. P.; Boutevin, J.; Duffield, J. R., Toward the tailoring of electrochromic bands of metal-oxide mixtures. *Electrochim. Acta* **2001**, 46 (13-14), 2091-2096.
26. Ozkan, E.; Lee, S.-H.; Liu, P.; Tracy, C. E.; Tepehan, F. Z.; Pitts, J. R.; Deb, S. K., Electrochromic and optical properties of mesoporous tungsten oxide films. *Solid State Ionics* **2002**, 149 (1-2), 139-146.
27. Badilescu, S.; Ashrit, P. V., Study of sol-gel prepared nanostructured WO₃ thin films and composites for electrochromic applications. *Solid State Ionics* **2003**, 158 (1-2), 187-197.
28. Regragui, M.; Addou, M.; Outzourhit, A.; Bern?e, J. C.; El Idrissi, E.; Benseddik, E.; Kachouane, A., Preparation and characterization of pyrolytic spray deposited electrochromic tungsten trioxide films. *Thin Solid Films* **2000**, 358 (1-2), 40-45.
29. Decher, G.; Lvov, Y.; Schmitt, J., Proof of multilayer structural organization in self-assembled polycation-polyanion molecular films. *Thin Solid Films* **1994**, 244 (1-2), 772-777.
30. Decher, G., Fuzzy nanoassemblies: Toward layered polymeric multicomposites. *Science* **1997**, 277 (5330), 1232-1237.

31. Grunlan, J. C.; Choi, J. K.; Lin, A., Antimicrobial behavior of polyelectrolyte multilayer films containing cetrimide and silver. *Biomacromolecules* **2004**, *6* (2), 1149-1153.
32. Podsiadlo, P.; Paternel, S.; Rouillard, J. M.; Zhang, Z. F.; Lee, J.; Lee, J. W.; Gulari, L.; Kotov, N. A., Layer-by-layer assembly of nacre-like nanostructured composites with antimicrobial properties. *Langmuir* **2005**, *21* (25), 11915-11921.
33. Jang, W. S.; Rawson, I.; Grunlan, J. C., Layer-by-layer assembly of thin film oxygen barrier. *Thin Solid Films* **2008**, *516* (15), 4819-4825.
34. Wang, Y.; Stedronsky, E.; Regen, S. L., Defects in a polyelectrolyte multilayer: The inside story. *J. Am. Chem. Soc.* **2008**, *130* (49), 16510-16511.
35. Nohria, R.; Khillan, R. K.; Su, Y.; Dikshit, R.; Lvov, Y.; Varahramyan, K., Humidity sensor based on ultrathin polyaniline film deposited using layer-by-layer nano-assembly. *Sens. Actuators, B* **2006**, *114* (1), 218-222.
36. Loh, K. J.; Kim, J.; Lynch, J. P.; Kam, N. W. S.; Kotov, N. A., Multifunctional layer-by-layer carbon nanotube-polyelectrolyte thin films for strain and corrosion sensing. *Smart Mater. Struct.* **2007**, *16* (2), 429-438.
37. Jiang, S.; Liu, Z.; Tian, Z., Layer-by-layer self-assembly of composite polyelectrolyte-nafion membranes for direct methanol fuel cells. *Adv. Mater.* **2006**, *18* (8), 1068-1072.
38. Farhat, T.; Hammond, P., Designing a new generation of proton-exchange membranes using layer-by-layer deposition of polyelectrolytes. *Adv. Funct. Mater.* **2005**, *15* (6), 945-954.
39. Cassagneau, T.; Fendler, J. H., High density rechargeable lithium-ion batteries self-assembled from graphite oxide nanoplatelets and polyelectrolytes. *Adv. Mater.* **1998**, *10* (11), 877-881.
40. Kim, B. S.; Park, S. W.; Hammond, P. T., Hydrogen-bonding layer-by-layer assembled biodegradable polymeric micelles as drug delivery vehicles from surfaces. *ACS Nano* **2008**, *2* (2), 386-392.
41. De Geest, B. G.; Dejumat, C.; Verhoeven, E.; Sukhorukov, G. B.; Jonas, A. M.; Plain, J.; Demeester, J.; De Smedt, S. C., Layer-by-layer coating of degradable microgels for pulsed drug delivery. *J. Control. Rel.* **2006**, *116* (2), 159-169.
42. Caruso, F.; Trau, D.; Möhwald, H.; Renneberg, R., Enzyme encapsulation in layer-by-layer engineered polymer multilayer capsules. *Langmuir* **2000**, *16* (4), 1485-1488.

43. Poghosian, A.; Abouzar, M. H.; Sakkari, M.; Kassab, T.; Han, Y.; Ingebrandt, S.; Offenhäusser, A.; Schöning, M. J., Field-effect sensors for monitoring the layer-by-layer adsorption of charged macromolecules. *Sens. Actuators, B* **2006**, *118* (1-2), 163-170.
44. Cui, T.; Liu, Y.; Zhu, M., Field-effect transistors with layer-by-layer self-assembled nanoparticle thin films as channel and gate dielectric. *Appl. Phys. Lett.* **2005**, *87* (18), 183105.
45. Walton, M. D.; Kim, Y. S.; Jan, C. J.; McConnel, E. P.; Everett, W. N.; Grunlan, J. C., Deposition and patterning of conductive carbon black thin films. *Synth. Met.* **2007**, *157* (16-17), 632-639.
46. Dawidczyk, T. J.; Walton, M. D.; Jang, W. S.; Grunlan, J. C., Layer-by-layer assembly of UV-resistant poly(3,4-ethylenedioxythiophene) thin films. *Langmuir* **2008**, *24* (15), 8314-8318.
47. Cutler, C.; Bouguettaya, M.; Reynolds, J., PEDOT polyelectrolyte based electrochromic films via electrostatic adsorption. *Adv. Mater.* **2002**, *14* (9), 684-688.
48. Jain, V.; Sahoo, R.; Jinschek, J. R.; Montazami, R.; Yochum, H. M.; Beyer, F. L.; Kumar, A.; Heflin, J. R., High contrast solid state electrochromic devices based on Ruthenium Purple nanocomposites fabricated by layer-by-layer assembly. *Chem. Commun.* **2008**, (31), 3663-3665.
49. DeLongchamp, D. M.; Hammond, P. T., Multiple-color electrochromism from layer-by-layer-assembled polyaniline/prussian blue nanocomposite thin films. *Chem. Mater.* **2004**, *16* (23), 4799-4805.
50. Kim, E.; Jung, S., Layer-by-layer assembled electrochromic films for all-solid-state electrochromic devices. *Chem. Mater.* **2005**, *17* (25), 6381-6387.
51. Jain, V.; Khiterer, M.; Montazami, R.; Yochum, H. M.; Shea, K. J.; Heflin, J. R., High-contrast solid-state electrochromic devices of viologen-bridged polysilsesquioxane nanoparticles fabricated by layer-by-layer assembly. *ACS Appl. Mater. Interfaces* **2009**, *1* (1), 83-89.
52. Malynych, S.; Luzinov, I.; Chumanov, G., Poly(vinyl pyridine) as a universal surface modifier for immobilization of nanoparticles. *J. Phys. Chem. B* **2002**, *106* (6), 1280-1285.
53. Bain, C. D.; Evall, J.; Whitesides, G. M., Formation of monolayers by the coadsorption of thiols on gold - variation in the head group, tail group, and solvent. *J. Am. Chem. Soc.* **1989**, *111* (18), 7155-7164.

54. Kern, W., The evolution of silicon-wafer cleaning technology. *J. Electrochem. Soc.* **1990**, *137* (6), 1887-1892.
55. Owens, D. K., The mechanism of corona and ultraviolet light-induced self-adhesion of poly(ethylene terephthalate) film. *J. Appl. Polym. Sci.* **1975**, *19*, 3315-3326.
56. DeLongchamp, D. M.; Kastantin, M.; Hammond, P. T., High-contrast electrochromism from layer-by-layer polymer films. *Chem. Mater.* **2003**, *15* (8), 1575-1586.
57. Eagleson, M., *Concise encyclopedia chemistry*. Walter De Gruyter & Co.: Berlin, 1994.
58. Ingle, J. D. J.; Crouch, S. R., *Spectrochemical analysis*. Prentice Hall: New Jersey, 1988.
59. Saito, N.; Kudo, A.; Sakata, T., Synthesis of tungstate thin films and their optical properties. *Bull. Chem. Soc. Jpn.* **1996**, *69* (5), 1241-1245.
60. Moriguchi, I.; Fendler, J. H., Characterization and electrochromic properties of ultrathin films self-assembled from poly(diallyldimethylammonium) chloride and sodium decatungstate. *Chem. Mater.* **1998**, *10* (8), 2205-2211.
61. Bard, A. J.; Faulkner, L. R., *Electrochemical methods: Fundamentals and applications*. Wiley: New York, 2001.

VITA

Name: Park, Yong Tae

Address: Department of Mechanical Engineering
c/o Dr. Jaime C. Grunlan
Texas A&M University
College Station, TX 77843-3123

Email: yong.t.park@gmail.com

Education: B.S., Mechanical Engineering, KAIST (Korea Advanced Institute of
Science and Technology), 1998

M.S., Mechanical Engineering, POSTECH (Pohang University of Science
and Technology), 2001

Ph.D., Mechanical Engineering, Texas A&M University, 2011